國立臺灣大學工學院土木工程學系

碩士論文

Department of Civil Engineering

College of Engineering

National Taiwan University

Master Thesis

加勁砂樁穩固邊坡受滲流作用之流固耦合分析

Coupled Hydro-mechanical Analysis of Geosynthetic Encapsulated Granular Columns (GECs) Stabilized Slope Subjected to Seepage Conditions

蘇愷瑞

Sukrityranjan Samanta

指導教授：楊國鑫 博士

Advisor: Kuo-Hsin Yang, Ph.D.

中華民國 112 年 6 月

June, 2023

doi:10.6342/NTU202301082

Acknowledgment

I would like to begin by expressing my profound gratitude to my advisor, Prof. Kuo-Hsin Yang, whose inspirational personality planted the seed for my pursuit of a doctoral degree. His unwavering guidance, support, and extensive expertise have been instrumental in the completion of my thesis. I will forever be guided by my admiration for him as I strive for excellence in all future endeavors.

I extend my heartfelt appreciation to my parents for their unwavering support during the most challenging times in my life. They have shouldered the burden of countless issues, ensuring that I could remain focused on achieving my goals. I am committed to honoring their sacrifices through my actions, particularly during times of uncertainty.

My gratitude extends to my fellow lab mates, who have provided invaluable support throughout my journey in Taiwan. I am particularly grateful to Dr. Chiang Jung, Peng Yi-Ping, Fu Ya-Hsuan, Wu Chung-Wei, Michel Edwige, and many others for their assistance. Additionally, I would like to offer special thanks to my fellow Indians in Taiwan who introduced me to the cricket and music club where I had spent my leisure time.

Furthermore, I would like to express my sincere appreciation to all the teachers and individuals I have encountered who believed in and supported me throughout my life's journey especially Vivek Gupta, Anamika Ghosh, Aarudra Nath, Dr. Sandeep Chouksey, Arpita Das, and Sushil Pant. I am truly fortunate to have crossed paths with them.

As you peruse my work, I hope you find it engaging and informative.

Sincerely,

Sukrityranjan Samanta

June 05, 2023

doi:10.6342/NTU202301082

Abstract

This study presents a meticulous investigation of the performance of geosynthetic encased granular column (GEC) stabilized slopes under extreme seepage conditions through a series of finite element (FE) analyses, validated by one-gravity (1-g) model tests. The primary objective is to evaluate the effectiveness of GEC stabilized slopes as a remedial measure for natural slopes failing under severe seepage conditions.

The research first employs a FE analysis of a natural slope, with a 50° slope angle and a total height of 6-meters, subjected to extreme seepage conditions, constructed atop an impermeable rock layer. This foundational scenario serves as a comparative basis against an OSC stabilized slope, GEC stabilized slope, a rigid pile stabilized slope, and a GEC stabilized slope with horizontal drainage conditions. The failure surface patterns are observed from the incremental shear strain ($\Delta\gamma_s$) and the results are scrutinized based on the progression of horizontal displacement (u_x), top settlement (u_z), dissipation of pore water pressure (PWP), and central line horizontal deflection of GEC.

Numerical simulations of the aforementioned scenarios serve as the baseline, with their veracity validated through reduced-scale model experiments for final failure surface, phreatic surface progression, and the deformed surface profile of stabilized slope. The GEC-stabilized slope outperforms the limitations of rigid piles due to its vertical drainage capacity, which impedes the development of steady-state seepage conditions. Rigid piles, with their superior bending stiffness, restrict the movement of soil particles, inducing k_0-conditions and a strong arching effect. Conversely, GECs, due to their lower bending stiffness, allow deformation, leading to k_a-conditions. This mobilization of strain for GEC stabilized slopes results in a uniform distribution of stress in the horizontal direction (σ_{xx}) near the GEC. The inclusion of GECs effectively extends the failure timing of the slope

doi:10.6342/NTU202301082

in comparison to both the natural and rigid pile stabilized slopes. The research identifies two primary stabilizing mechanisms: arching effect and soil shear strain mobilization.

The numerical results from the parametric study indicate that insertion of GECs increases the overall system stiffness, which does not necessarily enhance the slope stability. To secure adequate slope system stabilization against extreme seepage conditions, a proper quantification of the contribution of mechanical, hydraulic, and volume-controlling parameters is imperative. *S/D* ratio and diameter (*D*) are the most influential parameters where increment in stiffness of slope system caused the increment in horizontal deformation and failure timing. With properly installed horizontal drainage systems, GECs demonstrate their superiority as the most suitable solution. The study concludes with comprehensive design recommendations proposed for practical engineering applications.

Keywords: Geosynthetic encased granular columns (GEC), flexible structural systems, extreme seepage conditions, rigid piles, failure mechanisms, arching effect, drainage systems, volume-controlling parameters

doi:10.6342/NTU202301082

Table of Contents

doi:10.6342/NTU202301082

doi:10.6342/NTU202301082

doi:10.6342/NTU202301082

List of Tables

doi:10.6342/NTU202301082

List of Figures

Chapter 1 Introduction

Chapter 2 Literature review

doi:10.6342/NTU202301082

Chapter 3 Finite element analysis

doi:10.6342/NTU202301082

doi:10.6342/NTU202301082

doi:10.6342/NTU202301082

Chapter 6 Parametric study

doi:10.6342/NTU202301082

doi:10.6342/NTU202301082

doi:10.6342/NTU202301082

doi:10.6342/NTU202301082

List of Symbols and Nomenclature

Basic SI units are given in parentheses

English Letters-Upper Case

D	diameter of pile or GEC (m)
D_{50}	mean particle size (m)
D_r	relative density (%)
E	composite Young's modulus of the GEC/pile (kN/m^2)
E_s	young's modulus of the soil based on Mohr Coulomb's failure criteria (kN/m^2)
E_ϕ	efficiency factor (dimensionless)
E_{50}^{ref}	secant modulus (kN/m^2)
E_{oed}^{ref}	tangent oedometer loading modulus (kN/m^2)
E_{ur}^{ref}	unloading-reloading modulus (kN/m^2)
F_x	body force corresponding to the x-direction (kN)
F_y	body force corresponding to the y-direction (kN)
F_z	body force corresponding to the z-direction (kN)
G	shear modulus of soil (kN/m^2)
G_s	specific gravity (dimensionless)
H	slope height (m)
H_e	height of the pile/GEC (m)
I	area moment of inertia (kN-m^2)
$J_{50\%}$	reinforcement stiffness (kN/m)
L	cross-sectional length of slope (m)

doi:10.6342/NTU202301082

N	scaling factor (dimensionless)
P_r	tensile resistance of the reinforcement (kN/m)
R^2	coefficient of determination (dimensionless)
R_{inter}	interface reduction factor (dimensionless)
S	spacing between pile or GEC (m)
S_{res}	residual water content (%)
S_{sat}	saturated water content (%)
S_H	average horizontal support spacing (m)
S_V	average vertical support spacing (m)
T	reinforcement tensile force (kN/m)
T_{max}	mobilized maximum reinforcement tensile force (kN/m)
T_{ult}	reinforcement ultimate tensile strength (kN/m)

English Letters-Lower Case

a, b, c	fitting constants for sigmoid function (dimensionless)
c'	effective cohesion (kPa)
e	natural exponential function (dimensionless)
g_a	Curve fitting parameters as expressed by Brinkgreve et al. (2019)
g_c	Curve fitting parameters as expressed by Brinkgreve et al. (2019)
g_n	Curve fitting parameters as expressed by Brinkgreve et al. (2019)
k	hydraulic conductivity at any soil degree of saturation (m/sec)
k_{e}	saturated hydraulic conductivity of encased soil (m/sec)
k_{s}	saturated hydraulic conductivity of sloped soil (m/sec)
k_{rel}	relative hydraulic conductivity (dimensionless)

doi:10.6342/NTU202301082

n Curve fitting parameters in van Genuchten-Mualem's model (dimensionless)

s_u undrained shear strength of the soil at the bottom of the excavation (kPa)

u_x horizontal displacement (m)

u_z settlement (m)

u_a - u_w matric suction (where u_a and u_w are the pore air and pore water pressures, respectively) (kPa)

x distance to the left boundary (m)

Greek Letters-Upper Case

Θ normalized volumetric water content (dimensionless)

Greek Letters-Lower Case

α Curve fitting parameters in van Genuchten-Mualem's model (dimensionless)

α_B Biot–Willis coefficient (dimensionless)

γ soil unit weight (kN/m^3)

γ_d dry unit weight (kN/m^3)

$\gamma_{d,\ max}$ maximum dry unit weight (kN/m^3)

$\gamma_{d,\ min}$ minimum dry unit weight (kN/m^3)

γ_{xy} soil shear strain (dimensionless)

$\delta_{H(max)}$ maximum horizontal deformation (m)

$\delta_{V(max)}$ maximum horizontal deformation (m)

δ' effective interface friction angle (degree)

δ_{max} maximum surface settlement (m)

ε reinforcement tensile strain (%)

doi:10.6342/NTU202301082

ε_a	soil axial strain (%)
ε_f	reinforcement tensile strain at failure (%)
ε_{max}	mobilized maximum reinforcement tensile strain (%)
ε_r	residual reinforcement tensile strain (%)
ε_v	soil volumetric strain (%)
ε_{ult}	reinforcement ultimate tensile strain (%)
θ_r	residual volumetric water content (%)
θ_s	saturated volumetric water content (%)
λ	scaling factor based on geometrical similarity (dimensionless)
λ_E	scaling factor based on modulus of elasticity (dimensionless)
ρ	density of the fluid (gram/cm^3)
σ_3	confining pressure (kPa)
σ_d	deviatoric stress (kPa)
σ_n	normal stress on the soil-reinforcement interface (kPa)
σ_v	overburden pressure (kPa)
τ_{max}	soil-reinforcement interface shear strength (kPa)
$\tau_{mobilized}$	mobilized interface shear stress (kPa)
τ_{rel}	interface shear stress ratio (dimensionless)
ϕ'	effective peak friction angle (degree)
ϕ_{ps}	soil friction angle in the plane strain state (degree)
ϕ_{tx}	soil friction angle obtained by triaxial tests (degree)
ϕ_p	pressure head (m)
ν	poisson's ratio (dimensionless)
ψ	dilation angle (degree)

doi:10.6342/NTU202301082

List of Abbreviations

CD	consolidated drained
DEM	district element method
EA	axial rigidity
EI	flexural rigidity
FDM	finite difference method
FEM	finite element method
FS	factor of safety
GEC	geosynthetic encased granular column
GRS	geosynthetic reinforced soil
INDOT	Indiana state department of transportation
MPM	material point method
OMC	optimal moisture content
OSC	ordinary stone column
PIV	particle image velocimetry
PWP	pore water pressure
RCC	reinforced cement concrete
SC	stone column
SWCC	soil-water characteristic curve
USCS	unified soil classification system
USDA	U.S. Department of Agriculture

doi:10.6342/NTU202301082

Chapter 1 Introduction

1.1 Research background and motivation

The stability of slopes is critical in Geotechnical Engineering, serving to counteract the devastating effects of landslides. This necessity underscores its significance in protecting human lives and mitigating impacts on construction resources such as roadways, buildings, and more. Experts have long focused on slope stabilization techniques, with various innovative methods emerging to supplant conventional ones like sheet piles, soil nails, and anchors. However, these conventional practices demand substantial amounts of concrete as construction materials, which are not eco-friendly and sustainable (Khan & Ali, 2022). This shortcoming necessitates the development of superior construction materials. (Figure 1.1)

(a)

doi:10.6342/NTU202301082

(b)

Figure 1.1: Collapse of a slope designed as steep as 2:1, placed on sloping natural ground in S.R. 237, Perry county, Indiana, USA (Picture credit: INDOT): (a) first collapse; and (b) second collapse after first correction of insertion of soil nail wall, H-pile encasement, and a shotcrete facing

A promising material is the "Geosynthetic Encased Granular Column (GEC)", which has been utilized as a ground improvement technique for various land reclamation projects and embankment construction for some time. GECs are advanced composite materials comprising granular soil encased in geosynthetic materials (Huesker, 2021). These individual cylindrical columnar materials of varying diameters and lengths, when used in a series, form a flexible structural system for slope stabilization. This presents significant prospects for using such composite materials over traditional techniques. However, the quantification of GECs' response to external loads and their failure mechanics have not been thoroughly studied for slope stabilization applications. One aim of this research is to advance the application of GECs for slope stabilization and investigate their failure mechanisms.

doi:10.6342/NTU202301082

GECs enhance the load-bearing and shear capacity of slopes through the confinement of granular soil, rendering it less susceptible to failure (Araujo et al., 2009; Castro & Sagaseta, 2013; Chong et al., 2018; NYSDOT, 2013; and Wu et al., 2009). This confinement action is quantified as Hoop's stress. GEC structures can be constructed using either stone or sand columns. Due to the limitations of stone availability and environmental concerns surrounding stone quarries, this research focuses on the utilization of sand columns. Such structures not only improve structural integrity but also enhance the drainage capacity for excessively developed pore water pressure, reducing both immediate and long-term settlement (Heibaum, 2014). Thus, the flexibility, eco-friendly material, ease of construction/installation, and good drainage properties make GECs preferred materials for this study (Figure 1.3).

For this study, the stabilization of the slope is considered as part of a natural slope subject to seepage, overlaid on an impermeable rock layer. The predominant soil type under these conditions is colluvium, a marginal soil (Jeng & Sue, 2016; Song & Cui, 2016; and Soralump et al., 2021). A constant geosynthetic encased granular column diameter of 0.5 m, common in construction practice, has been considered. Columns have been placed at the upslope side to evaluate the most suitable location for application, considering the availability of a longer column inside the stabilized slope, which would effectively dissipate active pore water pressure. The performance of the flexible column system achieved by GECs has been compared with the rigid column system, conventionally achieved by concrete piles of the same diameter.

doi:10.6342/NTU202301082

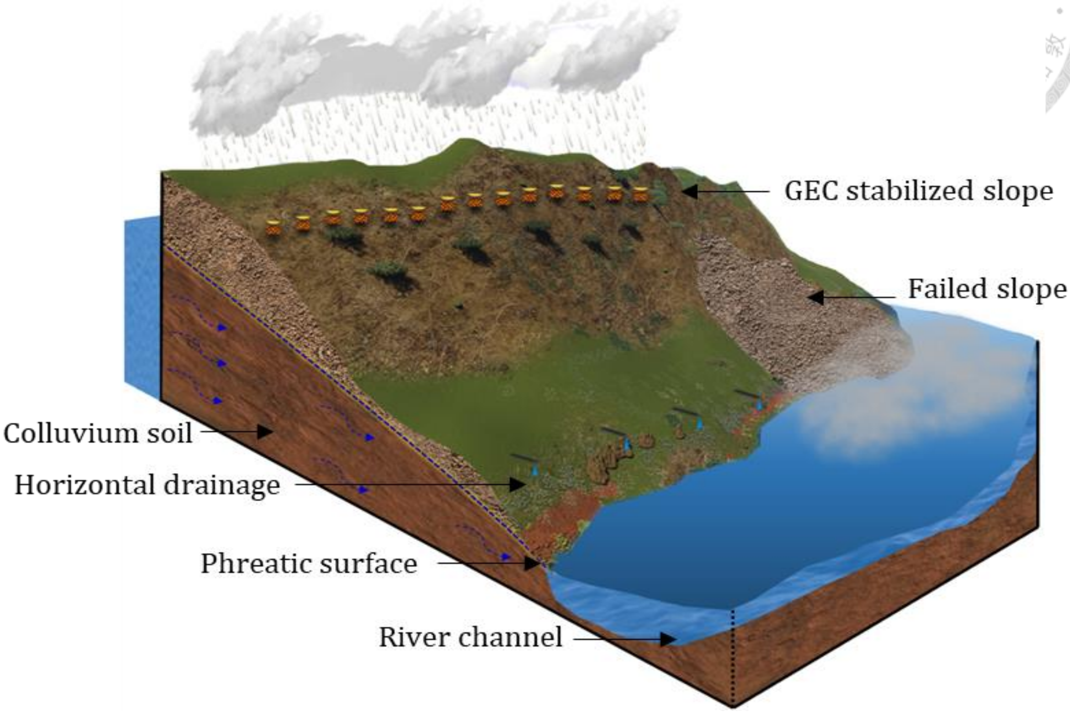

(a)

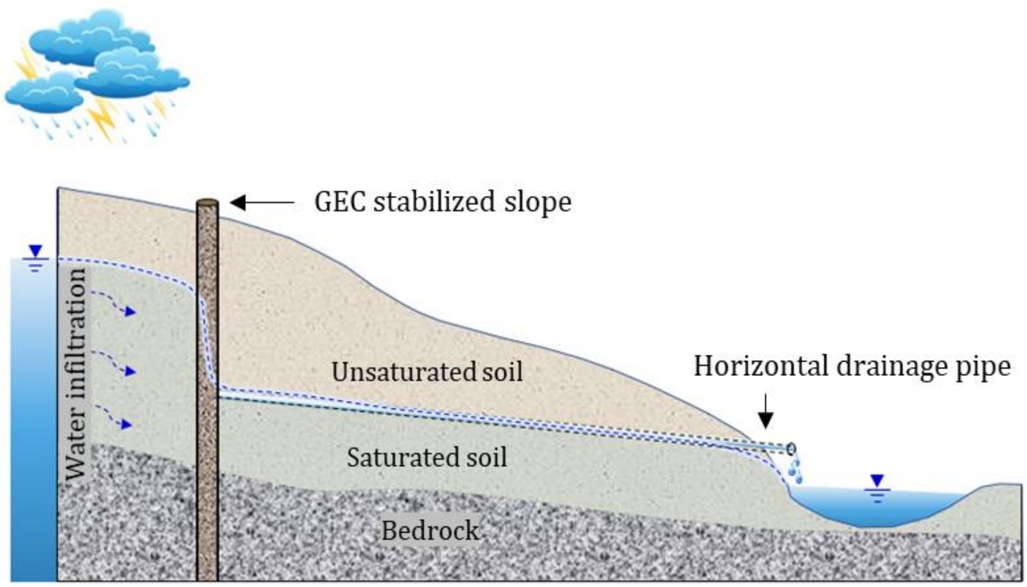

(b)

Figure 1.2: Conceptual case representing the GEC stabilized slope with horizontal drainage subjected to extreme seepage conditions in hilly terrain: (a) isometric view; and (b) cross-sectional view

doi:10.6342/NTU202301082

Furthermore, different types of installed drainage facilities, namely horizontal and vertical drainage systems, are evaluated based on slope stability efficiency, directly linked to the effective dissipation of pore water pressure. A comparative study based on specific points on the stabilized slope are analyzed the horizontal displacement, settlement, and pore water pressure dissipation over time for both flexible and rigid columnar systems.

As an extension of the study, a set of parametric studies is conducted to understand the influence of the hydraulic and mechanical properties of the column on the overall stability of the slope systems. The parametric study included the *S/D* ratio, column diameter, shear strength parameter of encased soil, stiffness of encased soil, relative permeability ratio, and stiffness of the reinforcement surrounding the columnar structure.

The failure mechanisms are analyzed based on the distribution of horizontal shear stress (σ_{xx}) across the cross section, considered at the mid-height of the slope. This contour aids in understanding the influence of the arching effect. A pronounced arching effect is observed in the case of the rigid pile, where stress concentration was noticed adjacent to the column, an element missing in the GEC-stabilized slope due to its flexible columnar system.

Given that GEC is a composite material, its flexural rigidity is determined through numerical simulations and experimental models. These findings are further corroborated by a unique analytical approach developed in this research, ensuring consistency across all adopted methodologies.

A separate study is conducted on a reduced-scale experimental model. The results of this Finite Element Method (FEM)-based numerical simulation are verified using a 1-*g* reduced-scale model test. Validation of the results include the final failure surface,

doi:10.6342/NTU202301082

deformed surface profile, and progression of the phreatic surface. The overall conclusive results show that the rigid pile-stabilized slope failed prior to the slope stabilized with the GEC. This is due to the GEC's drainage property, which continually provided drainage functionality, delaying soil particle movement. The rigid pile certainly stabilized the soil on the stabilized side, but it failed to prevent failure on the non-stabilized slope side.

Additionally, various research limitations within this study should be thoroughly examined before practical application for slope stabilization. These limitations include the columnar system with various diameters, diverse loading patterns, and slope characteristics.

doi:10.6342/NTU202301082

1.2 Research objectives

The primary objective of this research is to assess the performance of a Geosynthetic Encased Granular Column (GEC) stabilized slope system, utilized as a mitigation strategy for slope stability under varying seepage conditions. These conditions may arise from numerous factors such as a rise in groundwater levels, flooding, or rainfall infiltrations. The effectiveness of the GEC-stabilized slope has been compared and analyzed alongside the traditional reinforced concrete-based rigid pile system. Furthermore, the reinforcing mechanisms and the influence of various design parameters were investigated. The specific objectives of this research include:

- Proposing the utilization of GEC as an alternative method for slope stabilization.
- Investigating the combined effects of soil strength and drainage improvement provided by GEC on enhancing slope stability.
- Evaluating the unique failure behavior exhibited by various GEC-stabilized slope cases subjected to transient seepage analysis.

doi:10.6342/NTU202301082

1.3 Research layout

This thesis is organized into seven distinct chapters. Figure 1.4 graphically illustrates the research flow chart, encompassing the following sections:

Chapter 1: Introduction - This chapter sets the stage by presenting the background, motivation, and objectives that underpin this research.

Chapter 2: Literature Review - This chapter collates a review of the varied applications of Geosynthetic Encased Columns (GEC), characteristics of slope stabilization with rigid piles, failure mechanisms of GEC stabilized ground and slope, and case studies of rigid pile stabilized slope scenarios. Additionally, it delves into the theoretical foundations of the similarity analysis used in the 1-*g* model tests and the constitutive model applied in the numerical analyses.

Chapter 3: Finite Element Analysis - Chapter 3 elucidates the specifics of the Finite Element (FE) analyses conducted in this research. It discusses the numerical models, boundary conditions, input material properties, and parameter validation.

Chapter 4: Model validation - Chapter 4 elucidates the specifics of the 1-*g* model test conducted in this research for the validation purpose of numerical model.

Chapter 5: Numerical Results - This chapter disseminates the numerical results concerning natural slopes, OSC stabilized slopes, GEC stabilized slopes, rigid pile stabilized slopes, and GEC stabilized slopes with horizontal drainage under extreme seepage conditions. Furthermore, it presents numerical results for the evaluation of

doi:10.6342/NTU202301082

stabilizing mechanisms, and the influence of the arching effect.

Chapter 6: Parametric Study - Chapter 6 presents the outcomes of a parametric study of various GEC stabilized slope cases subjected to extreme seepage conditions. It reports the results for failure cases and enhanced measures, presented in terms of the analysis results of the slope system.

Chapter 7: Conclusions - The concluding chapter offers design recommendations and draws conclusions based on the findings of this study.

doi:10.6342/NTU202301082

Coupled hydro-mechanical analysis of Geosynthetic encapsulated granular column (GEC) stabilized slope subjected to seepage conditions

↓

Introduction

Research motivation and objectives **(Chapter 1)**

↓

Background

GEC, slope stabilization, failure mechanisms, and case studies **(Chapter 2)**

↓

Methodology

boundary conditions, input properties, parameter validation **(Chapter 3)**

↓

Results and recommendation

Model validations **(Chapter 4)**

Numerical results **(Chapter 5)**

Parametric results **(Chapter 6)**

↓

Conclusions

Conclusions and recommendations **(Chapter 7)**

Figure 1.3: Research flowchart

doi:10.6342/NTU202301082

Chapter 2 Literature Review

Geosynthetic Encased Columns (GEC) stabilized slope structures are primarily composed of reinforcement materials (specifically geotextiles), encased granular soil, and drainage systems. Traditional methods of slope stabilization have typically relied on the use of rigid piles constructed from reinforced concrete. Additionally, various other structural components, such as retaining walls or micropile systems, have been employed for slope stabilization. In recent years, innovative techniques have emerged, integrating Geosynthetic Reinforced Soil (GRS) structures with an array of facing systems. However, the construction of GRS structures often necessitates substantial spacing and entails considerable time and financial expenditure (Berg et al., 2009a; Berg et al., 2009b; and Elias et al., 2001). Consequently, GEC stabilized slope systems can present a more effective solution, given their inherent drainage properties and encasement stiffness. These attributes enhance their resistance to failure induced by excessive seepage.

2.1 Characteristics of slope stabilization with rigid pile

Landslides, or slope failures, are natural phenomena that occur globally, posing threats to human life and causing extensive property damage. A multitude of factors can trigger these failures, including slope steepening, seismic activity, surface erosion, deforestation, and most notably, rainfall infiltration. This latter cause is particularly prevalent in tropical regions, where prolonged periods of rainfall are common. In these hilly terrains, the soil cover, typically consisting of residual or colluvium soil, overlies bedrock and exhibits high matric suction values above the groundwater table.

To simulate the effects of rainfall triggering landslides in susceptible areas, it is imperative to conduct a coupled hydro-mechanical analysis. Taiwan serves as a prime

doi:10.6342/NTU202301082

example of a geographical region that necessitates further research due to its unique combination of environmental challenges. Predominantly mountainous, Taiwan is routinely subjected to various natural hazards, such as earthquakes and seasonal typhoons. The intense rainfall associated with these seasonal storms frequently results in disasters such as landslides and debris flows, making the examination of rainfall and groundwater variation on slopes crucial to disaster analysis. There are various methodologies available to achieve slope stability, including altering slope geometry, utilizing reinforcement elements, or implementing structural components such as retaining piles. One technique for developing the experimental *p-y* curve has been proposed in a previous study (Meyer and Reese, 1979).

The standard design procedure for stabilizing piles consists of three main steps: (1) assessment of the additional resistance required to elevate the slope's safety factor to a desired value, (2) estimation of the resultant lateral force that each pile in a row can provide to counteract the movement of the slope's sliding layer, and (3) selection of the type and quantity of piles and their optimal placement in the slope to ensure that the resultant lateral force meets or exceeds the additional resistance. As demonstrated in a case study (Kahyaoglu et al., 2017), the interplay of several factors, including the geometry of the sliding mass, the depth of the sliding soil, the deformation modulus of the stationary soil, and the relative movement between the soil, the piles, and adjacent piles, significantly influences the soil loads acting on piles and pile displacements.

Numerous studies (Galli et al., 2017; Hassiotis et al., 1997; Heidari & El Naggar, 2017; Ito et al., 1981; Ozcelik et al., 2012; Poulos, 1995; Pradel et al., 2010; and Zhang & Wang, 2017) have proposed various analytical approaches for designing and quantifying the behavior of slopes stabilized by rigid piles. The evaluation of pile response to ground movement can be classified into pressure-based, displacement-based,

doi:10.6342/NTU202301082

and numerical methods. For such cases, the three primary failure envelopes include "short," "intermediate," and "flow" modes as shown in Figure 2.1 and 2.2. In the intermediate mode, soil failure transpires along the entire pile length, whereas in the short and flow modes, soil reaches its ultimate strength exclusively in the stable and sliding soil layers, respectively.

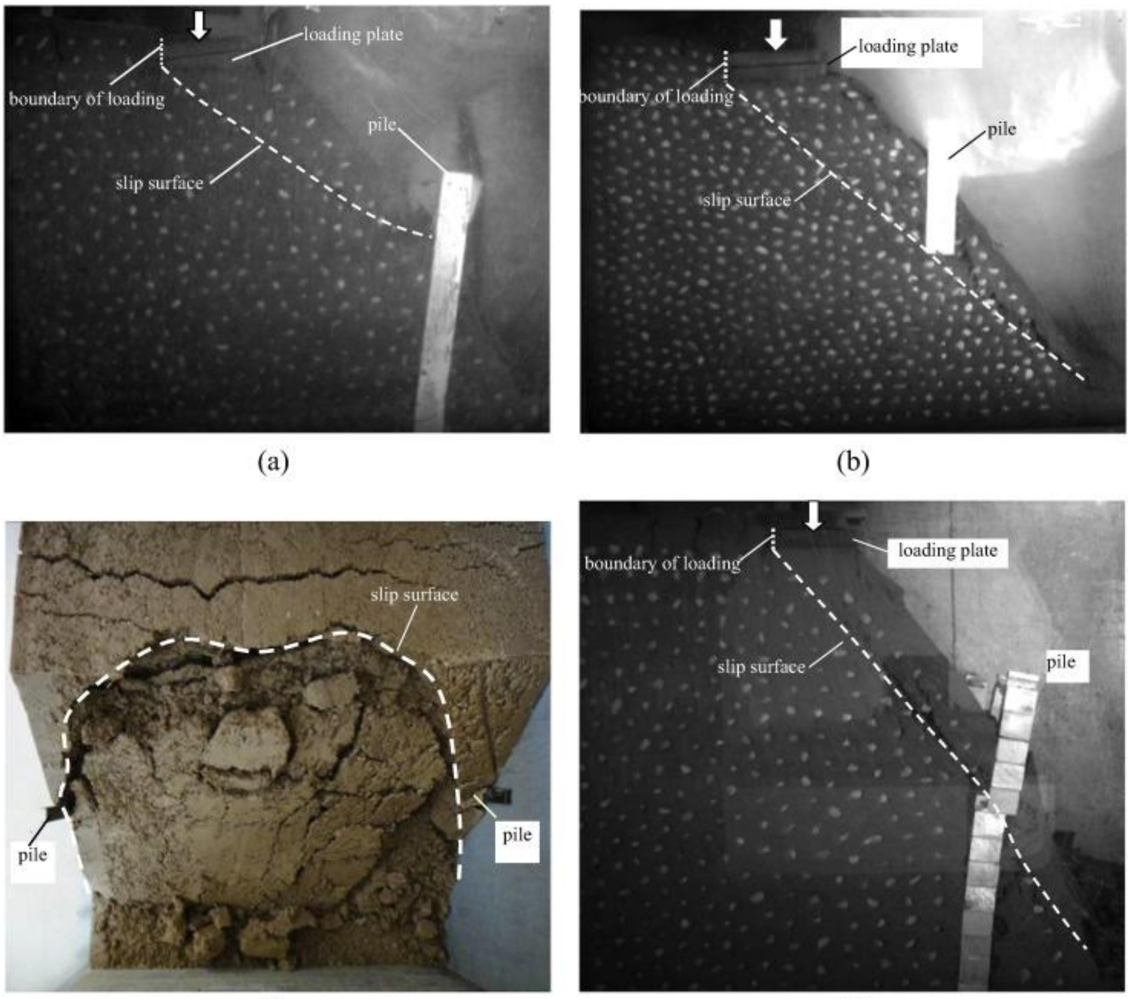

Figure 2.1: Photographs of the different failure modes conducted in experimental study (Zhang & Wang, 2017)

doi:10.6342/NTU202301082

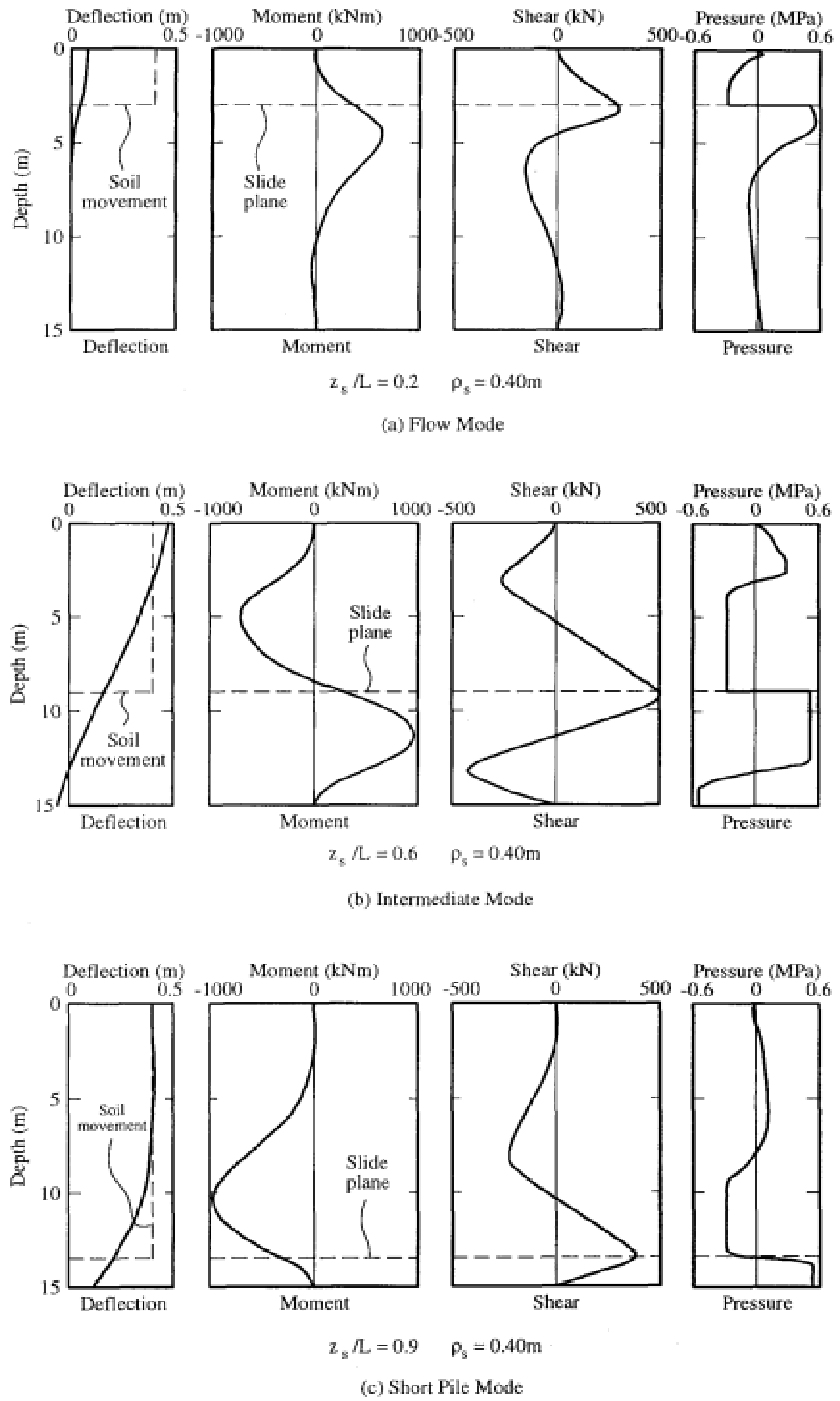

Figure 2.2: Pile behaviour characteristics for various failure modes (Poulos, 1995)

doi:10.6342/NTU202301082

Rowe and Poulos (1979) investigated the influence of various factors, such as pile stiffness (*EI*) and differing pile arrangements, to understand their effects on slope performance, displacement ratio, and maximum bending moment. The study found that the introduction of piles most significantly affected deformation at the slope's toe, while it minimally influenced the lateral movement of the upper part of the slope. This outcome is attributed to the fact that piles, even those with high stiffness, tend to move with the soil. While they provide some degree of restraint against deep-seated movement, the rotation of the pile about the base still permits significant deformation of the slope.

The efficacy of piles in mitigating deformation and enhancing slope stability is contingent upon both the pile stiffness and the fixity of the pile. The study also found that the effect of piles on slope deformation and stability increases only gradually with increasing pile stiffness. Consequently, it might be necessary to employ exceedingly stiff piles to achieve a substantial improvement in slope performance.

Ausilio et al. (2001) and Hasiotis et al. (1997) corroborated that the placement of piles for optimal safety factors should be in the upper middle part of the slope. This placement affirms the notion that a retaining structure situated near the toe or the crest of the slope can only restrain a small mass of soil. This location aligns with the assumption that piles are subject to lateral loading (Figure 2.3).

doi:10.6342/NTU202301082

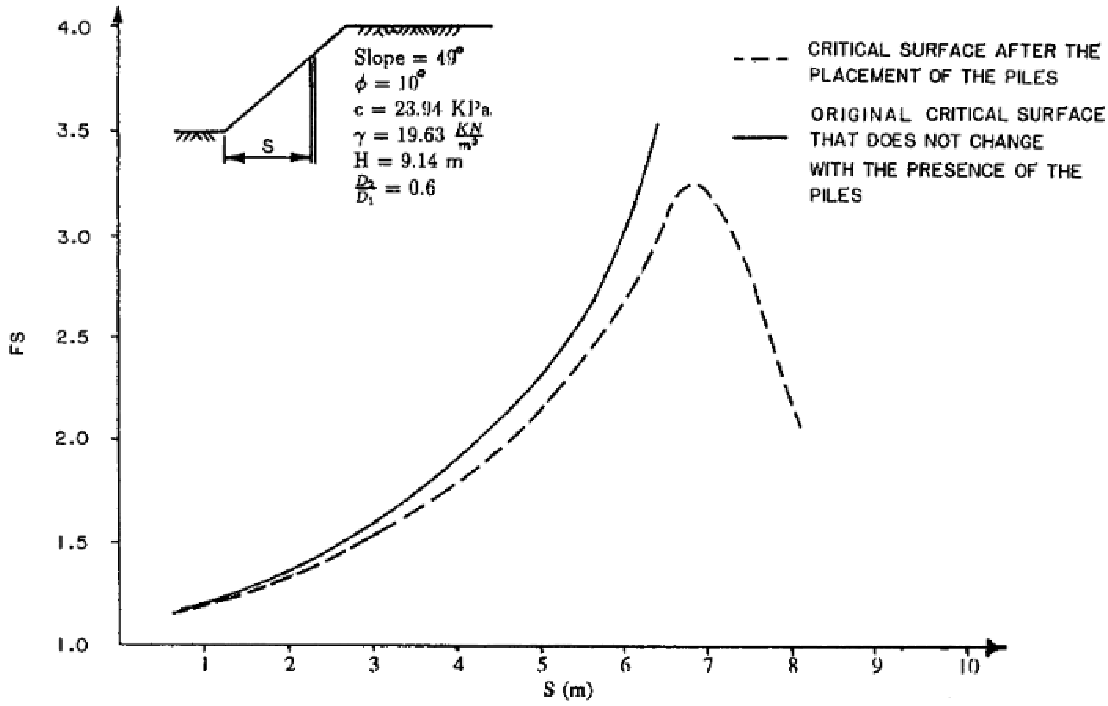

Figure 2.3: Effect of pile location on factor of safety of steep slope (Hasiotis et al., 1997)

Galli et al. (2017) examined the impact of spacing on the stability of slopes stabilized with rigid piles. It was found that when the spacing (*S*) is significantly larger than the pile diameter (*D*), interaction between piles is not possible. Consequently, the distribution of horizontal soil stress acting around the pile shaft corresponds to that of an isolated pile subject to a horizontal load. Conversely, when the spacing (*S*) is reduced to the value of the diameter (*D*), the result resembles a continuous sheet pile, and the soil stress distribution at failure tends to be uniform. This distribution reaches a condition of passive earth pressure on the uphill side and active earth pressure on the downhill side of the sheet pile.

Between these two extremes, there exists a range of spacing (*S*) values where the horizontal stress distributions of neighboring piles begin to overlap. This overlap generates the so-called "arching" effect (Figure 2.4 and Figure 2.5). This finding aligns

doi:10.6342/NTU202301082

with the results of Lee et al. (1995). Furthermore, it was discovered that soil modulus and pile stiffness have little or no impact on pile failure response and, consequently, on the stability of the pile-stabilized slope, since pile failure occurs at the ultimate condition.

Liang and Zeng (2002) confirmed the existence of the arching effect and demonstrated that it could significantly enhance slope stability, depending on the conditions of the soil and pile. Hajiazizi et al. (2018) proposed an analytical methodology for computing the forces exerted on piles. This approach was substantiated through both numerical simulations and empirical models.

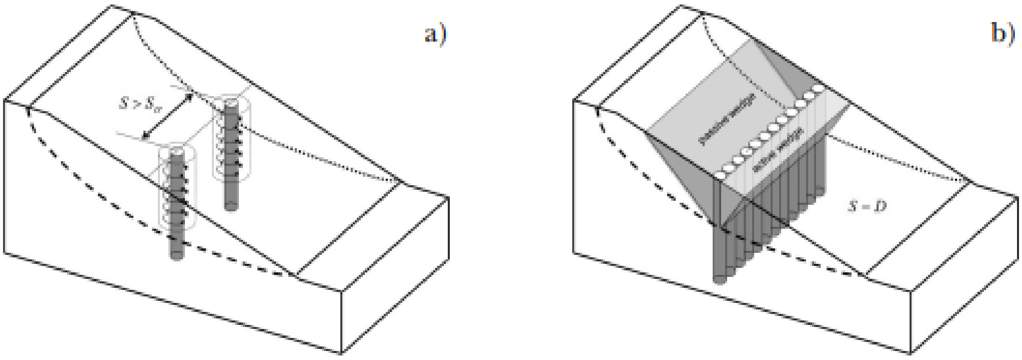

Figure 2.4: Influence of pile spacing on soil failure mechanisms around the piles: (a) isolated piles; and (b) continuous sheet pile (Galli et al., 2017)

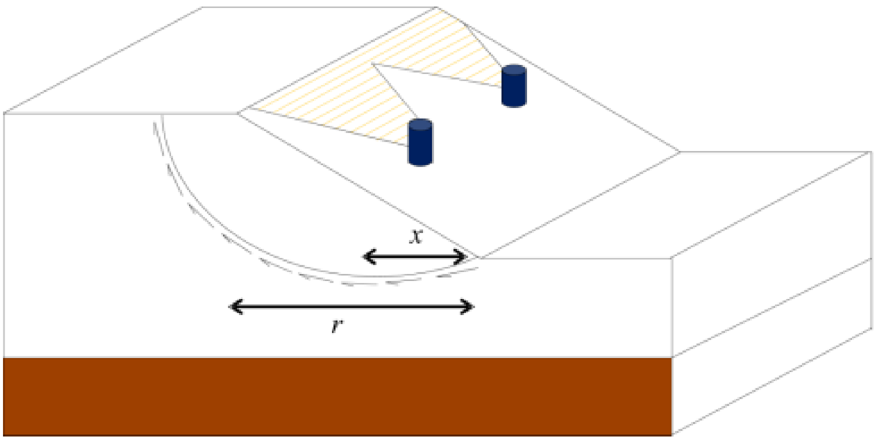

(a)

doi:10.6342/NTU202301082

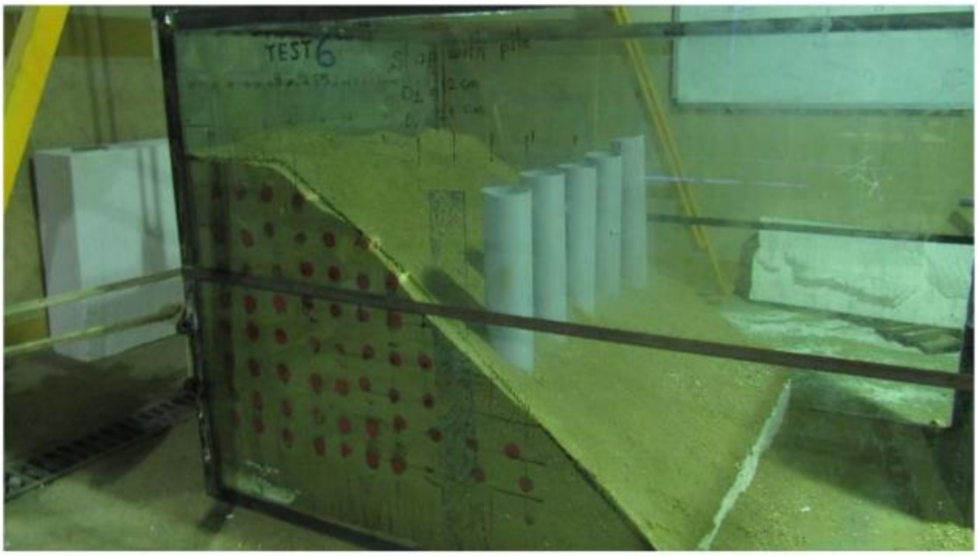

(b)

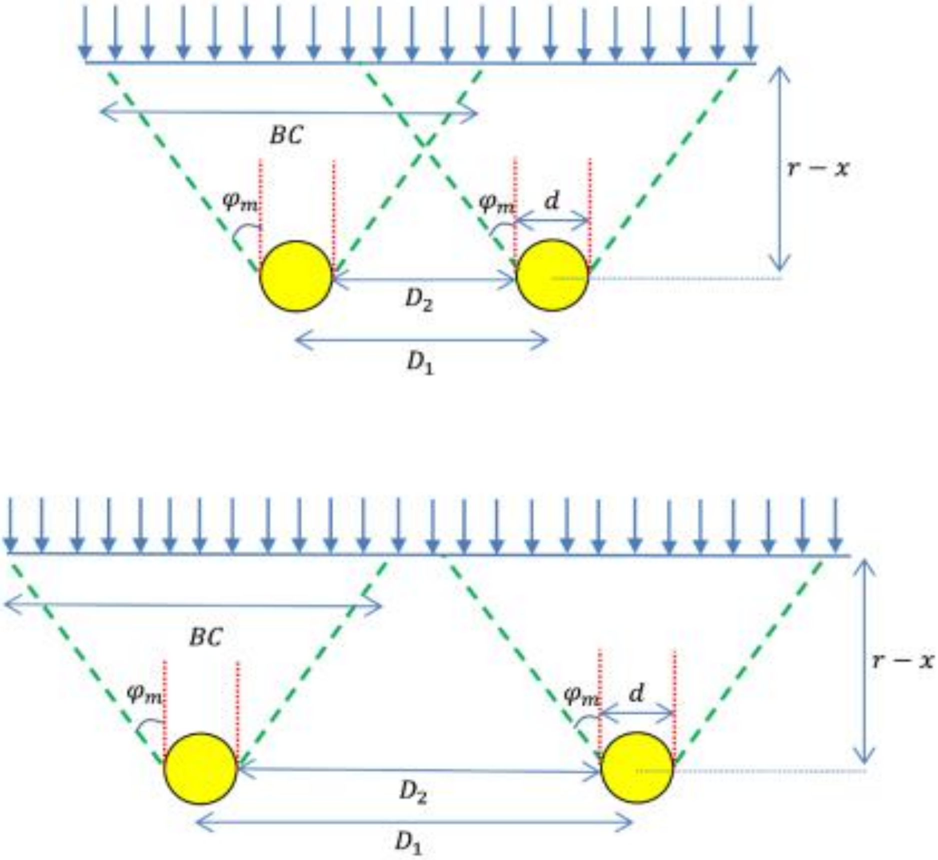

(c)

doi:10.6342/NTU202301082

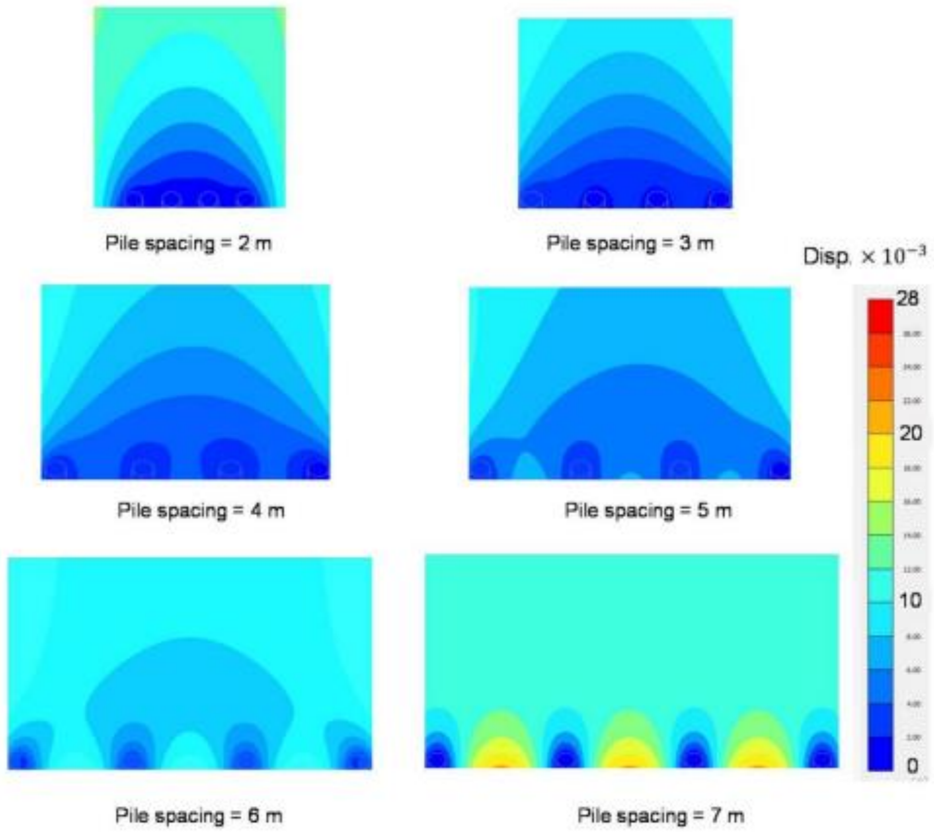

(d)

Figure 2.5: Experimental and numerical approach to evaluate stability of pile-stabilized slope: (a) numerical model; (b) experimental model; (c) influence of S/D ratio on force distribution; and (d) influence of pile spacing on arching effect (Hajiazizi et al., 2018)

Soil undergoes cycles of wetting and drying processes, developing matric suction in the process. Instances of rainfall can gradually reduce this matric suction, leading to a saturated state where pore water pressure escalates. This increase in pressure reduces the available shear strength needed to resist failure. Proper installation of horizontal or vertical drainage systems within the slope can mitigate this issue by delaying the wetting process and maintaining a relative hydraulic permeability substantially lower than the unit value. Gui and Alebachew (2022) elucidated the generation and dissipation of excess pore-water pressure, as well as the responses of the pile under various loading conditions. It was observed that different loading rates on the pile resulted in varying degrees of

doi:10.6342/NTU202301082

excess pore-water pressure generation. Furthermore, the generation of excess pore-water pressure significantly impacted the response of a laterally loaded single pile. The full combined formulation of soil–structure and fluid metaphysics may be represented by Biot's system of equations:

$$
\begin{aligned}
&G\nabla^2 u + \frac{G}{1-2\nu}\left(\frac{\partial^2 u}{\partial x^2} + \frac{\partial^2 v}{\partial x \partial y} + \frac{\partial^2 w}{\partial x \partial z}\right) = F_x - \alpha_B \frac{\partial p}{\partial x} \\
&G\nabla^2 v + \frac{G}{1-2\nu}\left(\frac{\partial^2 u}{\partial x \partial y} + \frac{\partial^2 v}{\partial^2 y} + \frac{\partial^2 w}{\partial x \partial z}\right) = F_y - \alpha_B \frac{\partial p}{\partial x} \\
&G\nabla^2 w + \frac{G}{1-2\nu}\left(\frac{\partial^2 u}{\partial x \partial y} + \frac{\partial^2 v}{\partial x \partial y} + \frac{\partial^2 w}{\partial^2 z}\right) = F_z - \alpha_B \frac{\partial p}{\partial x}
\end{aligned}
\tag{2.1}
$$

where G is the shear modulus; u, v, w is the displacement corresponding to the x, y, z direction, respectively; F_x, F_y, F_z is the body force in the respected direction, α_B is the Biot–Willis coefficient, and p is the fluid or pore pressure.

2.2 Performance of granular columnar systems

Non-traditional applications of Geosynthetic Encased Columns (GEC) include support for roadway or bridge approach embankments over unstable soils, structural support such as bridge approaches and retaining walls, slope stabilization, and mitigation of liquefaction. Key design parameters encompass the limit of the treatment area, depth of treatment, replacement ratio, column layout pattern, column diameter, and column spacing.

Alexiew et al. (2012) highlighted that the end product of a GEC design is a flexible, ductile, largely self-regulating, and hence robust system, which can be a significant advantage in many cases. This self-regulating load-bearing behavior implies that, should the columns yield, the load gets redistributed to the soft stratum, thereby increasing the ground resistance supporting the columns, leading to a subsequent load redistribution back into the columns.

doi:10.6342/NTU202301082

Ali et al. (2012), Gniel and Bouazza (2009), Hong et al. (2016), Hosseinpour et al. (2014), Murugesan and Rajagopal (2006), Nagula et al. (2018), Pulko et al. (2011), and Wu and Hong (2009) have discussed the failure modes and positive outcomes achieved through the use of GEC for ground stabilization, as opposed to conventional sand or stone columns. These studies have utilized experimental, numerical, and full-scale model tests to validate their arguments.

Cengiz et al. (2019) identified dominant failure modes for granular columns, namely, shear and bending failure modes under static and cyclic lateral loading conditions. Additionally, bulging and punching failures, which are more subjected to vertical loads, were highlighted. A GEC stabilized slope with sufficient reinforcement stiffness is likely to experience local bending of the column. This bending typically occurs within the vicinity of the shear plane or failure surface passing through the column. Apart from the evident shear resistance component provided by the column acting on the shear plane, a secondary reinforcement mechanism is triggered by the presence of the column. The column is postulated to act as a dowel resisting the relative movement of soil bodies on either side of the shear plane, leading to a buildup of soil pressure around the column's periphery. This concentration of horizontal stress and its distribution across the cross-section is commonly known as the arching effect, where the movement of soil particles and its associated stress arch over non-mobilized sections of structures. Consequently, the driving force exerted on the soil mass between the piles is reduced, leading to a higher safety factor for the slope.

2.2.1 Characteristics of slope stabilized with granular column

In the research by Hajiazizi et al. (2020), an experimental study was performed on a two-layer sand earth slope. This slope was saturated through precipitation, and its

doi:10.6342/NTU202301082

eventual failure over time post-saturation was observed. The placement of stone columns at various locations followed by the saturation of the earth slope through precipitation yielded logical and satisfactory results that could effectively guide designers. All the experimental models were simulated and compared using the 3D Finite Difference Method (3D FDM), and the outcomes were found to be consistent with each other (Figure 2.6).

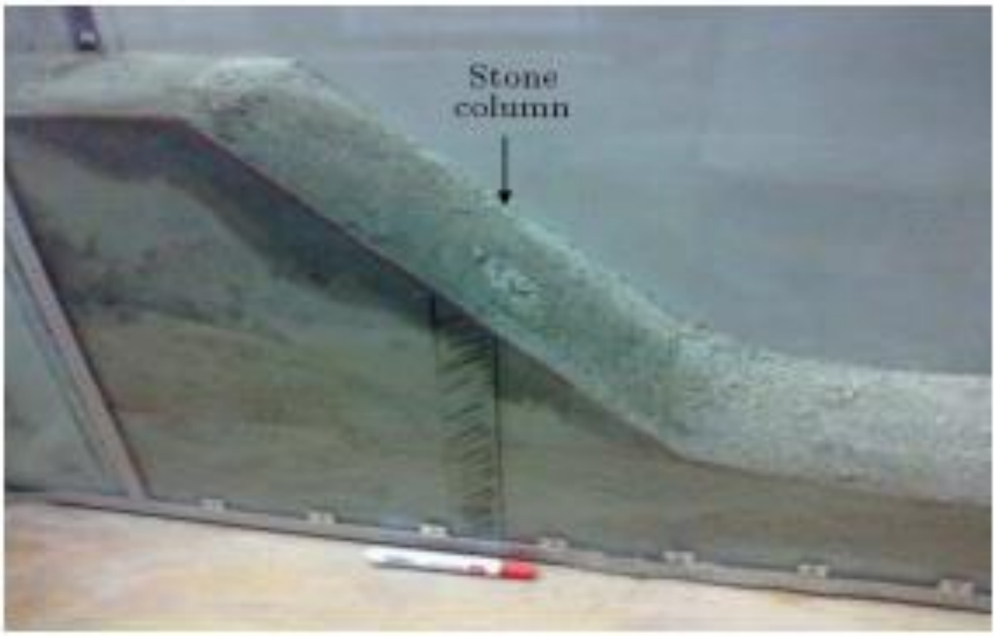

Figure 2.6: Experimental approach to evaluate stability of stone column-stabilized slope subjected to rainfall (Hajiazizi et al., 2020)

For a more accurate evaluation of the forces acting on the piles, the arching effect between adjacent piles must be considered. The most advantageous pile location, in terms of the footing's bearing capacity, is at the slope crest. This could be attributed to the fact that the passive wedge under the footing is relatively shallow. The model piles disrupt the failure surface, and the mobilized passive resistance increases when the pile row is situated closer to the slope crest. While other pile row positions may enhance the overall stability of the slope itself, they do not intersect with the failure plane. As a result, they

doi:10.6342/NTU202301082

cannot prevent or reduce the lateral deformations of soil particles under the footing and near the slope.

The experimental studies conducted Naderi et al. (2020) and Vekli et al. (2012) explored the impact of the *S/D* ratios (the ratio of the distance between the vertical axes of Stone Columns (SCs) to the diameter of SCs) on several key aspects of geotechnical engineering (Figure 2.7). These aspects included slope stability, ultimate bearing capacity, and the settlement of a footing situated on top of the slope.

(a)

doi:10.6342/NTU202301082

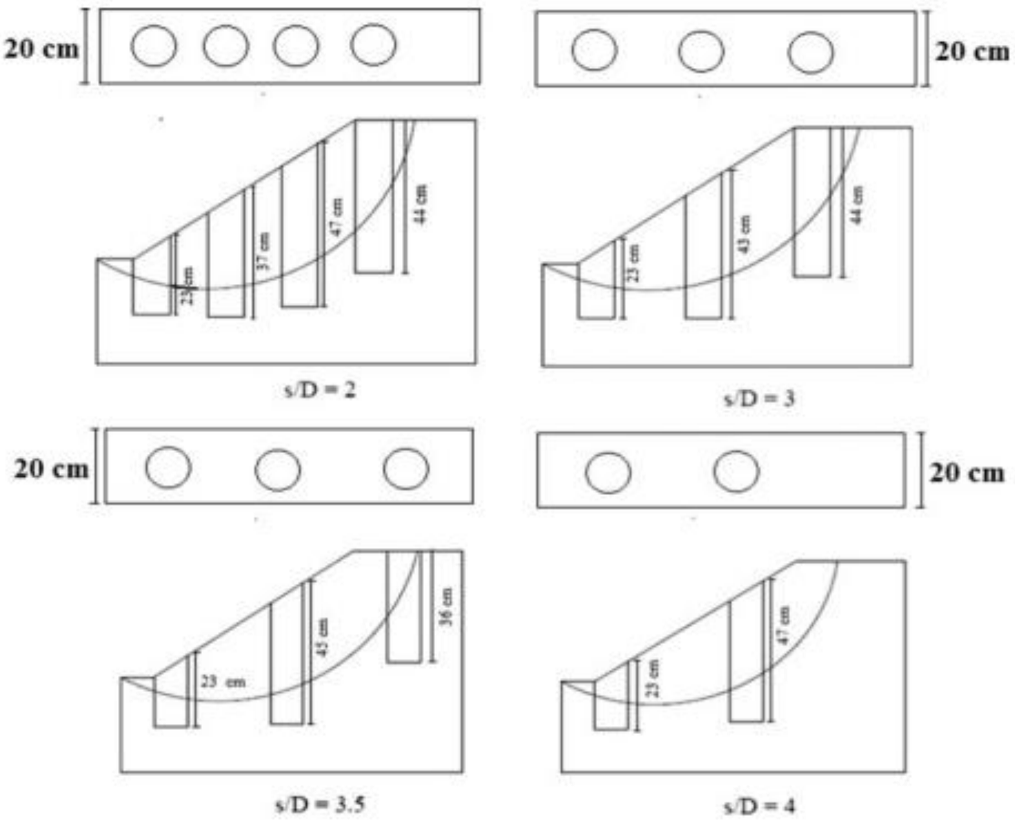

(b)

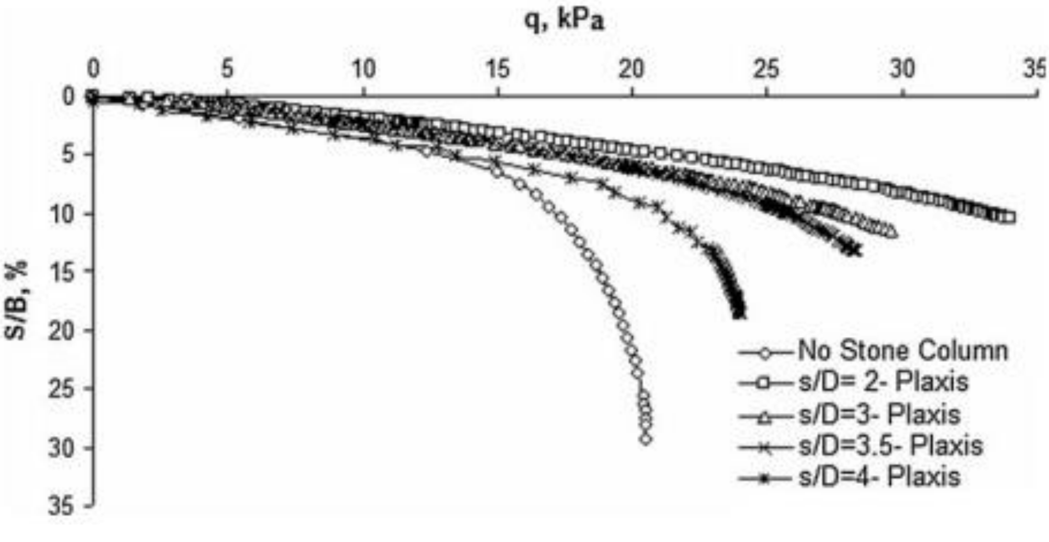

(c)

Figure 2.7: Experimental and numerical investigation of stone column stabilized slope subjected to loading: (a) experimental setup; (b) application with various *S/D* ratio; and (c) settlement reduction ratio with *S/D* ratio (Vekli et al., 2012)

doi:10.6342/NTU202301082

2.2.2 Characteristics of slope stabilized with geosynthetic encased granular column

In their respective studies, Araujo et al. (2009) and NYSDOT (2013) concluded that the use of Geosynthetic Encased Columns (GECs) provides distinct advantages over traditional granular columns in scenarios involving the structural collapse of surrounding soil. These GECs offer temporary yet highly effective vertical drainage, allowing for rapid construction due to the dissipation of excessive pore water pressure. Furthermore, GECs can be utilized to decrease seepage or artesian forces that promote slope movement. Wu et al. (2009) corroborated these findings, indicating that encapsulating the granular column within a flexible sleeve enhances the stiffness and strength of the traditional granular column.

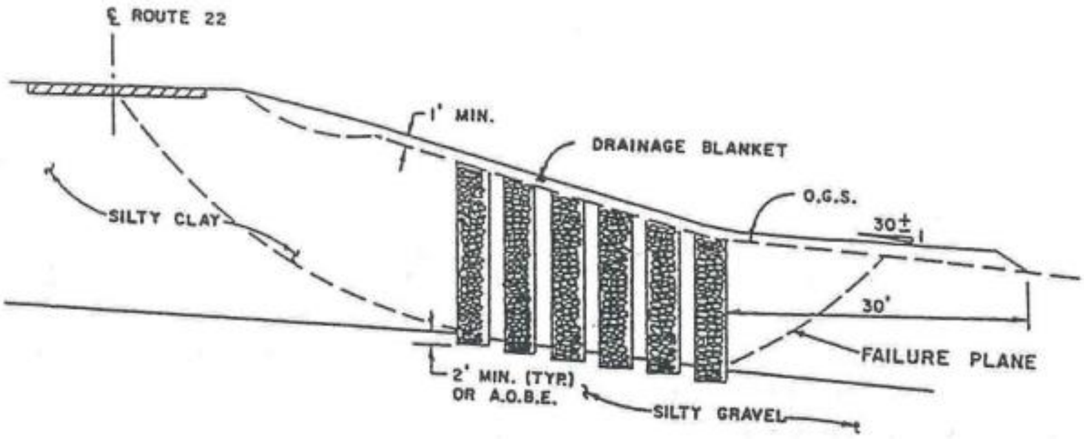

Figure 2.8: Elevation view of stone column supported embankment (NYSDOT, 2013)

Castro and Sagaseta (2013) demonstrated that stone columns or other rigid stabilizing structures might be inappropriate for extremely soft soils, which do not provide sufficient lateral confinement for the columns. For this investigation, the finite element code was employed to model the unit cell. The same boundary conditions and material properties used in the analytical solutions were applied to the numerical models

doi:10.6342/NTU202301082

for comparison purposes.

A 3D finite difference numerical study by Nasiri and Hajiazizi (2019) on the behavior of GECs in sand slope stabilization showed that the presence of GECs at the mid-point of the sand slope significantly enhanced stability compared to the ordinary stone column (OSC). This finding was verified by Hajiazizi et al. (2020), who determined the optimal pile or stone column location through a series of experiments involving the installation of stone columns at various locations and the saturation of the earth slope via precipitation.

Given that GEC stabilized slopes are subjected to shear stress, large shear box tests conducted by Chong et al. (2018) and Mohapatra et al. (2018) examined the behavior of GECs under lateral loads. Numerous direct shear tests were performed on granular columns, both with and without encasement, in a shear box. They found that as GECs did not shear completely, they continued to function as vertical drains due to the continuity of the flow path at large deformation (Figure 2.9). As a result, GECs could rapidly restore effective stresses post-earthquake by continuing to drain the liquefied ground, thereby preventing complete structural failure.

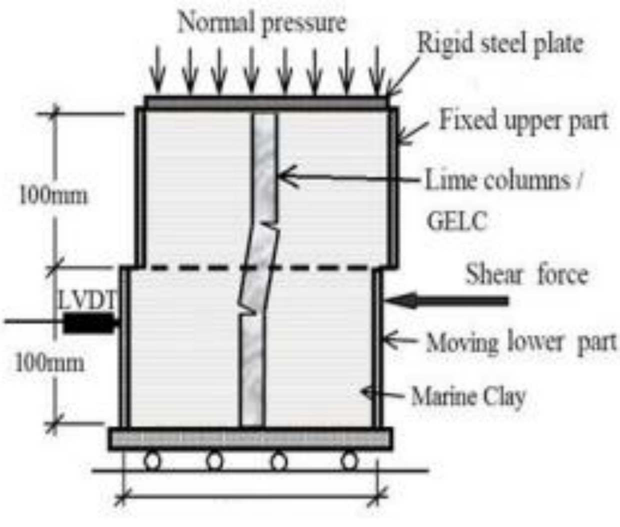

(a)

doi:10.6342/NTU202301082

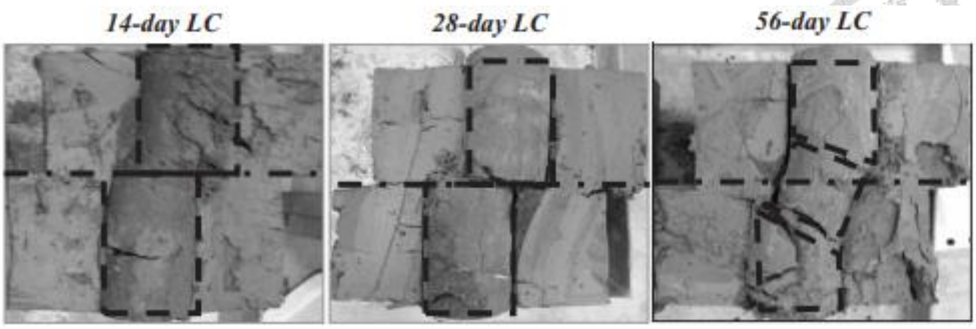

(b)

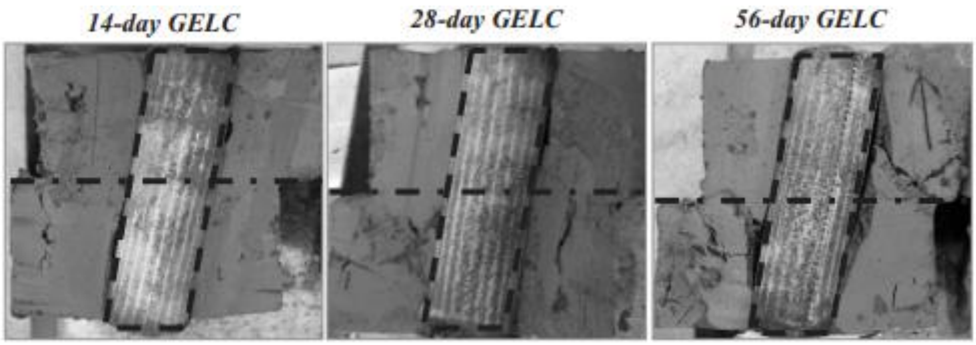

(c)

Figure 2.9: Experimental investigation of geotextile encapsulation on lime column under shear load: (a) large shear box test setup; (b) result of sample with 60mm line column without geotextile encasement; and (c) result of sample with 60mm line column without geotextile encasement (Chong et al. 2018)

Indraratna et al. (2013) highlighted that most of the imposed total stress is absorbed by the increased (excess) pore water pressure. As the excess pore pressure dissipates, progressive settlement of the soft clay and arching occur, resulting in an uneven distribution of vertical stress on the ground surface. In the case of GEC stabilized slopes, an uneven distribution of horizontal stress is anticipated prior to failure. Since slope failure is an instantaneous process, unlike ground improvement, clogging is highly unlikely. Likewise, the smearing effect, which results from installation in soil adjacent to the interface, can generally be disregarded.

doi:10.6342/NTU202301082

2.3 Similitude laws

The validation of numerical models using physical models is an essential part of geotechnical engineering research and practice. Numerical modelling, such as finite element is a powerful tool that uses mathematical equations to represent the physical behavior of soils and structures under various conditions. However, the complexity of soil behavior and the inherent uncertainties in soil properties often make it difficult to completely capture reality in numerical models. To ensure accuracy, reliable predictions for design and analysis of the models, they must be validated against experimental data.

The study has been divided mainly in four parts such as (1) Geometrical Similarity, (2) Soil Parameters, (3) Reinforcement Parameters and, (4) Flexural Stiffness and Loading.

It can be established by the principle of dimensional analysis that main theory is Buckingham (1914). The main content of which is that form of an equation is independent of the unit of measurement. It can be simplified to relationship of some independent dimensionless products, assuming an equation containing n variables can be expressed in x_i form as:

$$F(x_1, x_2, x_3..............x_n) = 0 \tag{2.2}$$

According to Buckingham theory, any equation similar to the above can be formed into a new equation by the dimensionless product of n-r formula, that is

$$f(\pi_1, \pi_2.............\pi_{n-r}) = 0 \tag{2.3}$$

where π represents the dimensionless product consisting of several variables x_i, and r is the fundamental dimension in the original variable, for example x_1, x_2 and x_3 are length, mass and time respectively, these three are independent fundamental dimensions, then r = 3, other all n-3 variables can be derived from these fundamental dimensions Langhaar (1951), so if a physical quantity is derived from a group dimensionless product

doi:10.6342/NTU202301082

which is expressed as:

$$\pi_1 = \phi(\pi_2, \pi_3 ....\pi_n) \tag{2.4}$$

(1) Geometrical Similarity

The geometry of the reduced model of the reinforced retaining wall in this study remains the same as the shape size, but the length and width should be reduced by *N* times to maintain model similarity.

(2) Soil Parameters

The similarity ratios related to soil parameters in this study mainly include cohesion, friction angle and unit weight, among which the friction angle does not need to be reduced with dimension, and the original soil sample does not need to be reduced for unit weight. The cohesion is expressed as follows:

$$c = f(\rho, g, H) \tag{2.5}$$

Where, *g* is gravity; ρ is the density of the fluid; *H* is the height of the reinforced retaining wall.

According to the Buckingham π theory, it can be expressed as:

$$\pi_c = c\rho^a g^b H^c \tag{2.6}$$

Model similarity would be

$$(c/\rho g H)_m = (c/\rho g H)_p \tag{2.7}$$

$$(c)_m = \frac{1}{\lambda}(c)_p \tag{2.8}$$

(3) Reinforcement Parameters

The mechanical behavior of stiffeners in sandy soil layers can be represented by the following functions:

$$F(\rho, g, E, \nu, \phi, H, T_{ult}, J_{50\%}, \mathrm{P_r} ...) = 0 \tag{2.9}$$

where ρ is soil density, *g* is gravitational acceleration, *E* is soil elastic modulus, ν is

doi:10.6342/NTU202301082

soil Poisson ratio, φ is soil friction angle, H is the height of the reinforced retaining wall, T_{ult} is the ultimate tensile strength of the stiffener, $J_{50\%}$ is the stiffness of the reinforcement, P_r is the tensile resistance of the reinforcement. If this complete functional relationship is to be applied to any similar system, then it needs to be converted into a combination of a series of dimensionless terms based on the principle of dimensional analysis. For example, stiffness of the reinforcement $J_{50\%}$ (unit is kN/m) should be expressed in terms of ρ, g, H as the basis of dimension analysis, then

$$\pi = J_{50\%}\rho^a g^b H^c \tag{2.10}$$

Model similarity would be

$$\left(\frac{J_{50\%}}{\rho g H^2}\right)_m = \left(\frac{J_{50\%}}{\rho g H^2}\right)_p \tag{2.11}$$

$$\left(J_{50\%}\right)_m = \frac{1}{\lambda^2}\left(J_{50\%}\right)_p \tag{2.12}$$

$$\left(T_{ult}\right)_m = \frac{1}{\lambda^2}\left(T_{ult}\right)_p \tag{2.13}$$

(4) Rigidity and Loading

Stiffness of elastic model can be represented by the flexural rigidity (*EI*) and axial rigidity (*EA*). Disintegrating the components of which comes out to be modulus of elasticity (*E*), area moment of inertia (*I*) and area of cross section (*A*).

It is evident that shape transformation in a pile subjected to the lateral loading would be substantially resisted by flexural rigidity (*EI*), however contribution of axial rigidity (*EA*) cannot be ignored. Importantly, component of *EI* has to be scaled for 1-g reduced scale model from the prototype with additionally similarity conditions as mentioned previously.

Franke and Muth (1985) formulated the parameters involved in the laterally loaded piles and suggested following π-terms:

doi:10.6342/NTU202301082

$$F(H,d,l,h,EI,\gamma,d_G,E_G,C_G,\overline{G},\overline{K_0})=0 \quad (2.14)$$

Where, H = total applied lateral force applied on the pile, d = diameter of pile, l = length of pile underground, h = length of pile above the ground level, EI = flexural rigidity of pile, γ = unit weight of sand, E_G = modulus of elasticity of soil, C_G = crushing strength of soil, G = dimensionless parameters summarizing the influence of grain shapes, normalized grain size and grain size distribution, K_0 = grain configuration at the test begin, representing the fabric of sand.

Using the π-theorem from the dimensional analysis, above equation can be represented in dimensionless form as

$$f\left(\frac{H}{\gamma d^3},\frac{l}{d},\frac{h}{d},\frac{EI}{\gamma d^5},\frac{d_G}{d},\frac{E_G}{\gamma d},\frac{C_G}{\gamma d},\overline{G},\overline{K_0}\right)=0 \quad (2.15)$$

The flexural rigidity of pile of the model pile must satisfy the following condition

$$\left(\frac{EI}{\gamma d^5}\right)_m=\left(\frac{EI}{\gamma d^5}\right)_p \quad (2.16)$$

Using the geometrical similarity law, the ratio comes out to be

$$\left(EI\right)_m=\frac{1}{\lambda^5}(EI)_p \quad (2.17)$$

For the above case, it can be simplified by assuming same pile material for model and prototype.

Similarity can be supported by following dimensional analysis,

$$\pi=(EI)\gamma^a d^b \quad (2.18)$$

$$\pi=(EI)\gamma^{-1}d^{-5}=\frac{(EI)}{\gamma d^5} \quad (2.19)$$

Reddy and Ayothiraman (2015) have used below based on Lai et al. (2005) relationship for flexural rigidity (EI). However, conclusions may need to be verified with full-scale/centrifuge test data. However, it is noteworthy that Haeiri et al. (2012) justified

doi:10.6342/NTU202301082

that scaling factor λ^5 for *EI* of pile as suitable for modelling of the prototype.

$$(EI)_m = \frac{1}{\lambda^{4.5}}(EI)_p \tag{2.20}$$

For the case of distinct ratio of modulus of elasticity (λ_E) other than geometrical similarity of the prototype and model due to any experimental set-up constraints, all corresponding ration should be modified as suggested by Ramu et al. (2010).

The scaling factors derived in this research are consistent with the theoretical results proposed by Viswanadham and Konig (2004) for modeling geosynthetic materials, as summarized in Table 2.1.

Table 2.1: Summary of scaling factors for modeling

Applied Similarity Law Factors for input properties (*N* = 10)	
Properties	**Scaling Factor**
Slope Properties	
Total Length, *L* (m)	$1/N$
Total Width, *W* (m)	$1/N$
Total Height, *H* (m)	$1/N$
Slope Angle, θ (◦)	1
Reinforcement Properties	
Ultimate tensile Strength, T_{ult} (kN/m)	$1/N^2$
Axial Stiffness, $J_{50\%}$ (kN/m)	$1/N^2$
Rigid Pile Properties	
Modulus of Elasticity, *E* (MPa)	$1/N$
Flexural Rigidity, *EI* (kN-m^2)	$1/N^5$
Poisson's Ratio, ν	1
Diameter, *d* (m)	$1/N$
GEC Properties	
Modulus of Elasticity, *E* (MPa)	$1/N$
Flexural Rigidity, *EI* (kN-m^2)	$1/N^5$
Diameter, *d* (m)	$1/N$

doi:10.6342/NTU202301082

2.4 Hardening soil model

The Hardening Soil model is an advanced model for the simulation of soil behavior. As for the Mohr-Coulomb model, limiting states of stress are described using the friction angle ϕ, the cohesion c, and the dilatancy angle ψ. However, soil stiffness is described much more accurately by using three different input stiffnesses: the secant stiffness E_{50}, the unloading-reloading stiffness E_{ur} and the tangent oedometer loading stiffness E_{oed}. In contrast to the Mohr-Coulomb model, the Hardening Soil model also accounts for stress-dependency of stiffness. This means that all stiffnesses increase with pressure. The basic concept for the formulation of the Hardening Soil model is the hyperbolic relationship between the vertical strain, ε_1, and the deviatoric stress, q, in primary triaxial loading.

The quantities of E_{50} and q_f are defined as

$$E_{50} = E_{50}^{ref}\left(\frac{c\cos\varphi - \sigma'_3\sin\varphi}{c\cos\varphi + p^{ref}\sin\varphi}\right)^m \tag{2.21}$$

$$q_f = \frac{2\sin\varphi}{1-\sin\varphi}\left(c\cos\varphi - \sigma'_3\right) \tag{2.22}$$

where E_{50}^{ref} = secant stiffness corresponding to the reference confining pressure, ϕ = friction angle, p^{ref} = reference confining pressure, m = power series, σ_3' = minor principal stress. When $q = q_f$, the failure criterion is satisfied, and perfectly plastic yielding occurs. For the unloading-reloading and tangent oedometer loading stiffnesses, another stress-dependent stiffness modulus is used:

$$E_{ur} = E_{ur}^{ref}\left(\frac{c\cos\varphi - \sigma'_3\sin\varphi}{c\cos\varphi + p^{ref}\sin\varphi}\right)^m \tag{2.23}$$

$$E_{oed} = E_{oed}^{ref}\left(\frac{c\cos\varphi - \sigma'_3\sin\varphi}{c\cos\varphi + p^{ref}\sin\varphi}\right)^m \tag{2.24}$$

doi:10.6342/NTU202301082

The integral yield surfaces of the Hardening Soil model in the *p-q* plane and principal stress space are shown in Figure 2.11.

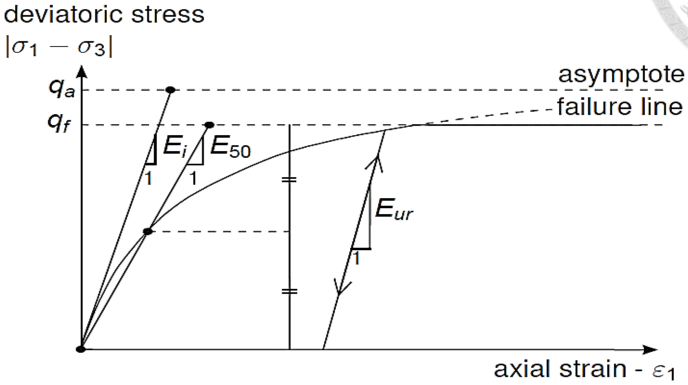

Figure 2.10: Hyperbolic stress-strain behavior of CD tests in the Hardening Soil model (Brinkgreve et al., 2019)

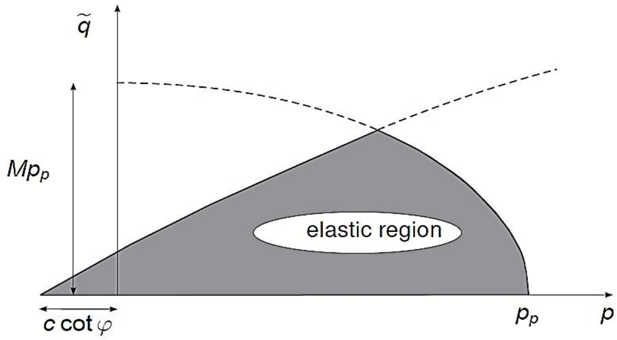

(a)

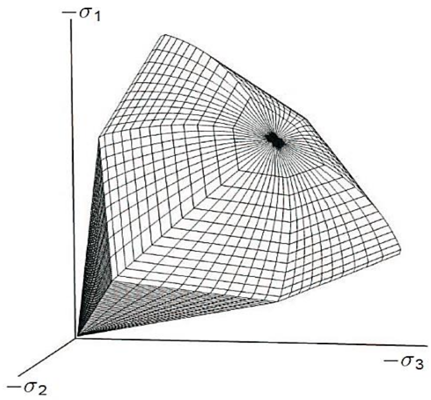

(b)

Figure 2.11: Yield surfaces of the Hardening Soil model in (a) *p-q* plane; and (b) principal stress space (Brinkgreve et al., 2019)

doi:10.6342/NTU202301082

2.5 Unsaturated soil mechanics

Unsaturated Soil Mechanics is integral due to the insights provided by the Soil-Water Characteristic Curve (SWCC), which establishes a conceptual relationship between the volume of water in the soil and its energy state. This discipline allows for the study of transition states, from residual to saturated conditions and vice versa, as well as the transfer of negative to positive pore pressure for safe design considerations. Unsaturated Soil Mechanics is particularly effective in studying rainfall infiltration and tsunami water infiltration. It is a key component in hydro-mechanical analysis, where both hydrological and mechanical parameters are variable. The study of water retention capacity in numerous capillaries and soil gradation, initially employed by agricultural engineers, is now widely utilized in geotechnical engineering. Thus, the principles of Unsaturated Soil Mechanics play a significant role in understanding and managing the behavior and performance of soil under various environmental conditions, thereby contributing to safer and more efficient design practices in geotechnical engineering.

Van Genuchten (1980) and Mualem (1976) model is adopted considering wider Range of suction and better captures the sigmoidal shape. Smooth transition at air-entry pressure and at residual condition approaching state. The soil-water characteristics and *k*-function curves are expressed as:

$$\Theta = \frac{\theta - \theta_r}{\theta_s - \theta_r} = \left[\frac{1}{1 + \left\{ \alpha \left(u_a - u_w \right) \right\}^n} \right]^{1-\frac{1}{n}} \tag{2.25}$$

$$k_{rel} = \frac{k}{k_s} = \Theta^{\frac{1}{2}} \left[1 - \left(1 - \Theta^{\frac{1}{(1-1/n)}} \right)^{1-1/n} \right]^2 \tag{2.26}$$

where Θ is the normalized volumetric water content; θ_s is the saturated volumetric water content; θ_r is the residual volumetric water content; (u_a - u_w) is the matric suction

doi:10.6342/NTU202301082

(where u_a and u_w are the pore air and pore water pressures, respectively); α and n are the curve fitting parameters in van Genuchten-Mualem's model; k_{rel} is the relative hydraulic conductivity; k is the hydraulic conductivity at any soil degree of saturation; k_s is the saturated hydraulic conductivity.

Conversely, the soil-water characteristics and k-function curve are expressed by Brinkgreve et al. (2019) as:

$$S(\phi_p) = S_{res} + (S_{sat} - S_{res})[1 + (g_a \mid \phi_p \mid)^{g_n}]^{g_c} \tag{2.27}$$

$$k_{rel}(S) = \max\left[(S_e)^{g_l} \left(1 - \left[1 - S_e^{\left(\frac{g_n}{g_n - 1}\right)} \right]^{\left(\frac{g_n - 1}{g_n}\right)} \right)^2, 10^{-4} \right] \tag{2.28}$$

Where, pressure head, ϕ_p is defined as:

$$\phi_p = -\frac{\psi}{\gamma_w} \tag{2.29}$$

Relationship between parameters g_c and g_n is defined as:

$$g_c = \left(\frac{1 - g_n}{g_n} \right) \tag{2.30}$$

Where ψ is matric suction; γ_w is unit weight of water.

Therefore, curve fitting parameters can be correlated as:

$$g_a(1/m) = \alpha.\gamma_w(1/kPa) \quad \text{and} \quad g_c = -m \quad \text{and} \quad g_n = n \tag{2.31}$$

Curve fitting parameters as expressed by Brinkgreve et al. (2019) are g_a, g_c and g_n.

doi:10.6342/NTU202301082

Chapter 3 Finite Element Analysis

In the current study, the development of finite element analyses is emphasized, with the aim of investigating the performance of Geosynthetic Encased Column (GEC) stabilized slopes when subjected to seepage. Owing to the intricate nature of the model, the application of specialized numerical software is necessitated for carrying out the computations. PLAXIS-3D, a leading-edge geotechnical engineering software, has been chosen for the assessment of slope stability. Advanced modeling capabilities are provided by this software, along with detailed insights into the performance of the stabilized slopes under diverse conditions. In subsequent sections, a comprehensive delineation of the numerical models employed, the boundary conditions defined, and the input material properties incorporated in the study will be provided. Through these descriptions, a more robust understanding of the methodologies utilized is sought to be fostered, thereby enhancing the credibility of the findings and conclusions derived from the analyses.

3.1 Input material properties

3.1.1 Soil properties

Table 3.1 provides a synopsis of the input soil properties incorporated in the Finite Element (FE) simulations. Four fundamental soil elements have been modeled, which are, (1) sloped soil; (2) encased soil; (3) impermeable rock; and (4) rigid pile. The sloped and encased soil are modeled as stress-dependent, hyperbolic, elastoplastic materials utilizing the hardening soil model (Schanz et al., 1999). Conversely, the Mohr-Coulomb model represents the rigid pile, while the impermeable rock is depicted through a linear elastic model. An exceedingly high stiffness characterizes the impermeable rock layer (E_{ref} = 24×10^{12} kN/m^2 and ν = 0.2), which limits the failure in the intact rock stratum. The

doi:10.6342/NTU202301082

properties considered for the rigid pile will be discussed in a forthcoming section.

The impact of the dilation angle and mesh fineness on the characteristics and paths of the failure surface, thereby influencing slope stability, has been scrutinized by Lin et al. (2020), and Manzari and Nour (2000). Consequently, the soil dilation angle, ψ, has been considered in the present study. The empirical relationship (i.e., $\psi = \phi' - 30°$) proposed by Bolton (1986) has been used to estimate the input value of ψ.

doi:10.6342/NTU202301082

Table 3.1: Input soil properties for numerical program

Soil Tests	Properties		Sloped Soil	Encased Soil
Sieve analysis and Hydrometer test	Soil classification (USCS)		SM	SP
	Mean grain size, D_{50} (mm)		0.28	0.98
	Fines content (%)		20	-
Atterberg Limit test	Liquid Limit, LL (%)		13	-
	Plastic Limit, PL (%)		6	-
Specific gravity test	Specific gravity, G_s		2.62	2.65
	Initial void ratio, e_{int}		0.9	0.7
Unit weight and water content properties				
Standard proctor test	Maximum dry unit weight, γ_{max} (kN/m^3)		18.10	16.36
	Minimum dry unit weight, γ_{min} (kN/m^3)		-	13.45
	Target dry unit weight, γ_d (kN/m^3)		13.58	15.30
	Relative compaction, R (%)		75	93
	Optimum water content, ω (%)		10.7	-
Relative density test	Relative density, D_r (%)		-	70
Modulus properties under stress-strain behaviour				
CIDC Triaxial test	Modulus of Elasticity, E^{ref}_{50} (kPa)		2,000	45,000
	Tangent oedometer loading modulus, E^{ref}_{oed} (kPa)		1,300	45,000
	Unloading-reloading modulus, E^{ref}_{ur} (kPa)		10,000	135,000
Shear strength properties				
CD Direct shear test	Effective cohesion, c' (kPa)	As-compacted	2.5	0
		Saturated	0	0
	Effective friction angle, ϕ' ($\circ$)	As-compacted	30.5	39.2
		Saturated	28.8	34.7
	Dilation angle, ψ ($\circ$)		-	9.2
Hydraulic properties				
Falling head/Constant head permeability test	Saturated hydraulic conductivity, k_{sat} (m/s)		1.024×10^{-5}	1.412×10^{-3}

doi:10.6342/NTU202301082

Soil Tests	Properties	Sloped Soil	Encased Soil
Interface properties with geotextile			
CD Interface direct shear test	Interface frictional angle, δ (°)	22.7	27.4
	Efficiency factor, E_{φ}	0.71	0.63
Interface properties with rock			
CD Interface direct shear test	Interface frictional angle, δ (°)	19.8	-
	Efficiency factor, E_{φ}	0.61	-

doi:10.6342/NTU202301082

The density of the sloped soil is maintained at 75% relative compaction, which is compacted at an optimal moisture content (OMC) of 10.7%. Based on numerous field and laboratory tests conducted on 53 selected samples to discern the properties of colluvium soil, Soralump et al. (2021) postulated that the soil exhibits plastic behavior. This implies that the soil possesses a high propensity to transition from a plastic to a liquid state. Under such circumstances, the soil void ratio could exceed 1 ($e \geq 1.0$), potentially leading to substantial deformation during saturation due to seepage. This suggests that maintaining an excessively low relative compaction can result in the violation of the ordinary plane strain condition of both the numerical and experimental models. The ordinary plane strain condition, as maintained in the numerical model, can be articulated as:

$$
\begin{aligned}
\varepsilon_x &= -\frac{\partial u}{\partial x} \neq 0 \\
\varepsilon_y &= -\frac{\partial v}{\partial y} = 0 \\
\varepsilon_z &= -\frac{\partial w}{\partial z} \neq 0
\end{aligned}
\tag{3.1}
$$

$$
\begin{aligned}
\gamma_{xy} &= -\left(\frac{\partial v}{\partial x} + \frac{\partial u}{\partial y}\right) = 0 \\
\gamma_{yz} &= -\left(\frac{\partial v}{\partial z} + \frac{\partial w}{\partial y}\right) = 0 \\
\gamma_{zx} &= -\left(\frac{\partial w}{\partial x} + \frac{\partial u}{\partial z}\right) \neq 0
\end{aligned}
\tag{3.2}
$$

Where ε represents the principal strain in respective direction; γ represents the shear strain in respective direction. ε_x, ε_z, and γ_{zx} are in-plane strain condition.

doi:10.6342/NTU202301082

The density of the encased soil is established at a 70% relative density, a recommendation advocated by Castro and Sagaseta (2013) as the ideal relative density achievable by machinery during installation. This consideration is particularly relevant for granular soil material, reflecting its unique physical properties and behavior during compaction.

The soil employed in this experiment, the properties of which are detailed in Table 3.1, was classified in accordance with the Unified Soil Classification System (USCS). The grain size distribution curve of the test soil is depicted in Figure 3.1. It is significant to note that all the soil properties were evaluated through laboratory experiments, ensuring accurate measurement and verification of the soil properties. This rigorous testing protocol bolsters the reliability of the study's findings and its applicability to real-world geotechnical scenarios.

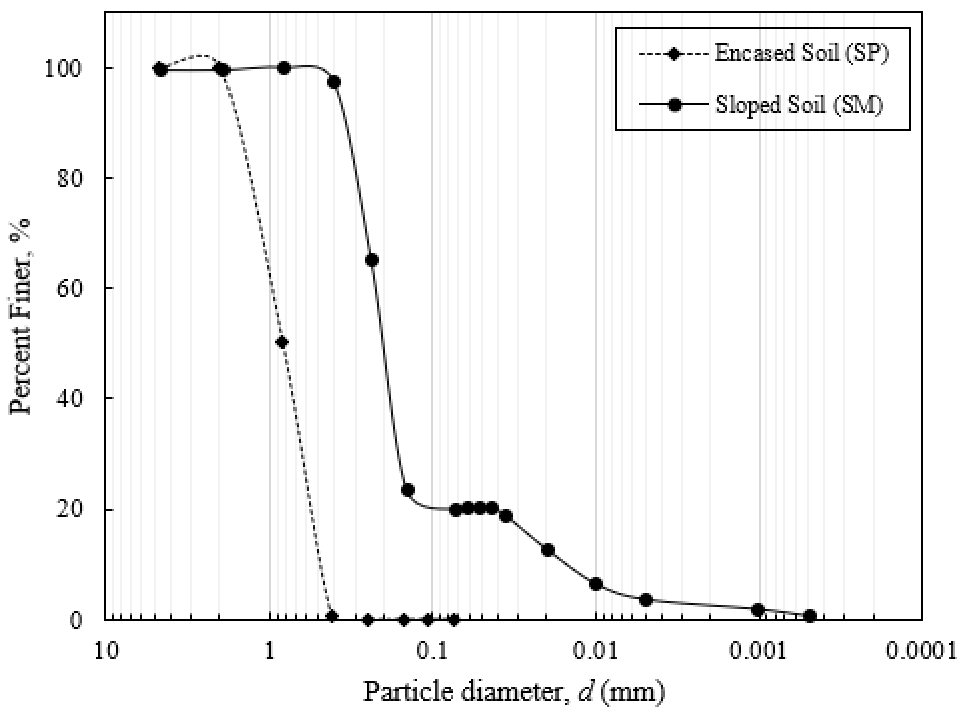

Figure 3.1: Grain size distribution curve for tested soil

doi:10.6342/NTU202301082

The input properties pertaining to soil shear strength and soil modulus are initially calibrated from the consolidated-drained triaxial compression tests. Figures 3.2 and 3.3 display the calibration results, presenting a comparison of the measured and predicted stress-strain-volumetric strain curves for both sloped and encased soil. A strain-softening behavior was noted in the stress-strain curve under high confining pressure. Despite this, considering strain-softening behavior within the numerical model predicated on the hardening soil model presents a challenge. A contrasting behavior was observed in the two soil types: while the encased soil exhibited brittle characteristics, the sloped soil demonstrated elastic behavior. These distinctions have significant implications for the understanding of their respective behaviors under different conditions and their optimal use in slope stabilization.

doi:10.6342/NTU202301082

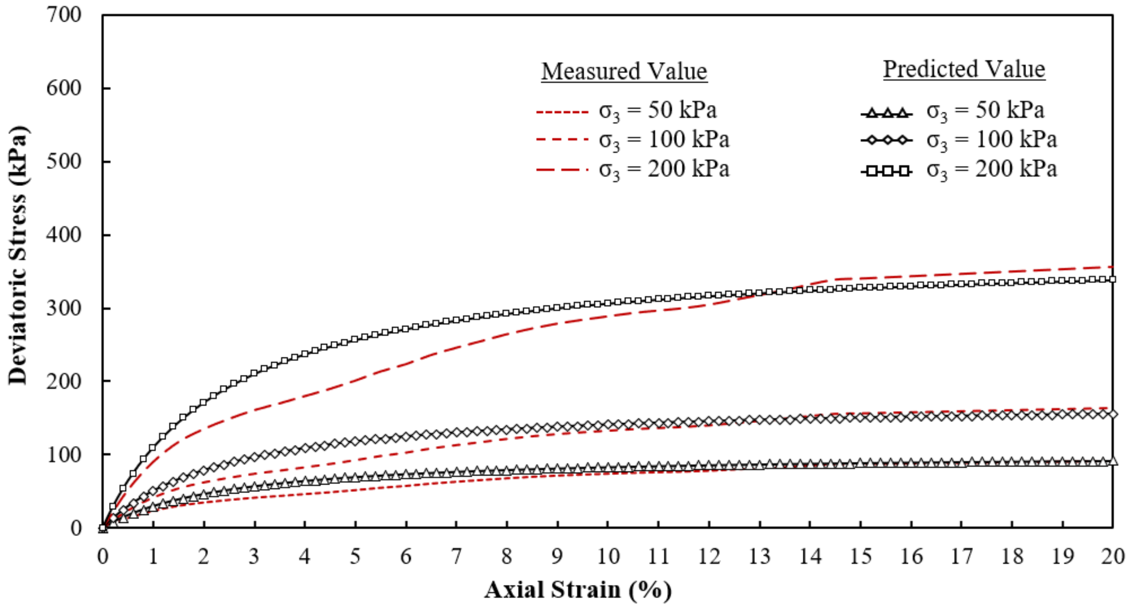

(a)

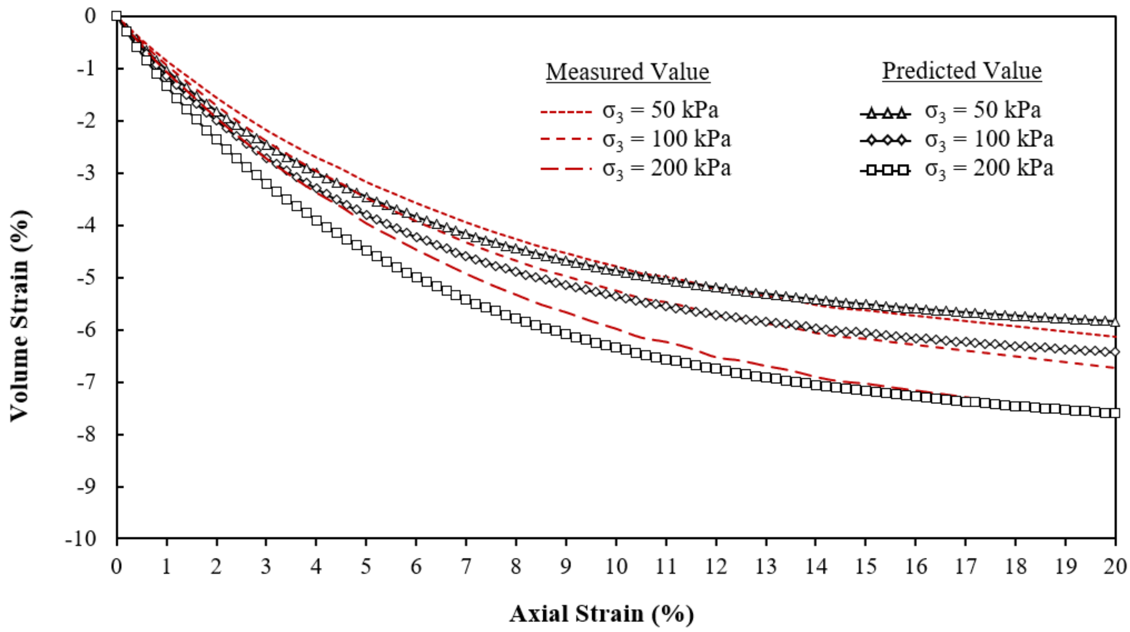

(b)

Figure 3.2: Material calibration by triaxial consolidated-drained test results of the sloped soil: (a) deviatoric stress vs. axial strain; and (b) volumetric strain vs. axial strain

doi:10.6342/NTU202301082

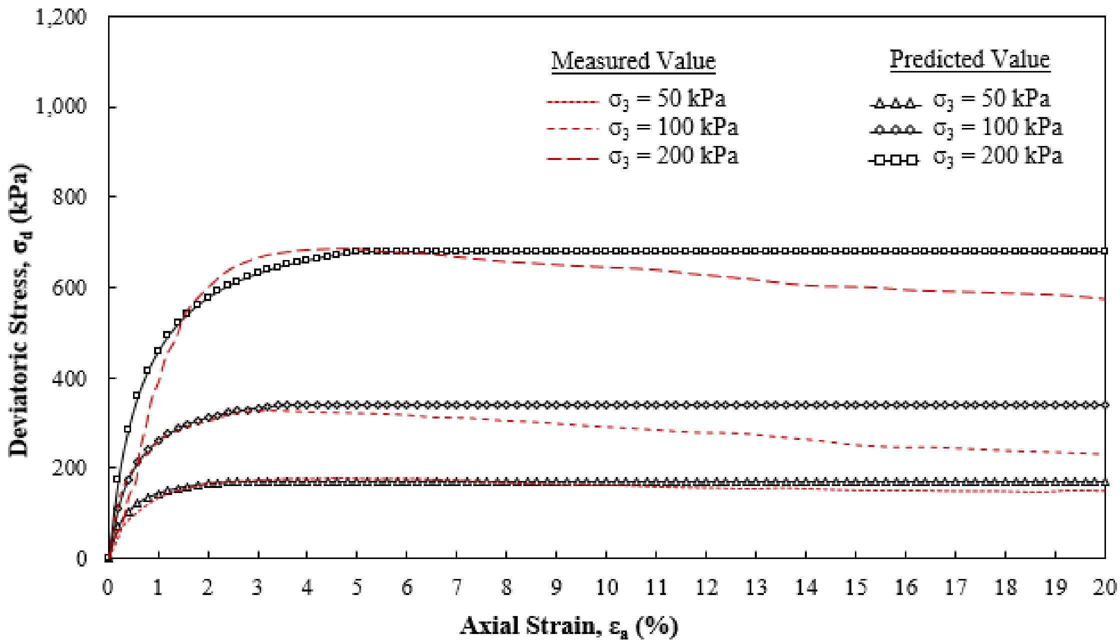

(a)

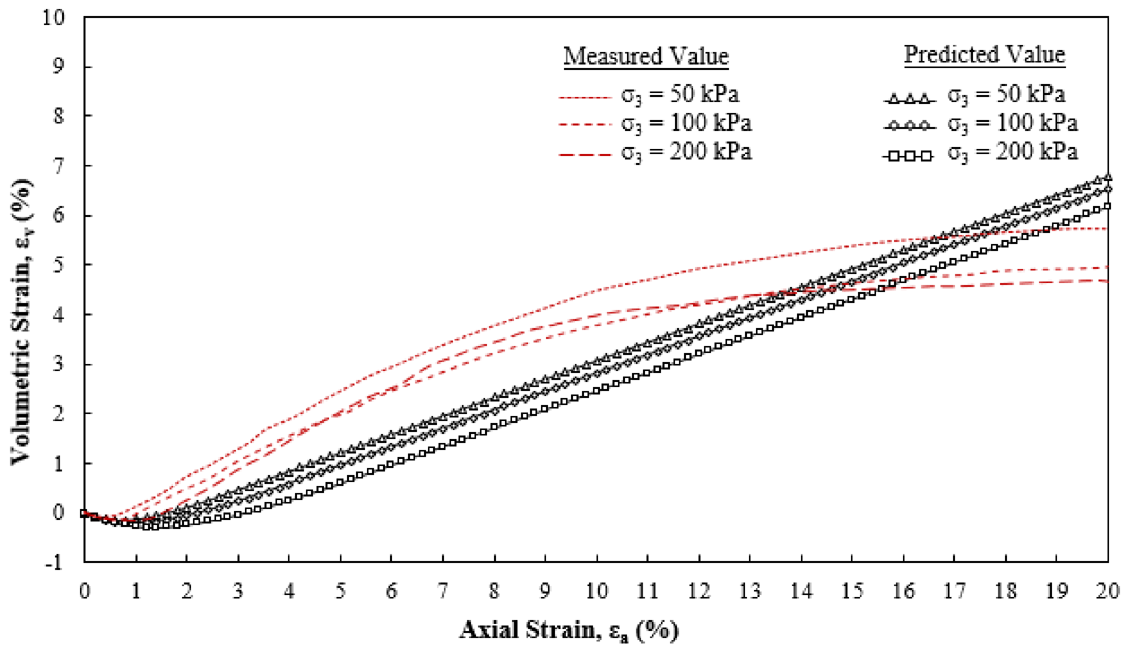

(b)

Figure 3.3: Material calibration by triaxial consolidated-drained test results of the encased soil: (a) deviatoric stress vs. axial strain; and (b) volumetric strain vs. axial strain

doi:10.6342/NTU202301082

Due to the soil's initial state being unsaturated, the hydraulic properties of the unsaturated soil were defined. The transition from an unsaturated to a saturated state was observed during the seepage infiltration process. An unsaturated soil zone allows for the coexistence of air, water, and the soil skeleton. Matric suction, which alters with the soil water content, is a key physical variable in unsaturated soils. It is observed that as matric suction value decreases, there is a corresponding reduction in soil strength.

A pressure plate extractor test was performed on the sloped soil using a 5-bar ceramic pressure plate and the weighting-outflow method, as outlined by ASTM D6836 (2008). To determine the unsaturated soil parameters for sloped soil, a curve-fitting method based on the Van-Genuchten model was utilized. The soil water characteristics curve (SWCC) and *k*-function characteristics curve results for the tested and calibrated sloped soil are depicted in Figure 3.4.

The saturated volumetric and residual volumetric water content were approximately 45% and 5.85%, respectively. The initial volumetric water content of the test was 19 m^3/m^3, corresponding to a matrix suction of 180 kPa. These details underline the importance of understanding and defining the hydraulic properties of unsaturated soil, which directly impact its behavior during saturation and load application.

doi:10.6342/NTU202301082

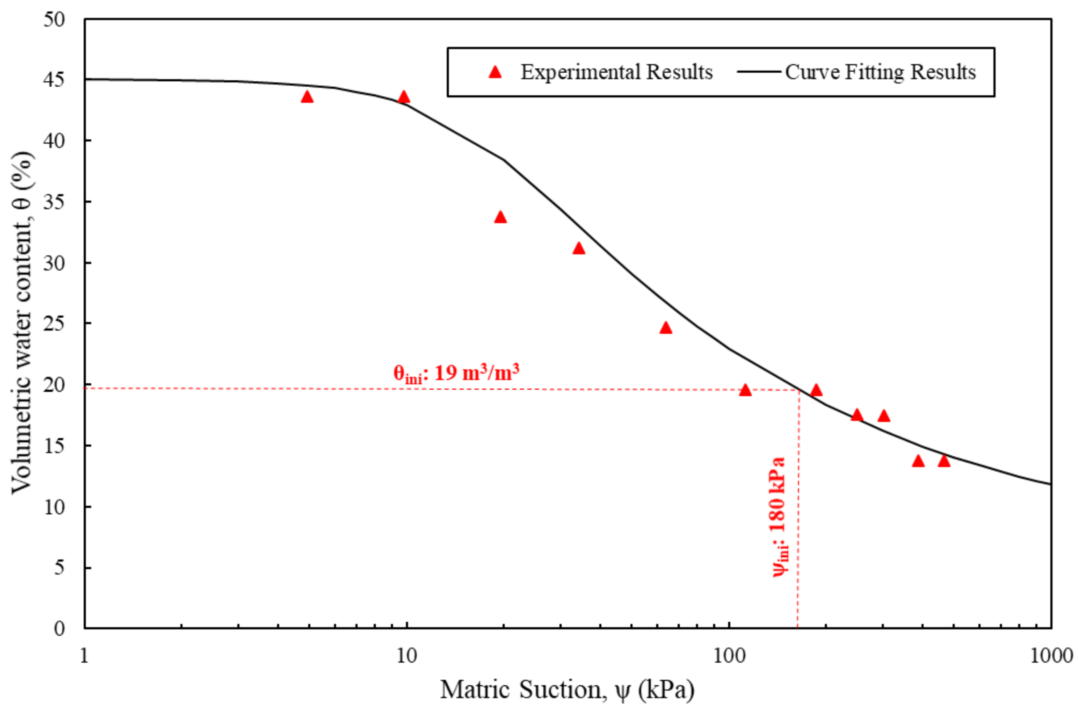

(a)

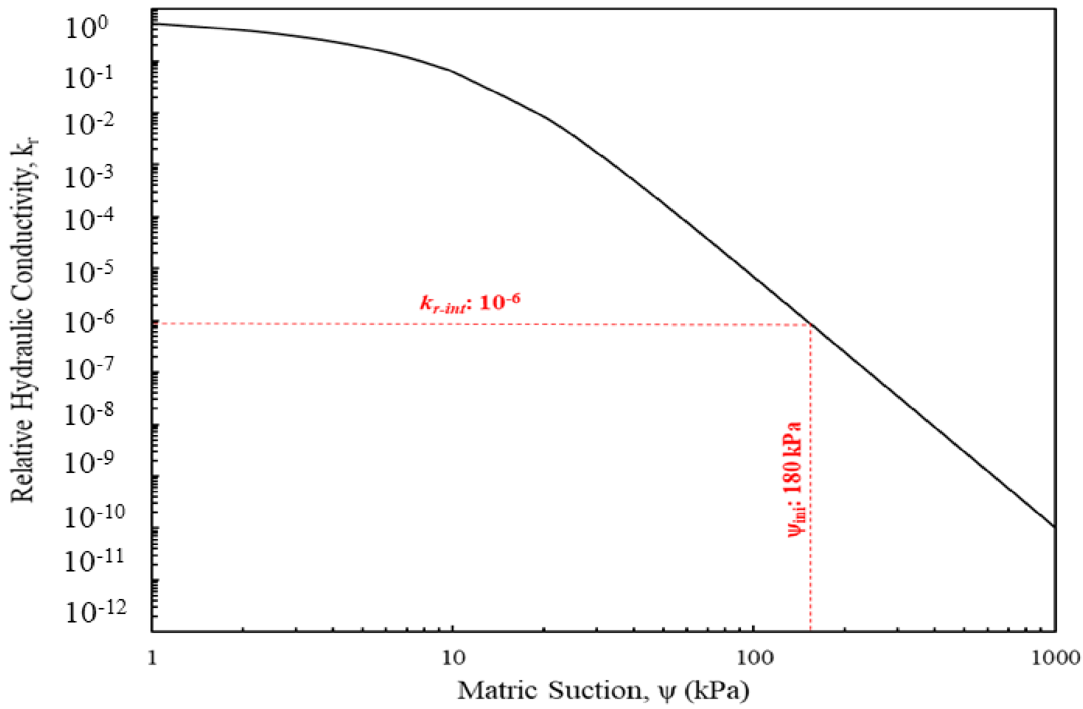

(b)

Figure 3.4: Calibration of unsaturated soil properties of sloped soil by experimental result: (a) soil water characteristics curve; and (b) *k*-function characteristics curve

doi:10.6342/NTU202301082

Maintaining a uniform state of saturation for granular soil during the pressure plate extractor test proves challenging. Therefore, the prediction of the Van Genuchten model fitting parameters for sand was conducted based on the PLAXIS enabled U.S. Department of Agriculture (USDA) recommendation, which was determined from the grain size distribution using the Van Genuchten Soil Water Characteristics Curve (SWCC) fitting method. The Soil Water Characteristics Curve (SWCC) and *k*-function characteristics curve results for the predicted encased soil are presented in Figure 3.5. The saturated volumetric and residual volumetric water content were approximately 43% and 4.5%, respectively. These values pertain to the initial dry state of the encased soil. This methodology, combining empirical data with predictive modeling, offers a pragmatic approach to analyzing granular soil behavior under variable saturation conditions, particularly when experimental uniform saturation proves challenging.

Soil classification system	USDA	
Hydraulic model	van Genuchen-Mualem	
Soil distribution	< 2μm (%)	0
	2μm～50μm (%)	0
	> 50μm (%)	100

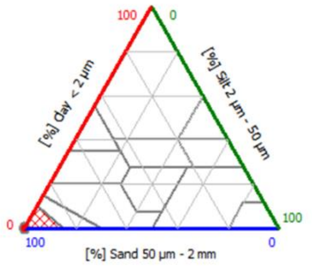

Sand

(a)

doi:10.6342/NTU202301082

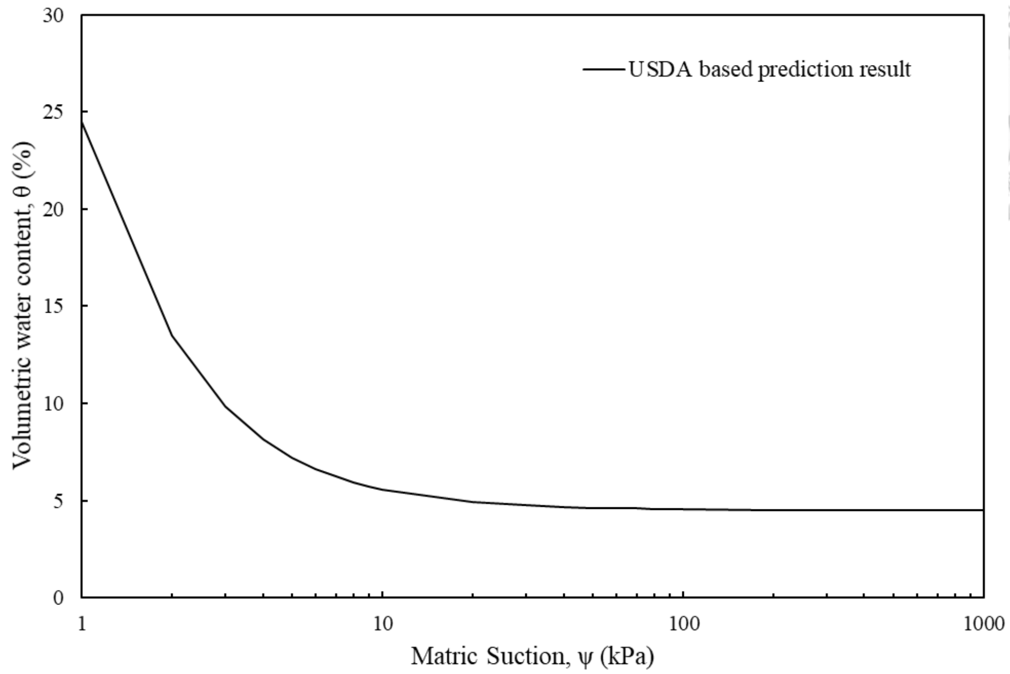

(b)

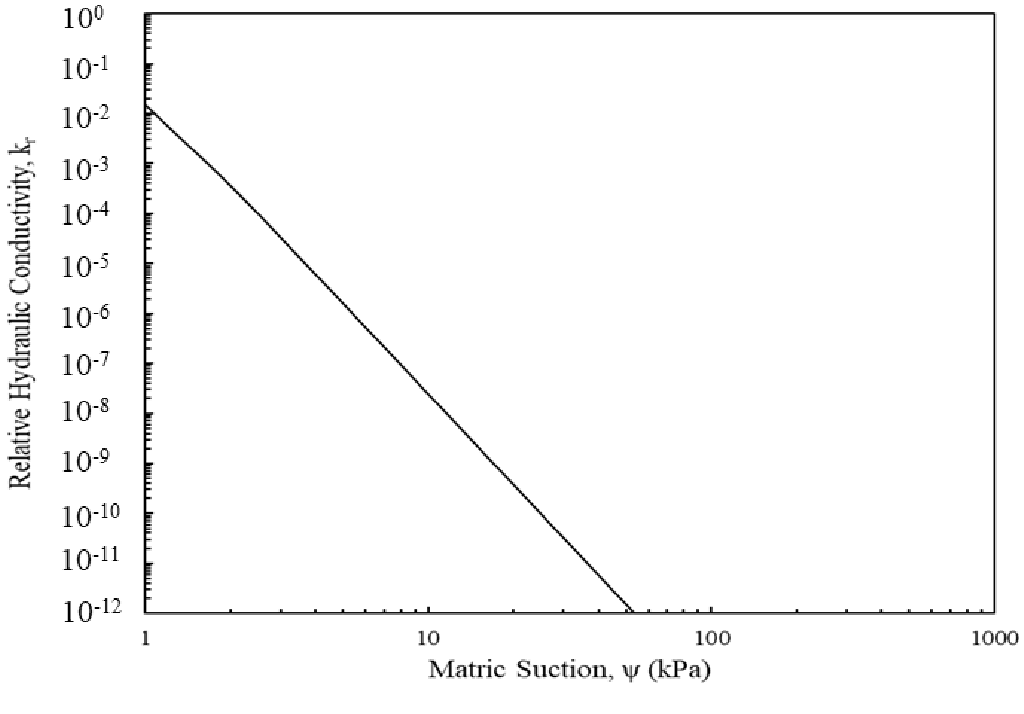

(c)

Figure 3.5: Prediction of unsaturated soil properties of encased soil: (a) inputs for prediction model; (b) soil water characteristics curve; and (c) *k*-function characteristics curve

doi:10.6342/NTU202301082

Table 3.2 presents a summary of the unsaturated state soil fitting parameters for both sloped and encased soil. These parameters have been used as inputs for the numerical simulation conducted in PLAXIS-3D, wherein the Van Genuchten Soil Water Characteristics Curve (SWCC) fitting method was employed. This utilization of the Van Genuchten SWCC fitting method helps to provide a more accurate and reliable model of the soil's unsaturated state, thereby enhancing the predictive capabilities of the numerical simulations.

Table 3.2: Input unsaturated soil properties for numerical program

Parameters	Sloped Soil (SM)	Encased Soil (SP)
θ_s, Saturated Volumetric Water Content (%)	45	43
θ_r, Residual Volumetric Water Content (%)	5.85	4.5
α, Van Genuchten Model Fitting Parameter (kPa^{-1})	0.06	1.45
n, Van Genuchten Model Fitting Parameter	2.3	2.68
m, (Mualem, 1976), $1-1/n$	0.2	0.5

3.1.2 Reinforcement properties

The reinforcement used in 1-g model test is nonwoven polypropylene geotextile, which is modeled as an elasto-plastic (N-ε) with failure strain geogrid element in FE analyses. The selected reinforcement model is superior to other available model commonly used for reinforcement because the mobilization of reinforcement tensile force (i.e. ultimate reinforcement tensile strength, T_{ult}, kN/m) and final strain (i.e. ultimate tensile strain, ε, %) can be set at a limited value. This model eliminates the complexities of manually deactivating to simulate reinforcement breakage. The input values of T_{ult} (= 0.7 kN/m) and reinforcement stiffness $J_{50\%}$ (= 5.47%) are directly calibrated from the wide-width tensile test result (Figure 3.6). Notably, low input values are used for tensile properties because the reinforcement tensile strength and stiffness properties for 1-g model test must be scaled down to $1/N^2$ of prototype tensile properties based on the

doi:10.6342/NTU202301082

similitude laws. Table 3.3 lists the values of the scaling factor ($N = 10$) and corresponding tensile properties in the prototype.

Table 3.3: Input reinforcement properties for numerical program

Properties	Scaling factor [a]	Values: Reduced scale [b]	Values: Prototype [c]
Reinforcement			
Ultimate tensile strength, T_{ult} (kN/m)	$1/N^2$	0.70	70
Stiffness, $J_{50\%}$ (kN/m)	$1/N^2$	5.47	547
Failure strain, ε_f (%)	1	12.7	12.7

[a] target scaling factor $N = 10$
[b] used in model validation

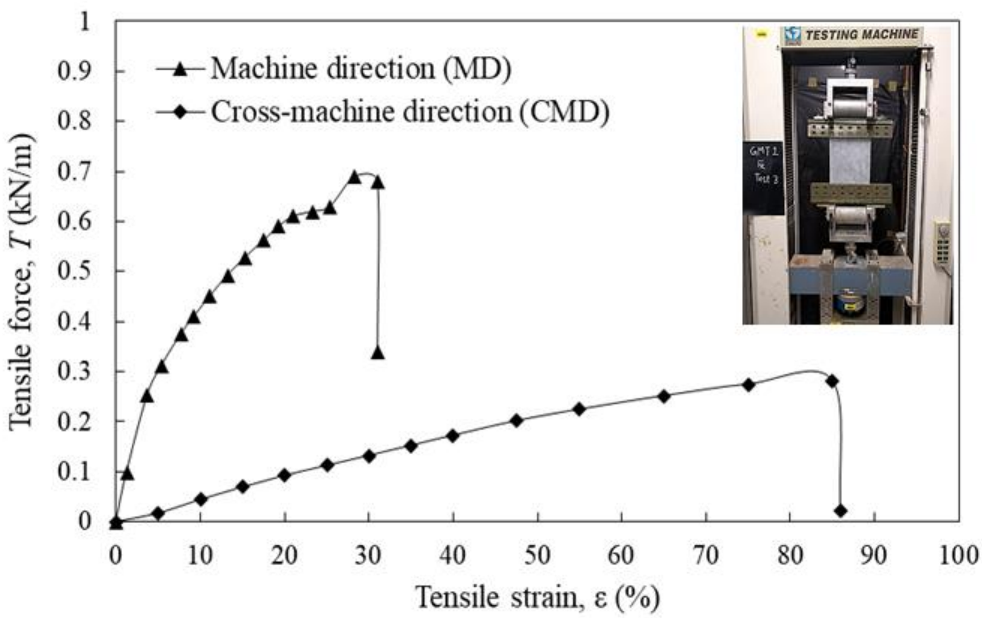

Figure 3.6: Wide width tensile test result of geotextile used in 1-*g* model test

doi:10.6342/NTU202301082

The soil-reinforcement interface is modeled as a linear elastic-perfectly plastic interface element (Table 3.1). The soil-reinforcement interface shear strength τ_{max} is defined by the Mohr-Coulomb failure criterion, expressed as

$$\tau_{\max} = R_{inter} \times \sigma_n \tan \varphi' \tag{3.3}$$

where R_{inter} is the interface reduction coefficient, σ_n is the normal stress acting on the soil-reinforcement interface, and ϕ' is the soil effective friction angle. The soil-reinforcement interface properties were determined using an apparatus modified from a conventional direct shear box. Two conditions were investigated in the test, including the starting the test and fully saturated state. For numerical simulation, interface reduction factor considered at saturated state is considered as strength propertied were reduced after soil gets saturated. The interface shear stress ratio (τ_{rel}) used for understanding the correlations or differences between the soil-soil and the soil-reinforcement is evaluated by:

$$\tau_{rel} = \frac{\tau_{mobilized}}{\tau_{\max}} \tag{3.4}$$

where $\tau_{mobilized}$ is the mobilized interface shear stress, and τ_{max} is the interface shear strength as defined in Eqn. 3.4.

Figure 3.7 illustrates the experimental set-up used to measure the permittivity of the geotextile. This was achieved by modifying the constant head permeability test set-up. The measured values reflect a decrease in the permeability of the encased soil when exposed to extreme seepage conditions. A layer of geotextile is positioned between the layers of encased soil. A decrease in permeability suggests a reduction in both horizontal and vertical drainage capacity. The permeability value for the geotextile-encased soil, denoted as $k_{geotextile\text{-}encasedsoil}$, was found to decrease to 7.849×10^{-4} m/sec. This measured decrease underlines the influence of geotextile on soil permeability and the potential implications for water flow and soil stability under seepage conditions.

doi:10.6342/NTU202301082

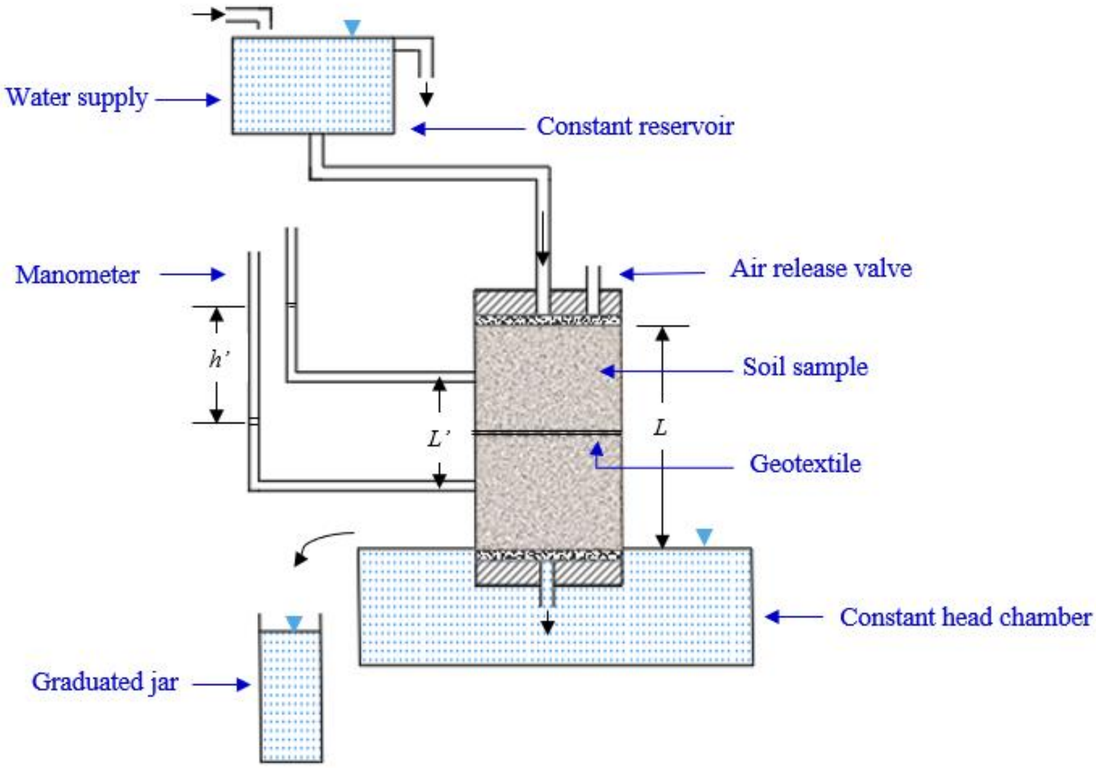

Figure 3.7: Modified constant head permeability test set-up for permittivity of geotextile

3.2 Boundary conditions

Figure 3.8 depicts the slope geometry, fixities, and composition of the natural slope considered for the numerical simulation. The slope angle for the sloped soil is set at 50°, while the impermeable rock is inclined at a 5° angle. This configuration results in a total slope height and length of 6.0-m and 8.0-m, respectively. Extreme seepage conditions, representing 80% of the total height of the slope, have been initiated from the crest side of the slope (i.e., the right side) and proceed towards the toe side of the slope (i.e., the left side). These parameters provide a comprehensive basis for the numerical simulation, allowing for a detailed examination of slope stability under extreme seepage conditions.

doi:10.6342/NTU202301082

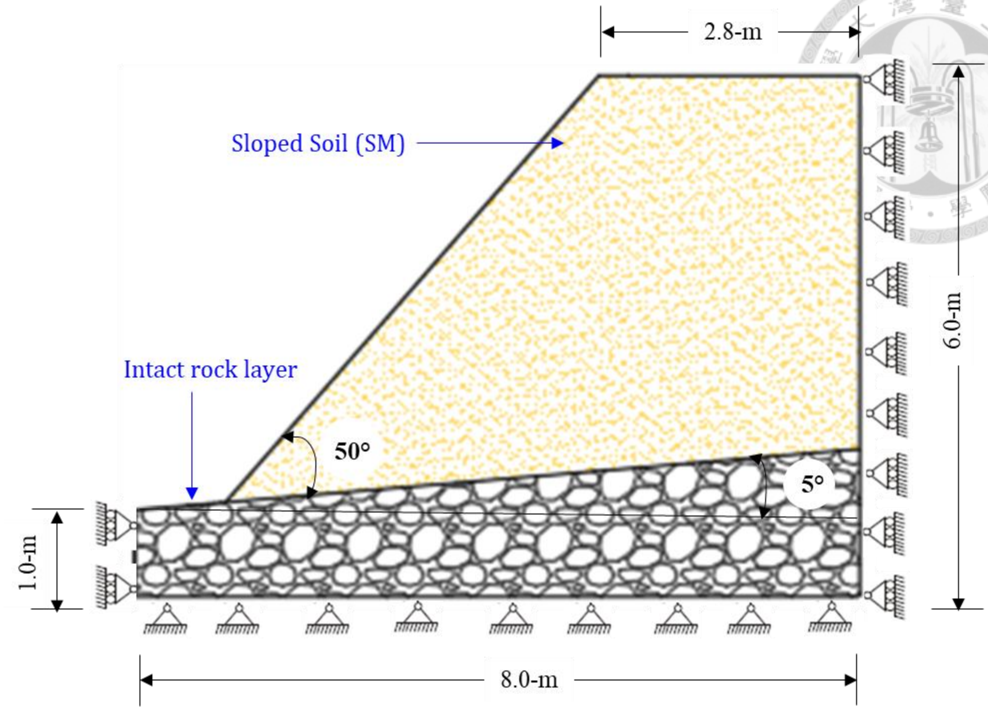

Figure 3.8: Slope geometry, fixities and constitution of natural slope

A mesh size encompassing 15 nodal elements has been chosen, as it provides more accurate results in comparison to elements with 6 nodes. It should be noted that the mesh size influences slope stability, with stability increasing alongside the refinement of the mesh size in finite element analysis. However, this also leads to increased computational time and memory usage. For the analysis, a medium mesh size of 0.5-m with a global scale factor of 1.0 has been adopted. The swept meshing option has been selected to enable faster mesh generation and provide greater control over mesh density. The mesh for sloped soil and encased soil has been refined by a factor of 0.5, while the mesh for the geotextile has been refined by a factor of 0.25. These adjustments serve to enhance the accuracy of failure surface calculations, thereby contributing to the robustness and reliability of the finite element analysis results.

Figure 3.9 illustrates the mechanical boundary conditions of the three-dimensional model. In the initial phase, standard fixities are applied to the model boundaries. The

doi:10.6342/NTU202301082

lateral boundaries in the x-direction and y-direction are allowed to move only in the vertical direction (i.e., $u_x = 0$, $u_y \neq 0$, $u_z = 0$). The bottom boundary, on the other hand, is restrained from movement (i.e., $u_x = 0$, $u_y = 0$, $u_z = 0$), while the top boundary remains free for movement (i.e., $u_x \neq 0$, $u_y \neq 0$, $u_z \neq 0$). The initial stress state is generated by applying the gravity loading procedure during the initial phase. Here, the vertical stress is in equilibrium with the soil's self-weight, while the horizontal stress is computed from the gravity loading condition to generate K_0 value. The application of the gravity loading procedure is justified due to the inclined sloped soil layer being confined by the sandbox. Following the generation of the initial stress state, the displacement is reset to zero at the start of subsequent calculation phases. This meticulous application and adjustment of boundary conditions ensures a robust and accurate numerical model, providing a solid basis for the analysis of slope stability under varying conditions.

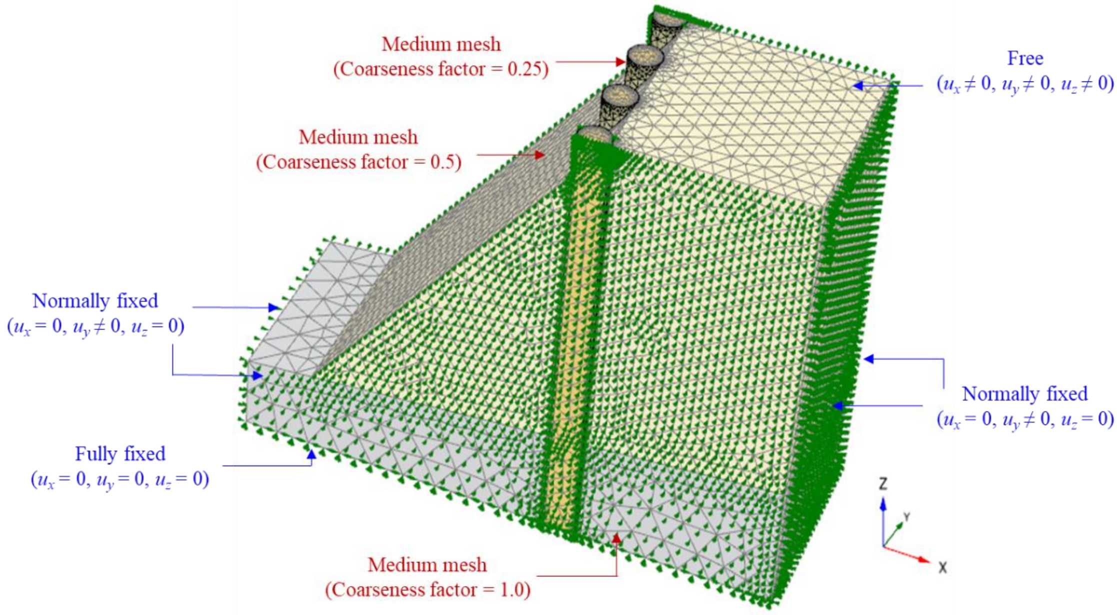

Figure 3.9: Mechanical fixities and mesh fineness for GEC stabilized slope

Figure 3.10 represents the hydraulic boundary conditions of the three-dimensional model. The model is set up to facilitate the inflow of seepage in the x_{max} direction and the

doi:10.6342/NTU202301082

outflow of seepage in the x_{min} direction. Accordingly, the hydraulic boundary in the aforementioned direction is kept open to groundwater flow, whereas the remainder of the hydraulic boundaries are deemed closed. This configuration allows for the controlled modelling of seepage flow, contributing to a more accurate representation of real-world hydrological conditions within the numerical model.

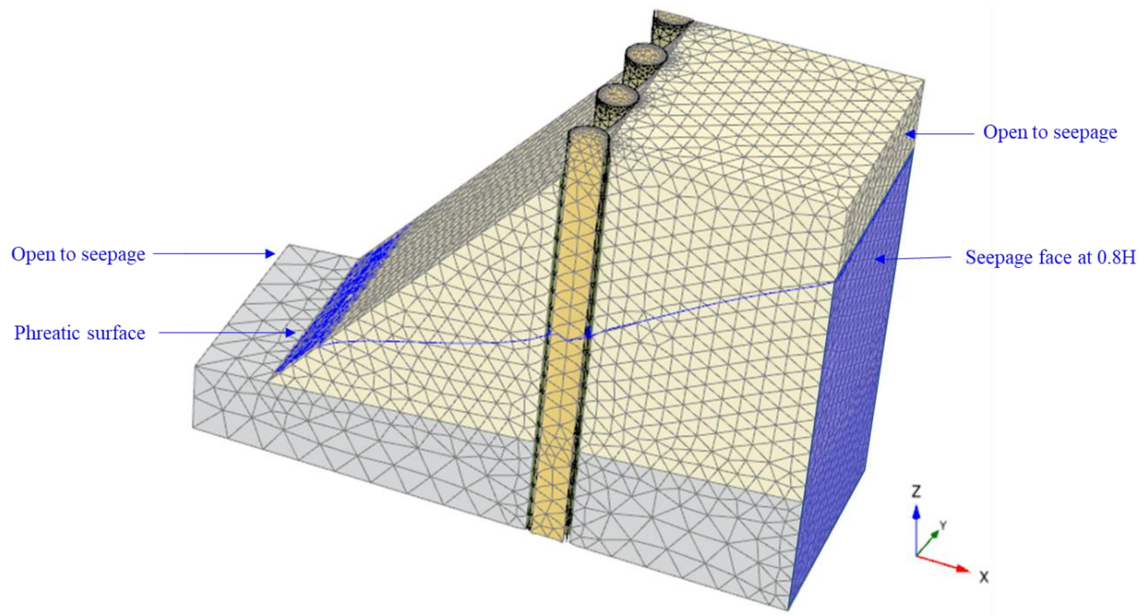

Figure 3.10: Hydraulic fixities and generated phreatic surface

3.3 Computational sequences

This section delves into the details regarding the construction sequences employed for the analyses in this study. Numerical computations were performed using PLAXIS-3D. The sequences were programmed to emulate the practical installation of GEC using the replacement method, as referenced in Huesker (2021). The replacement method is a low-impact installation method deemed suitable for maintaining slope stability during the installation of reinforcing agents such as GEC. This approach helps ensure the slope's integrity and safety while facilitating the incorporation of reinforcing elements. Here follows the step-by-step procedure:

doi:10.6342/NTU202301082

(a) Initial phase: The initial groundwater table is established at an elevation of 1.0-m from the ground surface at rock surface. The pore water calculation relies on the phreatic water level condition, with calculations performed based on gravity loading. It's important to note that, given the transient nature of the seepage analysis, suction has been taken into consideration, while other numerical control parameters have been set to their default settings. This method provides a realistic simulation of groundwater behavior under the specified conditions, providing valuable insights for further analysis.

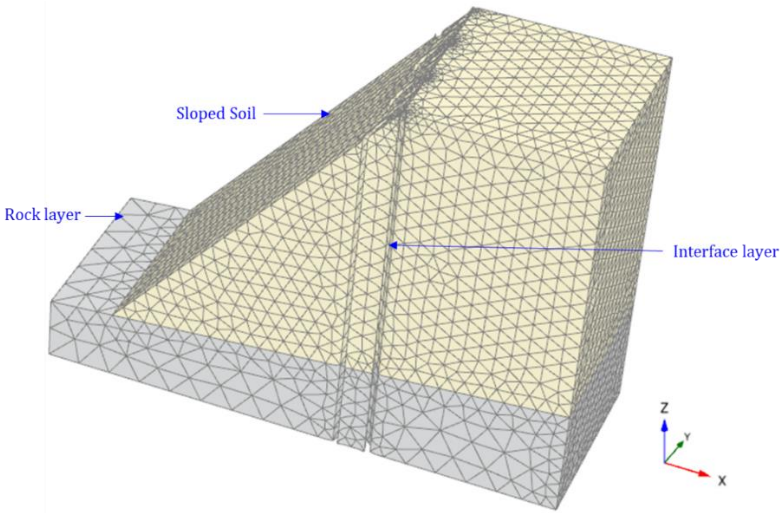

Figure 3.11: 3D numerical model at initial phase

(b) Installation of steel-casing and geotextile: To emulate the impact of steel casing, a series of cylindrical rigid bodies was generated and activated. These bodies restrict the movement of soil volume around the GEC installation area. Both negative and positive interfaces, with a virtual thickness factor of 0.1, and with hydraulic flow activity for geotextile, were maintained active throughout the simulation stages. Similar to earlier steps, other numerical control parameters were set to their default settings. This procedure ensures a realistic representation of steel casing effect during the installation of GEC, and contributes to a more

doi:10.6342/NTU202301082

accurate assessment of its performance within the soil matrix.

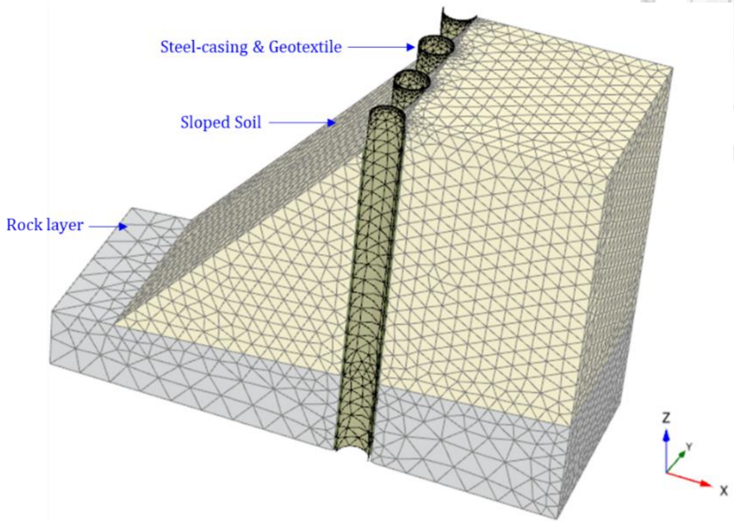

Figure 3.12: 3D numerical model at installation of steel-casing and geotextile

(c) Filling of granular soil: A cylindrical soil volume, incorporating the properties of encased soil, was activated. This step enables the simulation to represent accurately the physical and mechanical behaviors of the encased soil within the GEC in the context of the larger soil matrix, thus contributing to the validity and robustness of the analysis.

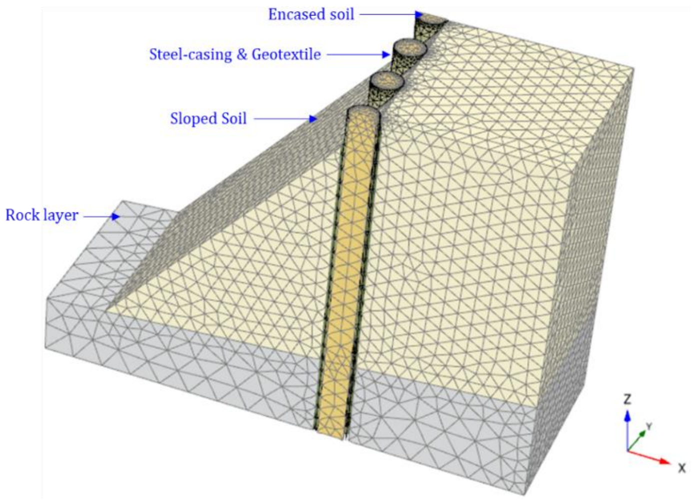

Figure 3.13: 3D numerical model at the stage of filling of granular soil

doi:10.6342/NTU202301082

(d) Removal of steel casing: The series of cylindrical rigid bodies was deactivated concurrently with the introduction of geotextile. This step enables the generation of stress within the geotextile, simulating the effect of steel casing removal. Thus, the procedure accurately portrays the conditions following casing withdrawal and allows for realistic representation of the associated stress dynamics within the geotextile reinforcement.

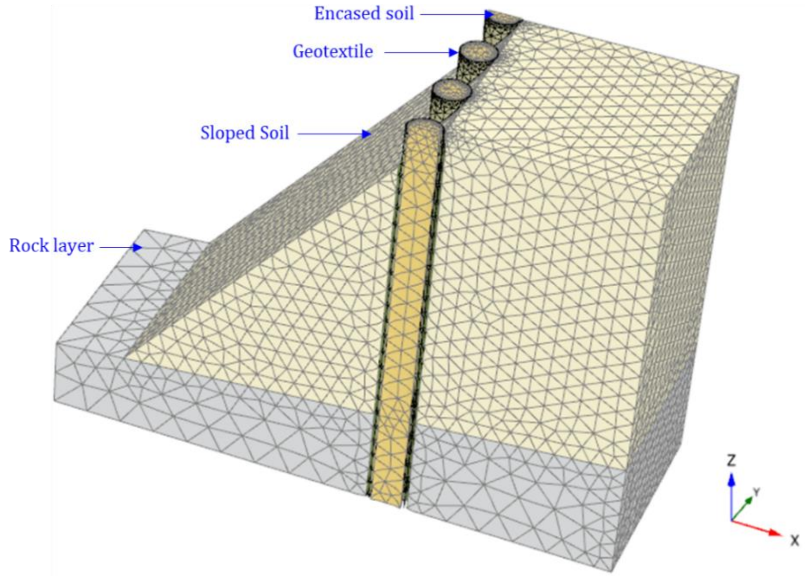

Figure 3.14: 3D numerical model at the stage of removal of steel casing

(e) Transient seepage analysis till failure of slope: In this stage, the calculation type is set to fully coupled flow deformation and is intended to simulate a total duration of 50 hours. The maximum number of calculation steps has been increased to 2000, while the rest of the numerical control parameters adhere to the default values set by PLAXIS-3D. It is important to note that the updated mesh function does not operate in this stage. Consequently, the simulation ceases to proceed further once the deformed mesh is large enough to cause convergence issues for the FE-based simulation. Factors such as incremental deviatoric strain ($\Delta\gamma_s$) and plastic points contribute to understanding the failure mechanism. These

doi:10.6342/NTU202301082

elements will be discussed in greater detail in the subsequent chapters.

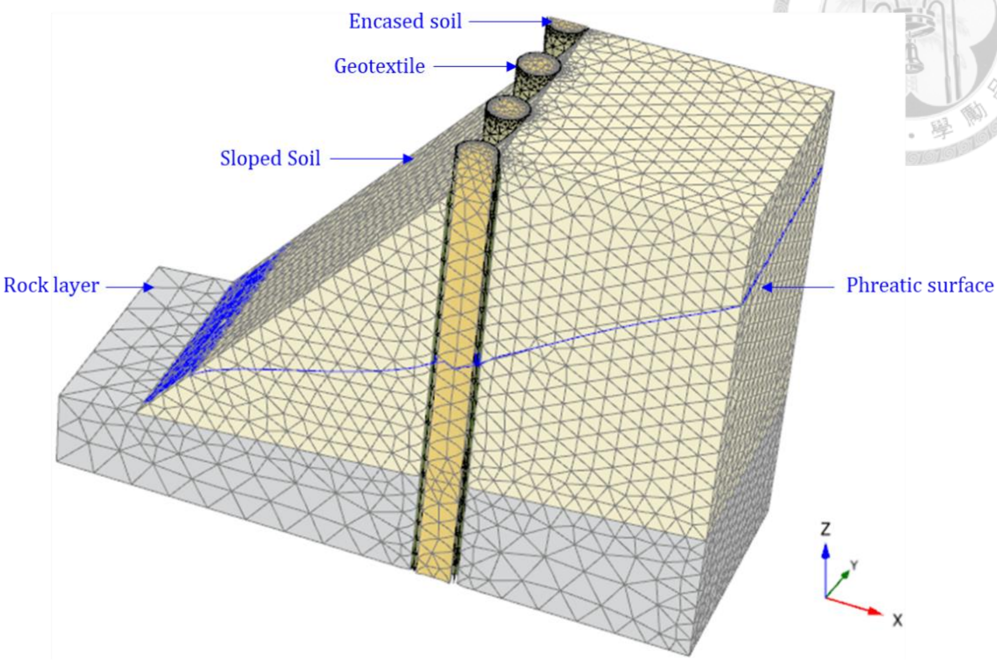

Figure 3.15: Stage of transient seepage analysis till failure of slope

The construction sequence for a rigid pile-stabilized slope follows a similar procedure to that of the GEC-stabilized slope, with one notable exception. Instead of filling with granular soil (as in Step c), precast concrete piles are installed. This alteration in the procedure accurately replicates the conditions associated with the installation of rigid pile reinforcements in slope stabilization projects, thus ensuring a valid representation within the numerical simulations.

3.4 Model validation

Before proceeding with the numerical analyses for the GEC-stabilized slope, it is imperative to conduct and validate experimental tests on the properties of GEC under bending conditions. It's worth noting that many finite element simulations for rigid piles employ a linear elastic model. However, in an effort to maintain the uniformity of the stress-dependent soil model among the various stabilizing agents used in this study, such

doi:10.6342/NTU202301082

as encased soil and rigid pile, the Mohr-Coulomb model has been utilized for the rigid pile. Accordingly, this section will discuss the calibrated properties of both the linear-elastic and the Mohr-Coulomb model for rigid pile.

3.4.1 Flexural rigidity test of GEC

The flexural rigidity test is a common procedure performed on structural components like beams or steel sections to determine their bending rigidity both pre and post plastic stage. In this study, since the GEC is not subject to direct external loading but rather to failure caused by rapid seepage, it's assumed that failure in GEC under bending conditions occurs purely at the elastic stage. However, given that the encased soil adheres to the elasto-plastic model of the Hardening soil model, and the geotextile follows the elastic model before rupture failure, it's challenging to define a singular model for a conjoined GEC where the properties of soil and geotextile are treated independently.

The flexural rigidity test of GEC is a novel approach introduced in this study to confirm the *EI* value in units per length. Previous research (Vogt et al., 2014) has conducted experimental work to determine the bending stiffness of GEC. Their findings suggest that geotextile stiffness, the fill material, and the fill material's density are dominant factors influencing bending and buckling. No rupture of the geotextile was observed upon reaching the buckling load.

PLAXIS-3D, an FEM-based software, is capable of simulating the soil encased inside the geotextile in a cylindrical shape. Thus, a simply supported GEC beam was simulated under different loading conditions (1-time, 2-times, and 3-times of unit weight of soil) and varying lengths of the supported beam with a constant diameter of 0.5-m. This comprehensive approach also captures the system's non-linearity, hence large-scale deformation of structural elements is ignored. The numerical simulation was carried out

doi:10.6342/NTU202301082

both in prototype and reduced scale model, and results were validated against experimental test results conducted on the reduced scale model (Figure 3.16).

In the experimental *EI* test approach for GEC, both supports ends of the sample were hinged and elevated, allowing for deformation by bending. The experimental geotextile sleeve was sewn to form a full cylindrical shape, and the soil sample was compacted in five different segments to maintain uniform density. A black and white strip was placed to measure the deformation of the sample's centerline, with each segment measuring 1-cm in length. It was observed during test repetitions that the direction of the sewn sleeve had minimal impact on the results.

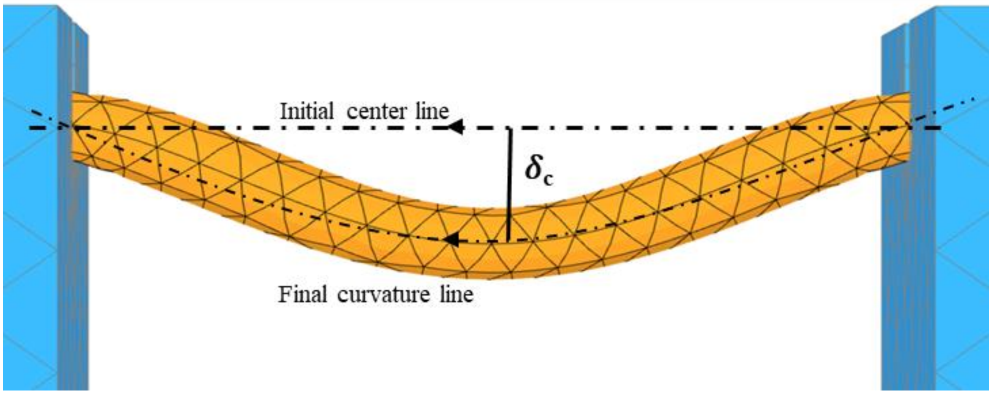

(a)

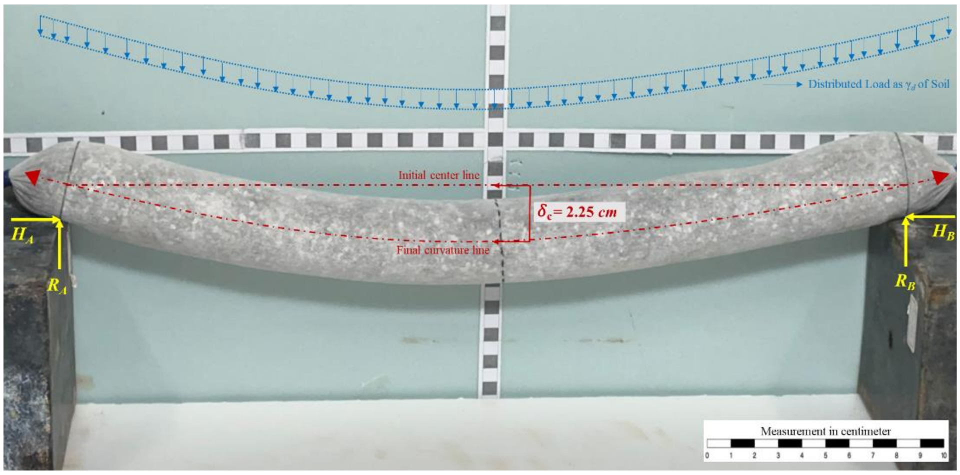

(b)

Figure 3.16: Flexural rigidity test of GEC: (a) Approach by numerical simulation; and (b) Experimental test result

doi:10.6342/NTU202301082

Figure 3.17 illustrates the validation of the flexural rigidity (*EI*) test of the geosynthetic encased column (GEC) conducted using both experimental and numerical approaches. The experimental results obtained from the reduced-scale model have been scaled up according to the similarity law, with a scale factor of N=10. There is a significant correlation between the measured values from the experiment and the values predicted by the numerical simulation, demonstrating the validity of the simulation model. This correlation is essential as it verifies that the numerical model accurately represents the physical behavior of the GEC under test conditions.

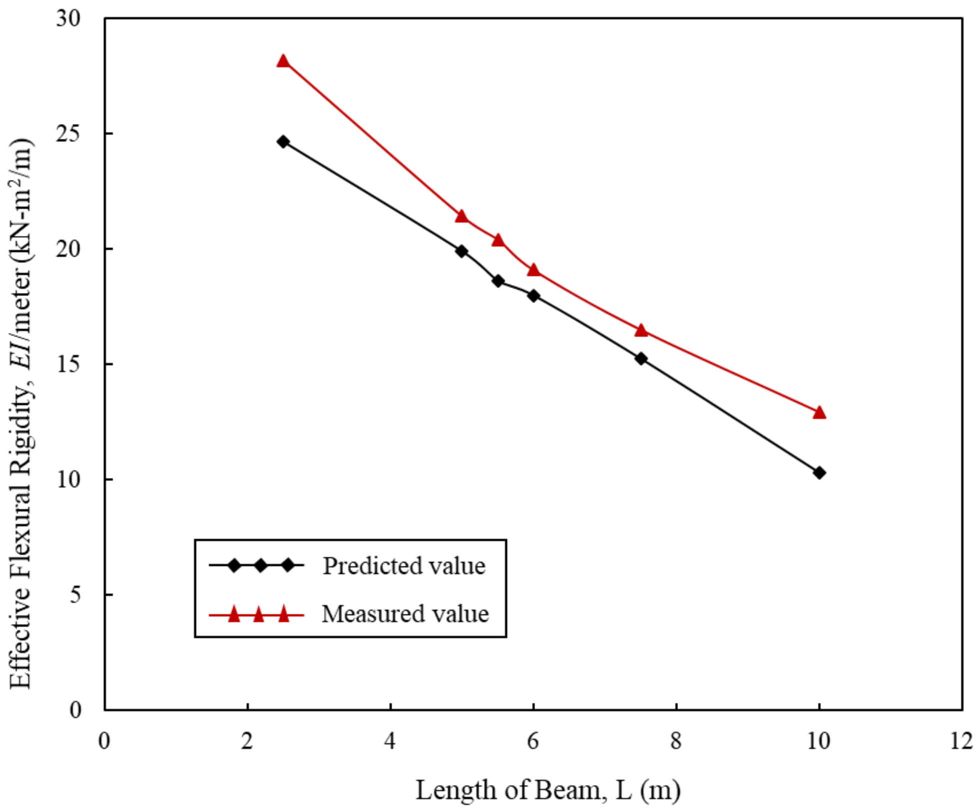

Figure 3.17: Validation results of the flexural rigidity (*EI*) test of GEC

Indeed, when it comes to composite materials like geosynthetic encased columns (GECs), their flexural rigidity is often determined using analytical approaches that consider the individual contributions of each component (in this case, the encased soil and the geotextile encasement). In this context, the theory of superposition is particularly

doi:10.6342/NTU202301082

useful for understanding the composite behavior of these components. This theory allows for the individual responses of each component to be added together to obtain the overall response of the composite material.

As the components are subjected to bending (or a combination of bending and axial loading), it becomes crucial to define the strength, stiffness, and ductility properties of the cross section based on the Moment-Curvature relationship. This relationship as depicted in Figure 3.18 is the basis of bending deformation theory, and it can provide important insights into how the composite material will perform under various load conditions.

The Moment-Curvature relationship shows how the bending moment (the product of a force and the distance from the point of application of the force to the point where bending occurs) changes with the curvature of the material (defined as the reciprocal of the radius of curvature). By understanding this relationship, we can better predict and manage the performance of GECs and similar composite materials in a variety of applications.

Curvature is a geometrical parameter representing cross sectional deformation is defined as unit rotation angle of a cross section under bending effect. It is obtainable the derivative of the inclination of the tangent with respect to arc length. In this approach, neutral axis ($\sigma = 0$) is located at the centroid of the beam cross section and bending stress varies linearly over beam cross section and is maximum at the extreme fibers of the beam.

$$curvature(k) = \frac{d\theta}{dy} = \frac{d^2y}{dx^2} = \frac{1}{\rho} \tag{3.5}$$

$$k = \frac{M}{EI} \tag{3.6}$$

Where, M = moment, EI = flexural stiffness

doi:10.6342/NTU202301082

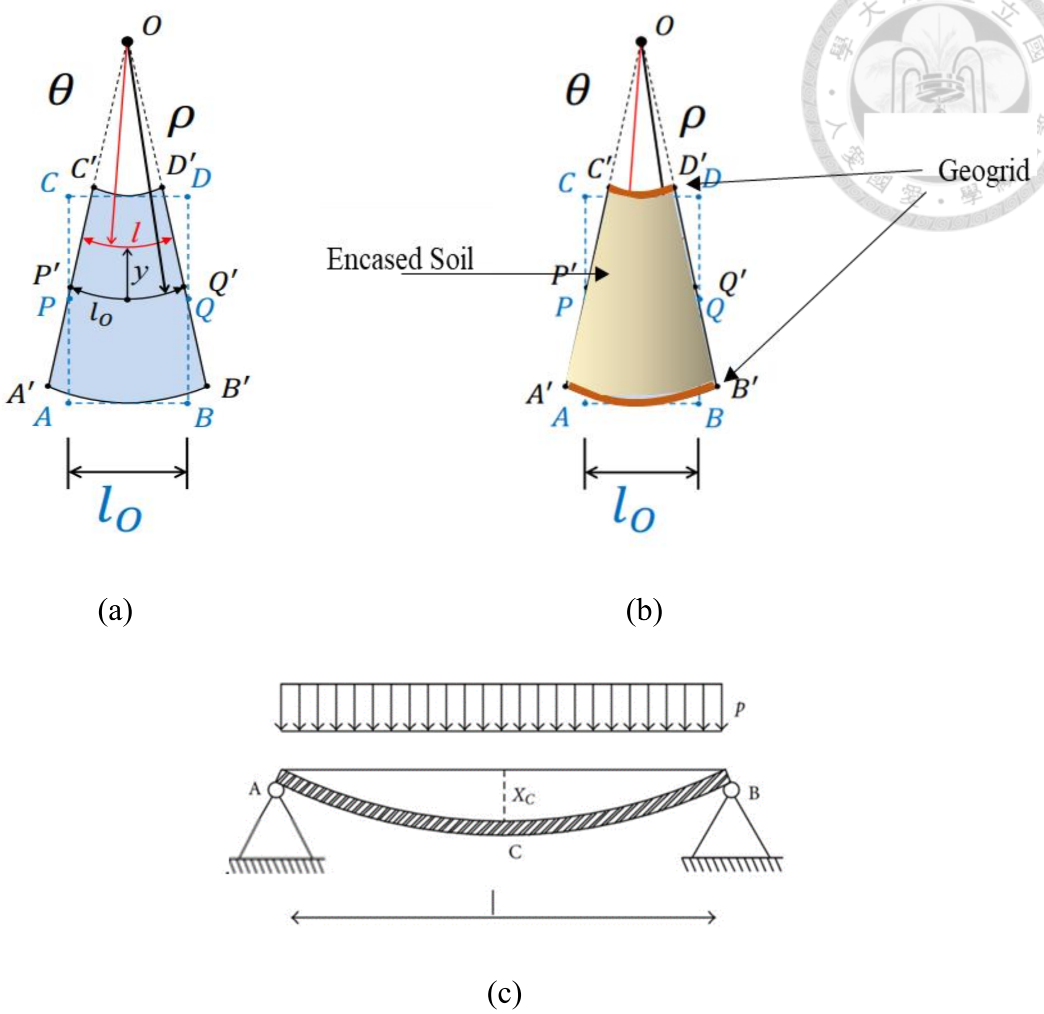

Figure 3.18: Bending of beam subjected to lateral load: (a) Bending deformation of beam; (b) Bending deformation of composite GEC; and (c) Bending of simply supported beam case

External moment would be carried by the both geogrid layer and encased soil materials.

$$M_{total} = M_s + M_g \tag{3.7}$$

$$k(EI)_{composite} = k_s(EI)_s + k_g(EI)_g \tag{3.8}$$

As neutral axis is same for both the materials, value of curvature *k*(rad/meter) would be same.

$$k = k_s = k_g \tag{3.9}$$

doi:10.6342/NTU202301082

So that,

$$(EI)_{composite} = (EI)_s + (EI)_g \tag{3.10}$$

Based on result of deflection (Eqn. 3.11), flexural rigidity (Eqn. 3.12) could be calculated.

$$Deflection(\Delta_C) = \frac{5wl^4}{384EI} \tag{3.11}$$

$$(EI)_{FEM} / meter = \frac{5wl^3}{384\Delta_C} \tag{3.12}$$

Figure 3.19 shows the validation flowchart of *EI* test of GEC based on three approaches, i.e., reduced scale experiment, prototype numerical simulation, and analytical solution. Hence, all the mentioned approaches provide the conformity to the results. It is noteworthy that *EI* value of rigid pile is approximately 500 times of *EI* value of GEC which makes the GEC stabilized slope as flexible slope systems.

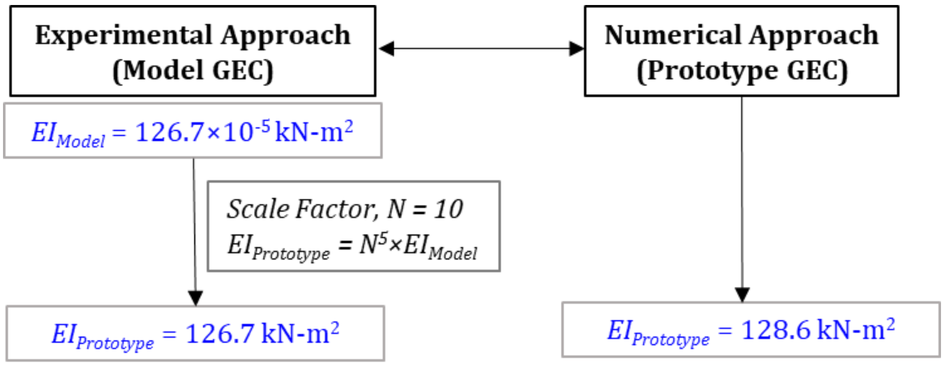

Figure 3.19: Validation flowchart of the flexural rigidity (*EI*) test of GEC

doi:10.6342/NTU202301082

3.4.2 Laterally loaded rigid pile model

In the study discussed by Li et al. (2022), rigid piles made of reinforced cement concrete (RCC) are modeled as linear elastic models when loaded laterally. However, in this study, the Mohr-Coulomb's properties for rigid piles have been calibrated (as summarized in the referenced Table 3.4). The failure of the rigid pile under conditions of active earth pressure is simulated by applying lateral loading, with earth pressure quantified based on the soil properties (Figure 3.19). It is important to note that both the soil and the rigid pile share the same dry material type, an initial porosity (n) of 0.1, and a unit weight (γ_s) of 24 kN/m^3.

A comprehensive understanding of the behaviour of these piles under various load conditions is facilitated by this approach of using Mohr-Coulomb parameters for the rigid piles in combination with the soil properties. The use of the Mohr-Coulomb soil model in modeling the behavior of rigid piles offers a more realistic depiction of their performance under lateral loading. This model is widely employed in the field of geotechnical engineering to estimate the strength of soils due to its simplicity and ease of use, despite its limitations in fully capturing the complex behavior of soils under different conditions. To compare the results and better evaluate the reliability of these predictions, additional analyses using different soil models may need to be carried out.

Table 3.4: Calibration properties for rigid pile model

Properties	**Rigid pile properties**	
	Linear elastic model (Li et al., 2022)	**Mohr-Coulomb model (this study)**
Stiffness, E' (kN/m^2)	3x10^7	3x10^7
Poisson's ratio, ν'	0.2	0.2
Effective cohesion, c' (kN/m^2)	-	3500
Effective frictional angle, ϕ' (°)	-	45
Effective dilatancy angle, ψ (°)	-	0
Tensile strength, T (kPa)	-	0

doi:10.6342/NTU202301082

The final model calibration results have been evaluated by comparing the horizontal deflection and the resisting bending moment within the elastic zone (Figure 3.21). For the simplicity of all model conditions and comparison of failure timing, soil element model for rigid pile have been considered. An embedded beam with infinitesimal diameter and modulus of elasticity has been introduced within the rigid pile. In the final analysis step, the bending moment value is multiplied by a factor of increment to achieve the accurate value. This methodology was examined and validated by Dao (2011), and the comparison showed a considerable match in the properties. The process of inserting an infinitesimal beam and subsequently adjusting the bending moment value provides a method of circumventing the limitations of the Mohr-Coulomb model for structural analysis. This innovative approach allows for more accurate estimation of the bending moment in rigid piles.

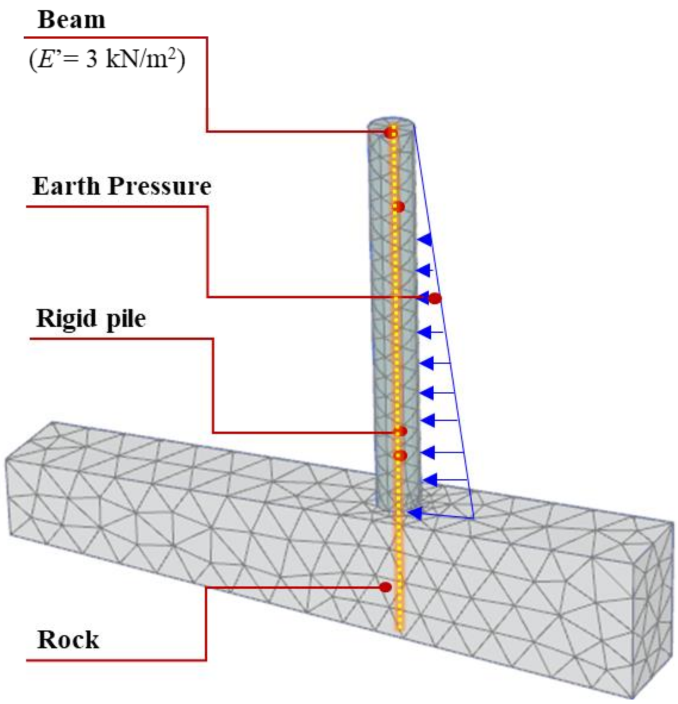

Figure 3.20: Numerical model for calibration of rigid pile properties

doi:10.6342/NTU202301082

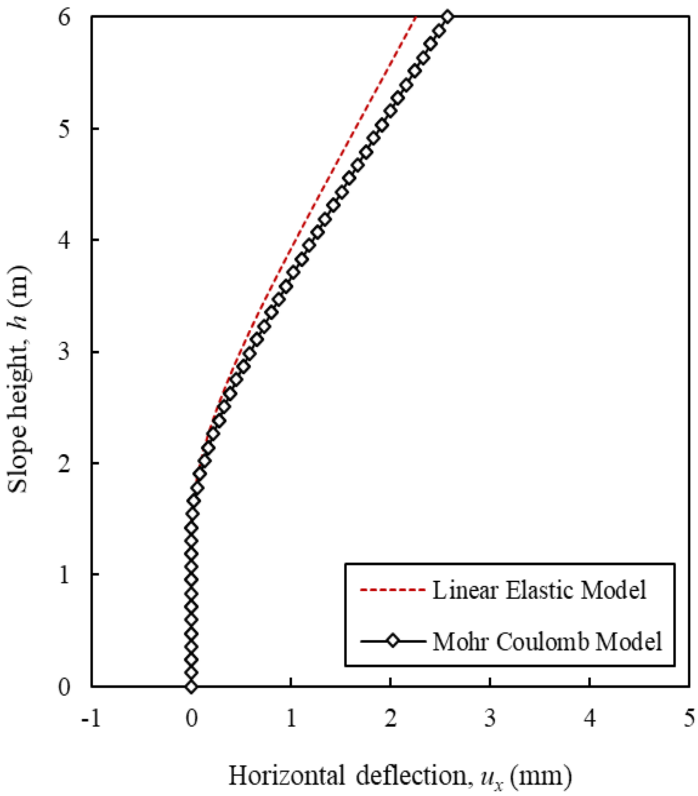

Figure 3.21: Calibration results at the centerline of rigid pile model based on horizontal deflection

3.5 Rise of groundwater level

An increase in groundwater level directly influences seepage conditions and consequently, slope stability. Various factors can lead to a rise in groundwater level, such as extreme flooding, rising sea levels, or elevated water levels in dam or river embankments. Correlating the relationship amongst these different factors influencing the rise in groundwater level can be extremely challenging.

Figure 3.22 illustrates common failure modes in dam embankments due to extreme seepage conditions, where failures due to seepage and piping can erode sloped soil. Such instances could be mitigated with the installation of stabilizing agents that are capable of effectively dissipating pore water pressure. These stabilizing agents can provide a critical line of defense against groundwater-induced instabilities and erosion, safeguarding the structural integrity of dam embankments and other similar structures.

doi:10.6342/NTU202301082

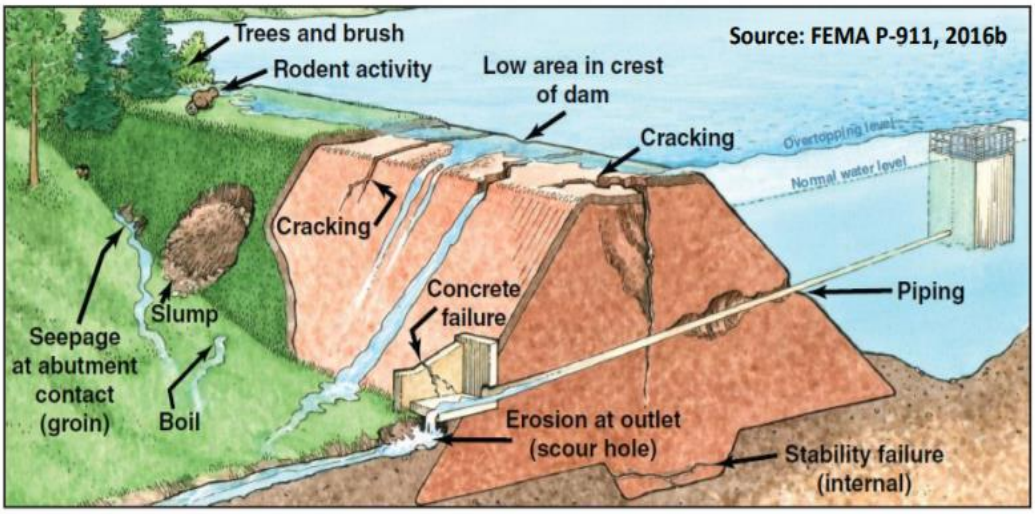

Figure 3.22: Failure of embankment by seepage and piping (FEMA, 2016b)

Figure 3.23 presents the timeline of the groundwater level rise. The initial water level is set at a ground level of 1-meter and is increased in five stages to an extreme water level of 5 meters. The water level is incrementally raised with a pause of 100 minutes at each stage. These increments are calculated based on a normalized water level (h_w/H), where h_w denotes the height of the water level and H signifies the total height of the slope. The stages are set at normalized water levels of 0.33, 0.45, 0.58, 0.70, and 0.83, respectively. The final stage of h_w/H = 0.83 is maintained for 50 hours, a duration deemed sufficiently long for a slope failure to occur under seepage conditions.

doi:10.6342/NTU202301082

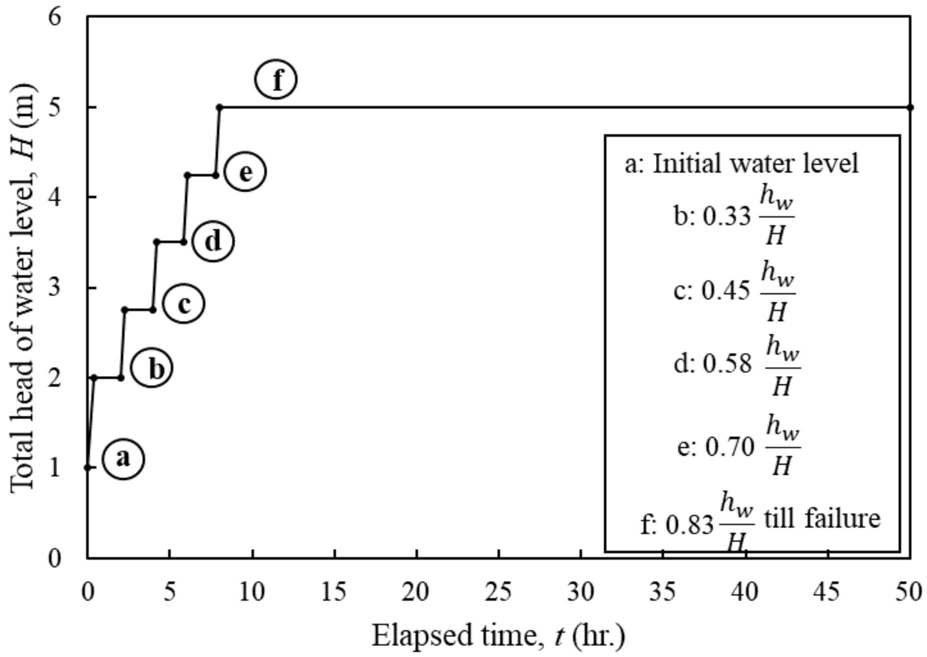

Figure 3.23: Pattern of groundwater level rise

doi:10.6342/NTU202301082

Chapter 4 Model Validation

This chapter discusses the geometry of 1-*g* experimental model which is used to validate the numerical results. The 1g model tests on natural slope, and GEC stabilized slope were conducted using a sandbox in the geotechnical research laboratory at National Taiwan University. Figure 4.1 presents a geometry of the reduced-scale model test.

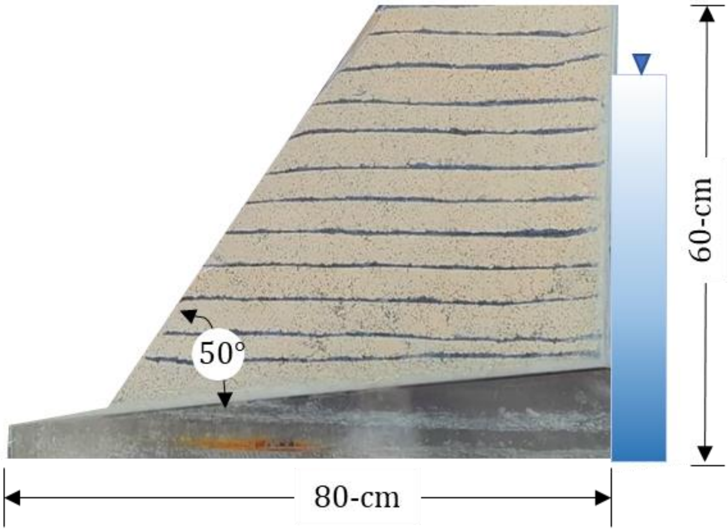

(a)

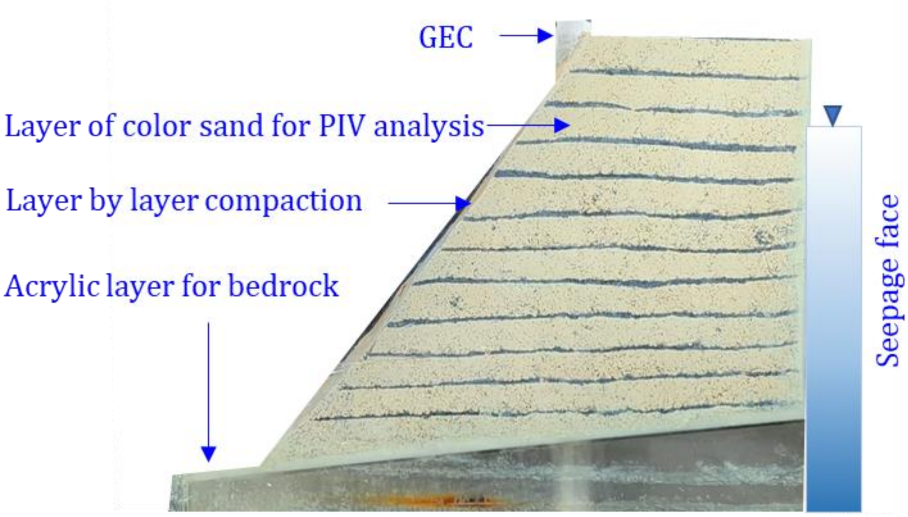

(b)

Figure 4.1: Geometry of experimental model of (a) natural slope; and (b) GEC stabilized slope

doi:10.6342/NTU202301082

4.1 Experimental validation for natural slope

The results of numerical and experimental models were validated based on three conditions: (1) failure surface, (2) deformed surface profile, and (3) progression of the phreatic surface.

Figure 4.2 presents the experimental and numerical results of the final failure surface for the natural slope subjected to seepage conditions. The failure surface for reduced scale model tests could be identified by observing the movement in the layers of colored sand. Additionally, sophisticated Particle Image Velocimetry (PIV) analysis was employed to understand the development of shear strain (ε_{xy}). It is important to note that the Finite Element (*FE*) analysis neither considers strain softening behavior nor allows for large deformation at the post-failure behavior of the slope. The obtained results display a close approximation in predicting the final failure surface of the natural slope.

doi:10.6342/NTU202301082

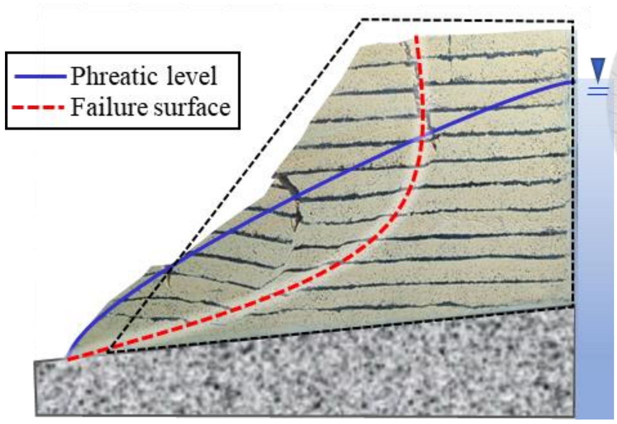

(a)

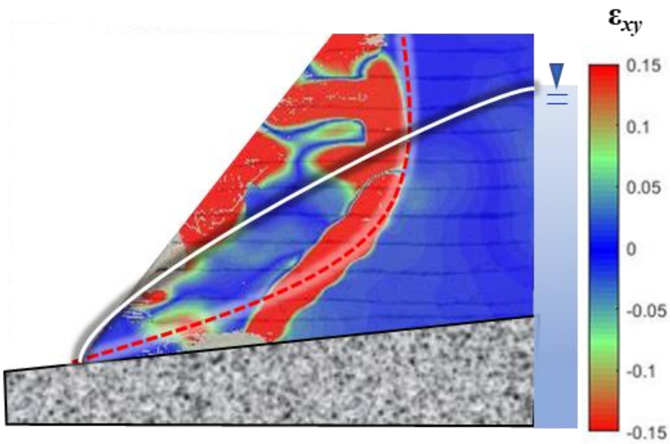

(b)

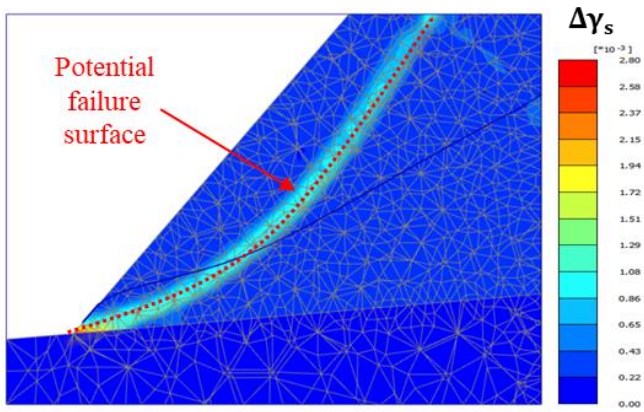

(c)

Figure 4.2: Validation by failure surface of natural slope; (a) observed failure surface of test model; (b) failure surface of test model by PIV analysis; and (c) failure surface by incremental deviatoric strain ($\Delta\gamma_s$) of numerical model

doi:10.6342/NTU202301082

Figure 4.3 depicts a comparison of the predicted and measured surface settlement profiles of the natural slope subjected to seepage conditions. The predicted and measured results are generally in good agreement, although the surface settlement is underestimated in Finite Element (*FE*) analyses. Garcia and Bray (2019a) reported a more localized settlement in the experiment than the predicted settlement in numerical analyses because the numerical mesh is inevitably larger than the real soil particle size. This results in a thicker shear band and a less localized settlement being obtained in numerical analyses than in the experiment. The numerical results are influenced by mesh size; thicker shear bands were observed when a medium-element mesh was used in the FE analysis, while relatively narrow shear bands were obtained when a fine-element mesh was adopted.

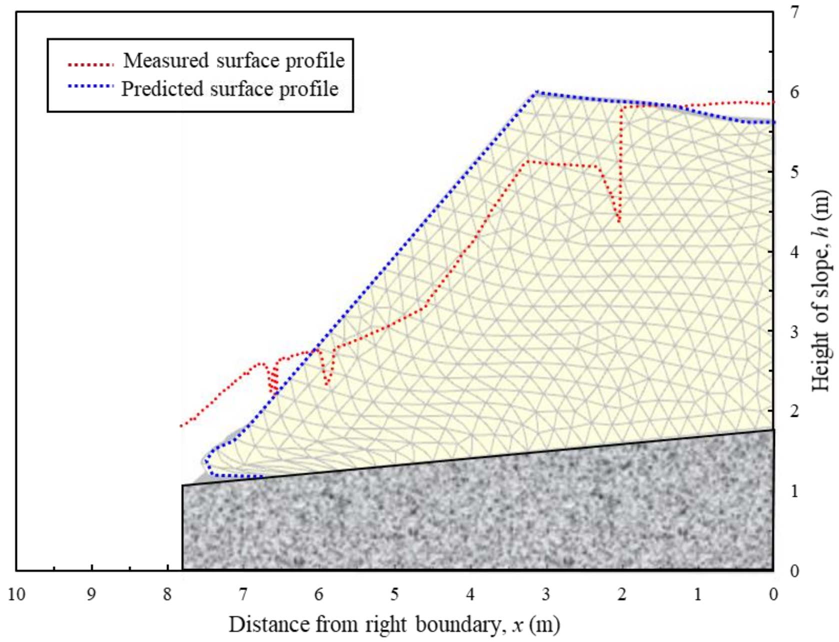

Figure 4.3: Validation by deformed surface profile of natural slope

Figure 4.4 provides a comparison of the progression of the phreatic surface in the predicted and measured results at the cross section of a natural slope subjected to seepage conditions. The experimental model was prepared with reconstituted soil, which was dried and mixed with water to achieve the desired compaction level and water content. In

doi:10.6342/NTU202301082

the process of soil reconstitution, matric suction is lost, leading to a substantial increase in permeability. Consequently, Finite Element (FE) analysis tends to predict the phreatic surface progression at different timings with some delay.

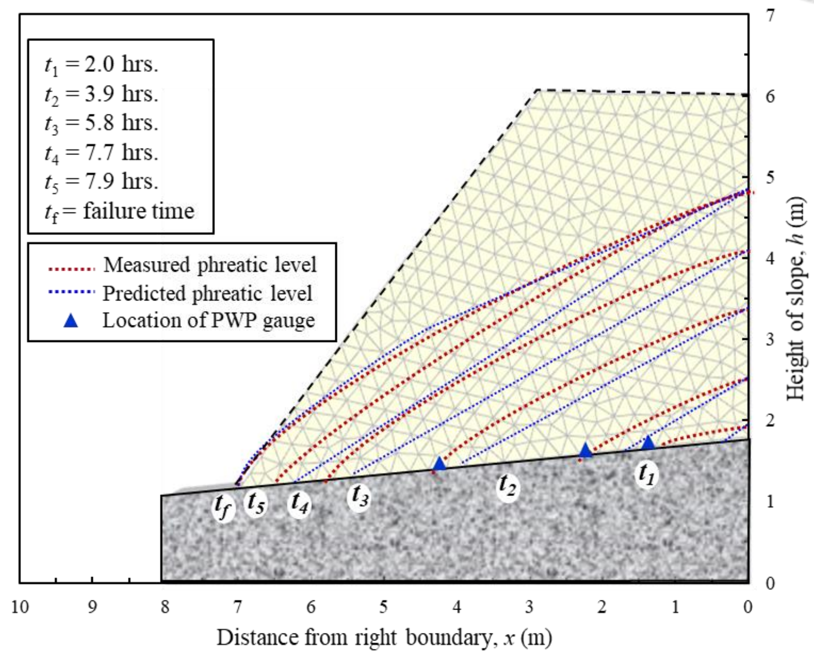

Figure 4.4: Validation by progression of phreatic surface of natural slope

doi:10.6342/NTU202301082

4.2 Experimental validation for GEC stabilized slope

Figure 4.5 demonstrates both experimental and numerical results of the final failure surface for the natural slope when subjected to seepage conditions. The results obtained show a close approximation in predicting the final failure surface of the natural slope.

Figure 4.6 offers a comparison of predicted and measured surface settlement profiles of the natural slope when subjected to seepage conditions. As mentioned in the previous section, the predicted and measured results generally align, except that the surface settlement is underestimated in Finite Element (FE) analyses.

Figure 4.7 provides a comparison of the progression of the phreatic surface in the predicted and measured results at the cross-section of the Geosynthetic Encased Column (GEC) stabilized slope when subjected to seepage conditions. In this instance, the FE analysis predicts a delayed phreatic surface at various timings.

doi:10.6342/NTU202301082

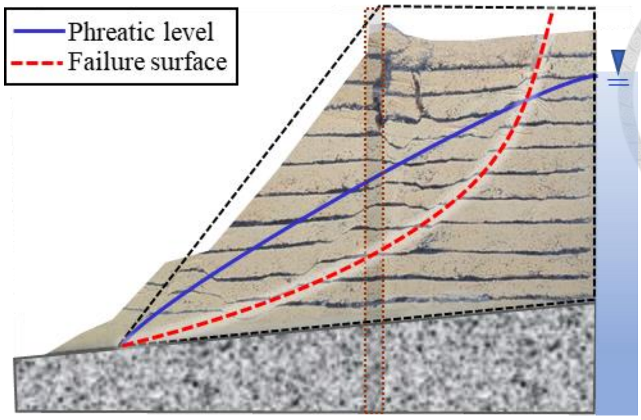

(a)

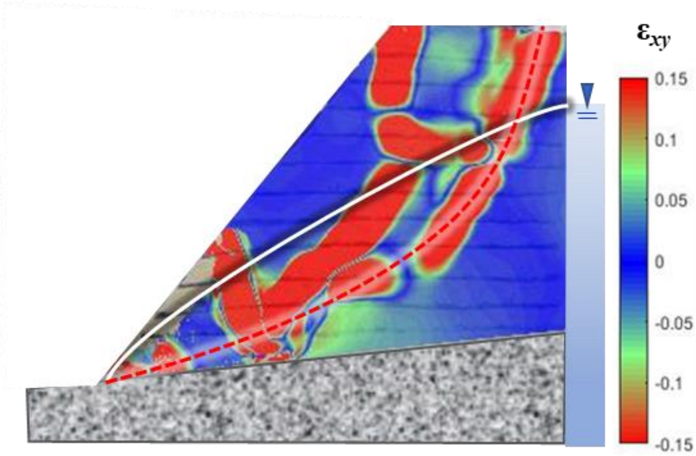

(b)

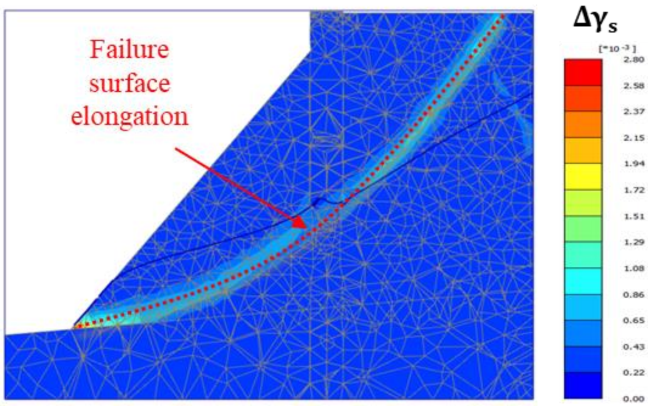

(c)

Figure 4.5: Validation by failure surface of natural slope; (a) observed failure surface of test model; (b) failure surface of test model by PIV analysis; and (c) failure surface by incremental deviatoric strain ($\Delta\gamma_s$) of numerical model

doi:10.6342/NTU202301082

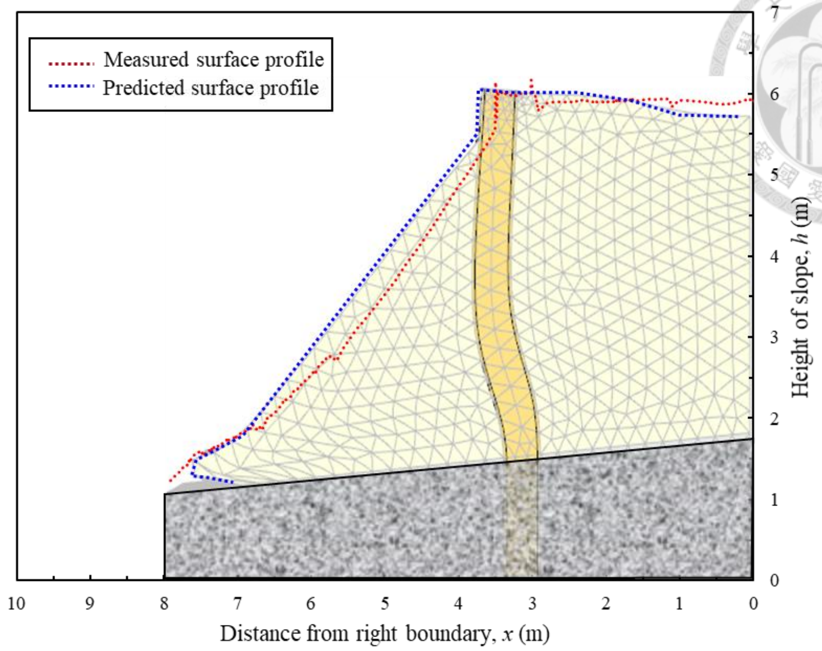

Figure 4.6: Validation by deformed surface profile of GEC stabilized slope

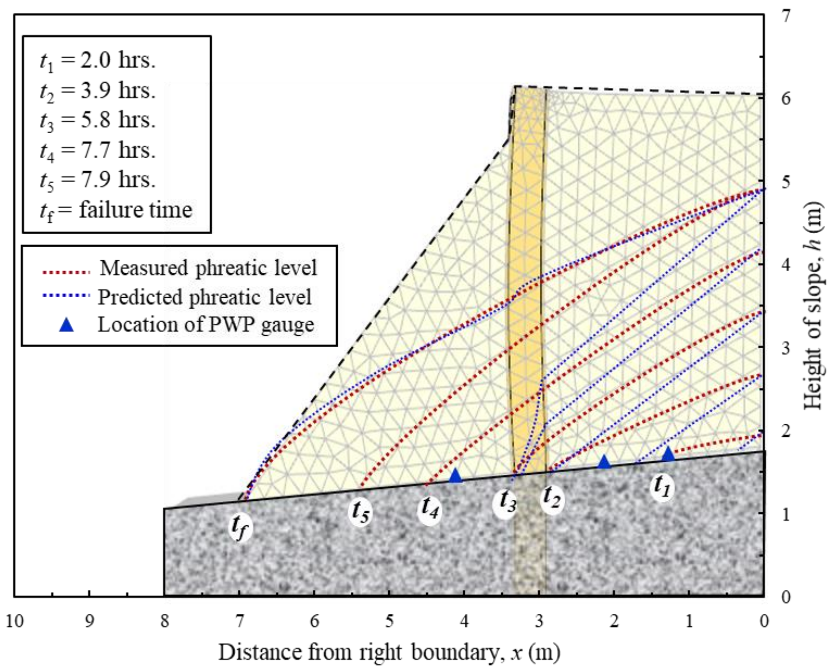

Figure 4.7: Validation by progression of phreatic surface of GEC stabilized slope

doi:10.6342/NTU202301082

Chapter 5 Numerical Results

This chapter presents a discussion on the model simulated through the Finite Element Method (FEM) and the associated results. Numerical models were established to simulate five prototype scale models: a natural slope, a rigid pile stabilized slope, a OSC stabilized slope, a GEC stabilized slope, and a GEC stabilized slope with horizontal drainage. A detailed failure mechanism is provided for a better understanding of the behavior. The results of numerical simulations were verified by 1-g reduced scale model tests. The test results demonstrated consistency with the performance achieved from the FEM simulations.

5.1 Numerical analyses of Natural slope

To assess the impact of soil and stabilizing parameters on the performance of GEC stabilized slope under seepage conditions, design methods were developed against various failure conditions such as failure surface elongation, failure surface diversion, failure surface isolation, and toe failure. These methods were developed under plane strain conditions using FEM software PLAXIS 3D. The 3D modelling boundaries were set in such a way that each vertical cross section displayed the same strain contour. In this manner, lateral boundary conditions did not influence the development of different failure surfaces across the lateral direction of the slope. Numerical and experimental results were compared for model validation to ensure the feasibility and reliability of the numerical results. The 1*g* model test results for the natural slope and GEC stabilized slope were adopted. These tests used the same soil and reinforcement materials and followed the same procedures and conditions as those in the 1-*g* model tests.

Figure 5.1 presents the dimensions and layout of the numerical models, which are

doi:10.6342/NTU202301082

identical to those of the 1-*g* model test. The dimensions of the numerical model are 8.0-m × 3.0-m × 6.0-m (*L* × *B* × *H*). A 15-node triangular element with 12 stress points was designated as the soil element, and a 5-node geogrid element with five stress points was assigned as reinforcement. The assigned mesh density generated approximately 25000 tetrahedral elements for a given geometry. The GEC included three rows with a constant *S/D* ratio of 2. However, at the boundary interface, it was simulated as a longitudinally half-cut cross section to allow observation of any visible deformation merely by observing the boundary. Interface elements were applied along each layer of geotextile to simulate soil-reinforcement interaction and capture reinforcement failure.

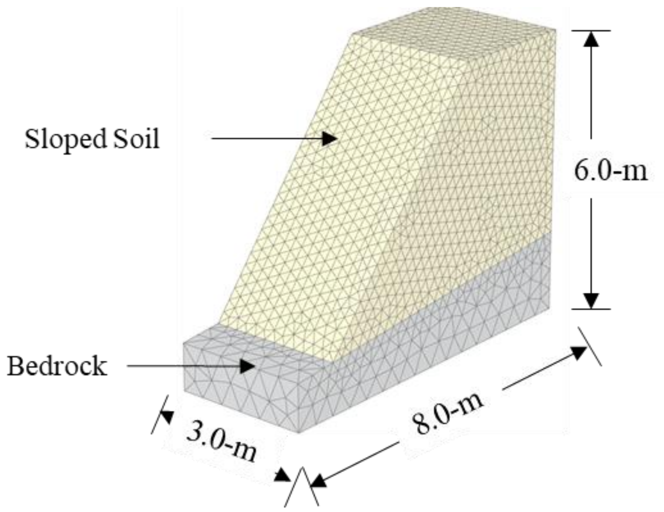

Figure 5.1: 3D numerical model of natural slope

doi:10.6342/NTU202301082

5.2 Numerical analyses of rigid pile stabilized slope

Figures 5.2 and 5.3 present the numerical model and numerical results of the rigid pile stabilized slope case subjected to seepage conditions, respectively. A non-circular failure surface was observed for the rigid pile stabilized slope in the numerical results, contrasting with the distinct failure surface seen in the natural slope. Due to the high flexural rigidity of the rigid pile, the failure surface could not penetrate towards the top of the slope. Moreover, very minimal horizontal deflection was noticed, suggesting that the seepage-induced failure zone is narrower than that of the natural slope. This indicates that stability is maintained on the stabilized slope side, while compromised on the existing slope side.

This stabilizing mechanism is identified as the diversion of the failure surface, in which the contribution of soil shear strain is not fully mobilized due to the loss in matric suction caused by seepage conditions. The impermeable concrete pile component is not able to effectively dissipate the excess pore water pressure. Therefore, the relatively insignificant contribution of the stiffer rigid pile makes it ineffective in the slope system subjected to slope failure caused by seepage.

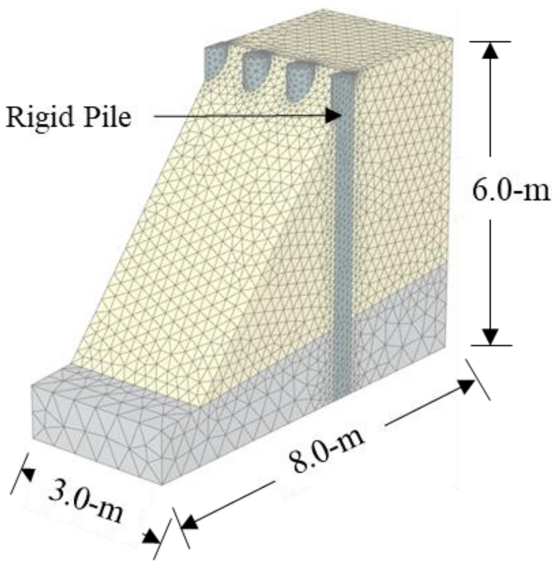

Figure 5.2: 3D numerical model of rigid pile stabilized slope

doi:10.6342/NTU202301082

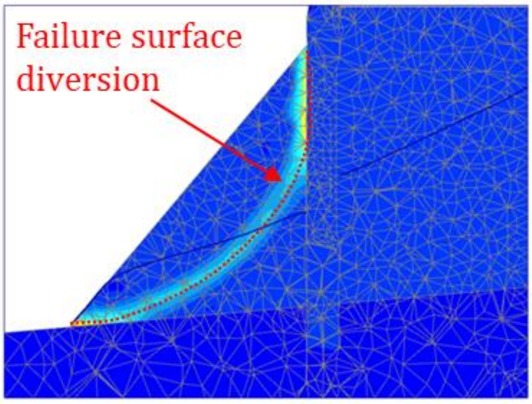

(a)

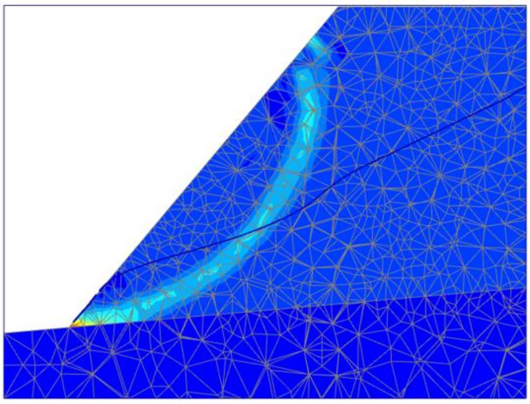

(b)

Figure 5.3: Numerical results of failure surface of rigid pile stabilized slope: (a) cross section considered through the rigid pile; and (b) cross section considered through the sloped soil

5.3 Numerical analyses of OSC stabilized slope

Figure 5.4 displays the numerical results of the OSC stabilized slope subjected to seepage conditions. A failure surface similar to that observed for the GEC stabilized slope in the numerical results was noted. Due to the lower flexural rigidity of the OSC compared to the rigid pile, the failure surface did not completely prevent penetration but instead elongated towards the top of the slope. This created a larger zone of slope subjected to failure compared to either the rigid pile stabilized slope or the natural slope.

This stabilizing mechanism, identified as the elongation of the failure surface, allows

doi:10.6342/NTU202301082

the soil shear strain to be mobilized due to the loss in matric suction caused by seepage conditions. This causes a steady and noticeable failure over a large part of the slope system. The absence of encasement reduced the failure timing, however no significant change in failure surface is noticed.

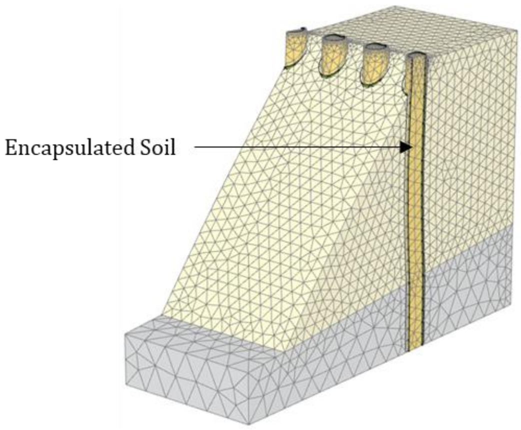

Figure 5.4: 3D numerical model of OSC stabilized slope

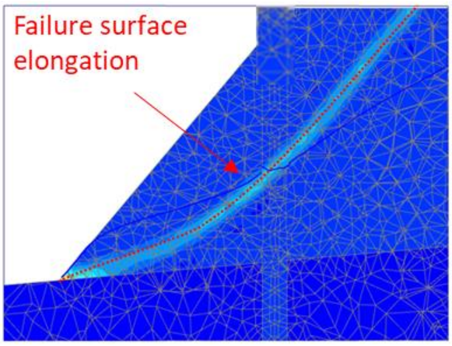

(a)

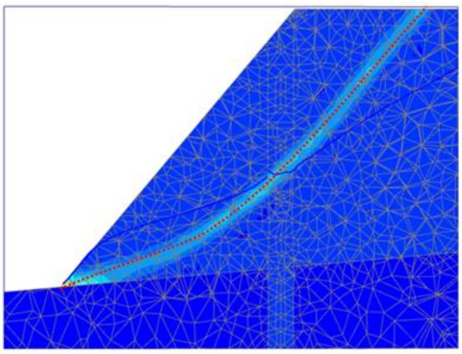

(b)

Figure 5.5: Numerical results of failure surface of OSC stabilized slope: (a) cross section considered through the OSC; and (b) cross section considered through the sloped soil

doi:10.6342/NTU202301082

5.4 Numerical analyses of GEC stabilized slope

Figure 5.6 displays the numerical results of the GEC stabilized slope subjected to seepage conditions. A circular failure surface similar to that observed for the natural slope was noted for the GEC stabilized slope in the numerical results. Due to the lower flexural rigidity of the GEC compared to the rigid pile, the failure surface did not completely prevent penetration but instead elongated towards the top of the slope. This created a larger zone of slope subjected to failure compared to either the rigid pile stabilized slope or the natural slope.

This stabilizing mechanism, identified as the elongation of the failure surface, allows the soil shear strain to be mobilized due to the loss in matric suction caused by seepage conditions. This causes a steady and noticeable failure over a large part of the slope system.

The GEC, with its permeable encased soil layer, delayed the failure timing by enabling dissipation of pore water pressure through its horizontal drainage capacity. As a result, the failure timing was longer compared to both the rigid pile stabilized slope and the natural slope. This significant contribution of the GEC makes it effective in slope systems subjected to slope failure caused by seepage.

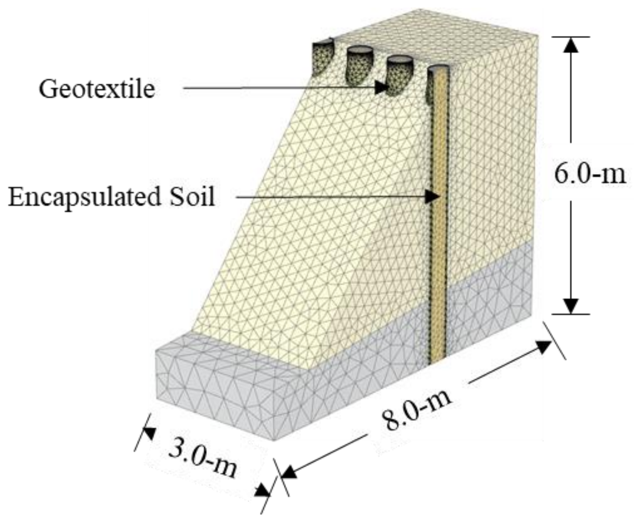

Figure 5.6: 3D numerical model of GEC stabilized slope

doi:10.6342/NTU202301082

5.5 Numerical analyses of GEC stabilized slope with horizontal drainage

Figure 5.7 and 5.8 showcase the numerical model and the numerical results of the Geosynthetic Encased Column (GEC) stabilized slope equipped with horizontal drainage and subjected to seepage conditions. The presence of horizontal drainage effectively dissipates all excess pore water pressure, which helps maintain a steady-state seepage condition with a factor of safety (FS) greater than 1 during the given period of transient seepage analysis. Interestingly, no failure surface is observed for the GEC stabilized slope with drainage, particularly in the numerical result.

The horizontal drainage has been simulated based on the drainage line elements with normal drainage conditions and a water pressure head of zero, as modelled in PLAXIS 3D. The effectiveness of these drainage line elements has been studied and validated by Wong (2013). An effective drainage system is constituted by a series of four horizontal drainage pipes, slightly inclined at an angle of 5°, inserted parallel inside the slope. Minimal horizontal deflection and settlement are observed for the slope system with drainage.

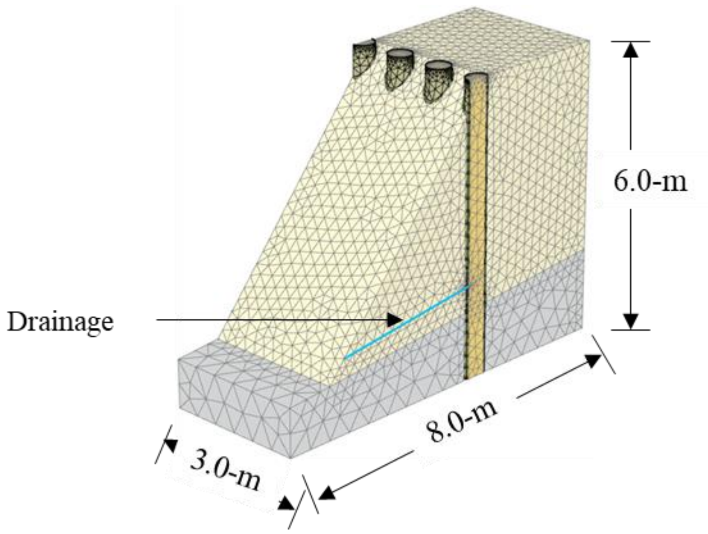

Figure 5.7: 3D numerical model of GEC stabilized slope with drainage

doi:10.6342/NTU202301082

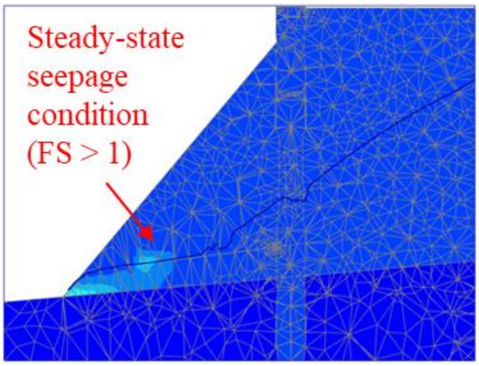

(a)

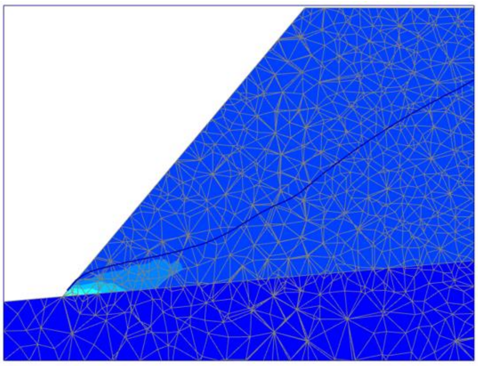

(b)

Figure 5.8: Numerical results of failure surface of GEC stabilized slope with drainage: (a) cross section considered through the GEC; and (b) cross section considered through the sloped soil

In summary, the Finite Element (FE) analyses were capable of accurately predicting the slope stability characteristics of the natural slope, the Geosynthetic Encased Column (GEC) stabilized slope, the rigid pile stabilized slope, and the GEC stabilized slope with drainage when subjected to extreme seepage conditions. The model validation results further confirm the suitability of the FE analysis employed in this study for investigating the performance of GEC stabilized slopes under extreme seepage conditions.

doi:10.6342/NTU202301082

5.6 Performance of various slope failure cases

Figure 5.9 shows the locations and purposes of the stress points considered for numerical analyses. All the points are located at the central vertical cross-section of the slope. Point-A, located in front of the stabilizing agents (e.g., Geosynthetic Encased Column (GEC), or rigid pile), predicts the progression of settlement of crest ($|u_z|$) for the existing sloped side. Point-B, located on the stabilized slope side, predicts the progression of settlement of top ($|u_z|$). The combined data from points A and B help to understand the extent of deformation occurring on either side of the existing or stabilized slope, or failure mechanism.

If increasing settlement at point-B is observed concurrently with horizontal deformation at point-A, this indicates a flexible slope system, which can be achieved by a GEC stabilized slope system. However, if an increase in settlement at point-B is not observed while horizontal deformation at point-A increases, it means the slope system is a rigid slope system, achieved by the rigid pile stabilized slope.

The location of point-C indicates the delay in the arrival of the phreatic surface or the maximum allowable positive pore water pressure before slope failure. It is expected that the presence of GEC would delay the progression of the phreatic surface due to its vertical drainage capacity, in contrast to the rigid pile, which is impermeable in nature.

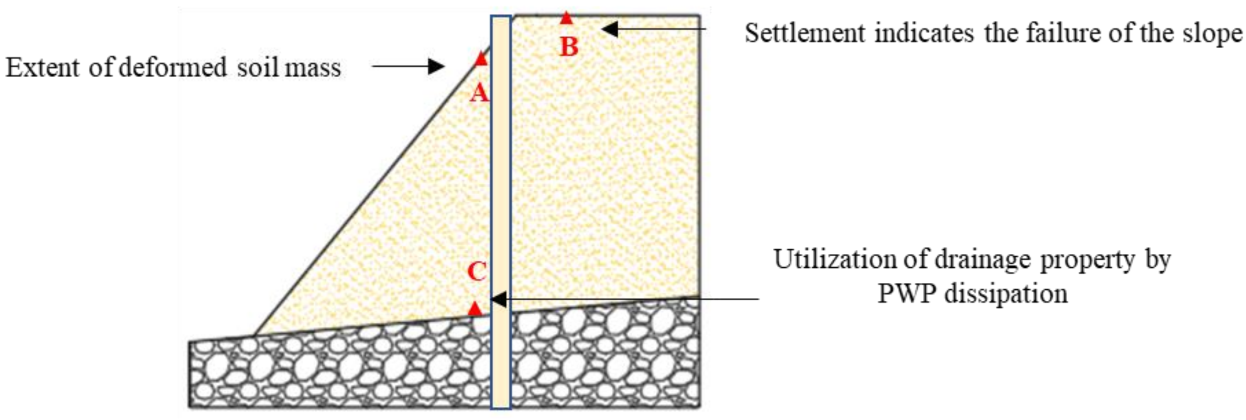

Figure 5.9: Locations of stress points considered for numerical analyses

doi:10.6342/NTU202301082

Figure 5.10(a) displays the progression of settlement of crest ($|u_z|$) at point-A. The results indicate that the natural slope failed earlier, while the Geosynthetic Encased Column (GEC) with drainage condition achieved a constant horizontal displacement with a factor of safety (FS) greater than 1. The GEC, being a flexible slope system, allowed for a larger displacement before failure, while the rigid pile-stabilized slope, a rigid slope system, failed allowing for a smaller displacement. The failure timing of the GEC stabilized slope is slightly longer than that of the rigid pile stabilized slope, suggesting that failure in a GEC stabilized slope is steady and provides ample time for failure detection.

Figure 5.10(b) displays the progression of settlement ($|u_z|$) at point-B. The results demonstrate that the natural slope experienced greater settlement, while the presence of the GEC effectively reduced the settlement of the natural slope and extended the time until failure. The settlement observed for the rigid pile stabilized slope is negligible, as the rigid pile, being part of a stiffer slope system, could restrain the movement of soil particles on the stabilized slope side. Notably, the GEC with drainage condition achieved a constant settlement with a FS greater than 1.

Figure 5.10(c) illustrates the dissipation of pore water pressure (*PWP*) at point-C. Seepage saturates the slope, which changes the soil state from unsaturated to saturated, leading to a shift from negative to positive pore water pressure as the saturation stage changes. The results indicate that the GEC delayed the development of pore water pressure more effectively than the rigid pile-stabilized slope. Moreover, the GEC with drainage condition maintained a constant pore water pressure lower than that of the GEC stabilized slope without drainage. Since the installed horizontal drainage effectively dissipated the pore water pressure, the slope reached a steady-state seepage condition with FS greater than 1.

doi:10.6342/NTU202301082

Figure 5.10(d) presents the deflection in the stabilizing agent. The GEC stabilized slope allowed for a larger deflection, while the value of deflection in the GEC was limited with the installation of horizontal drainage. In contrast, the rigid pile, with its higher flexural stiffness, allowed for very negligible horizontal deflection.

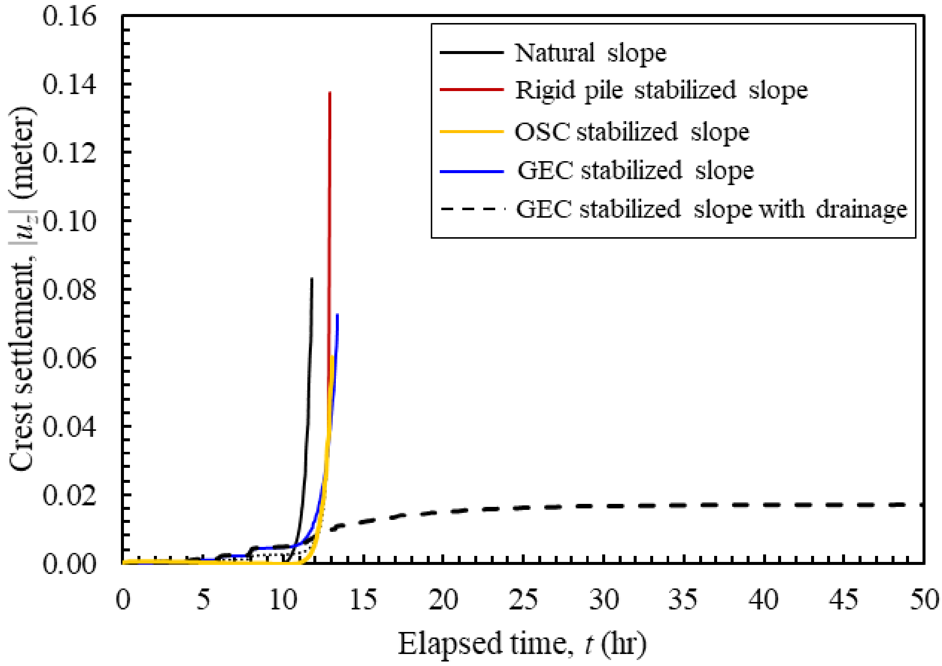

(a)

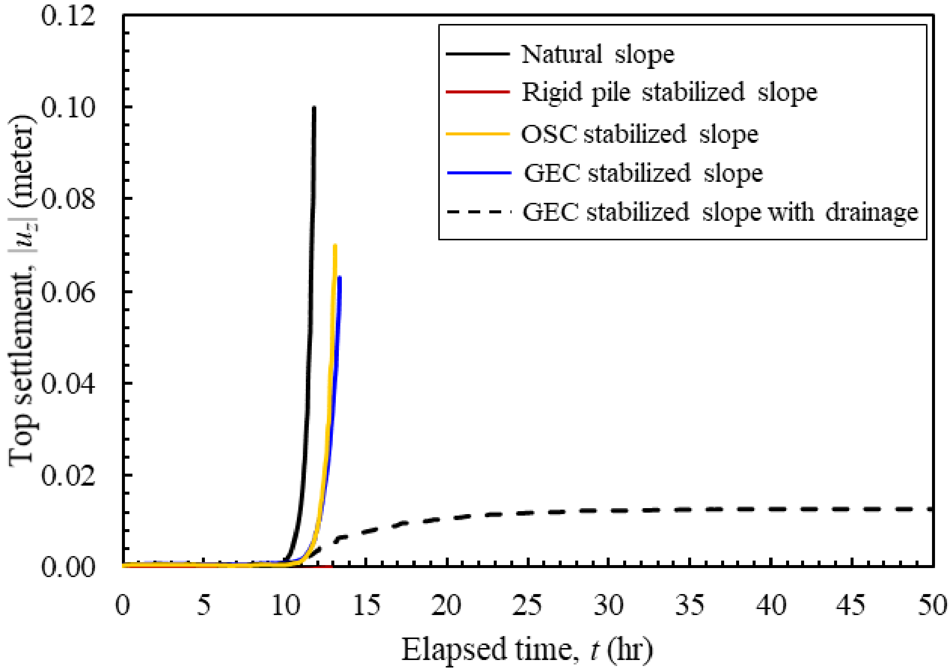

(b)

doi:10.6342/NTU202301082

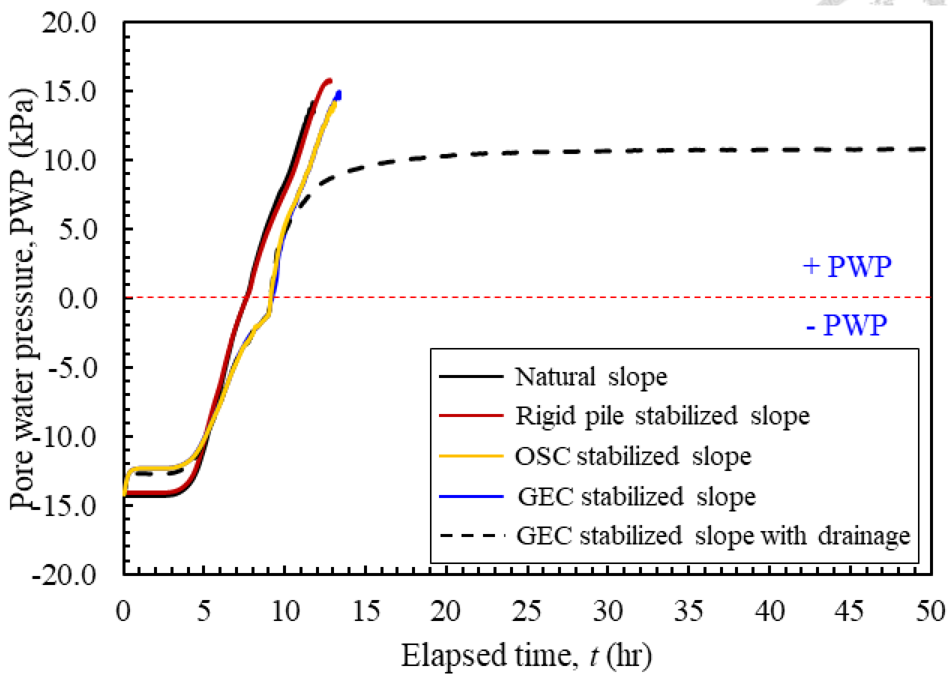

(c)

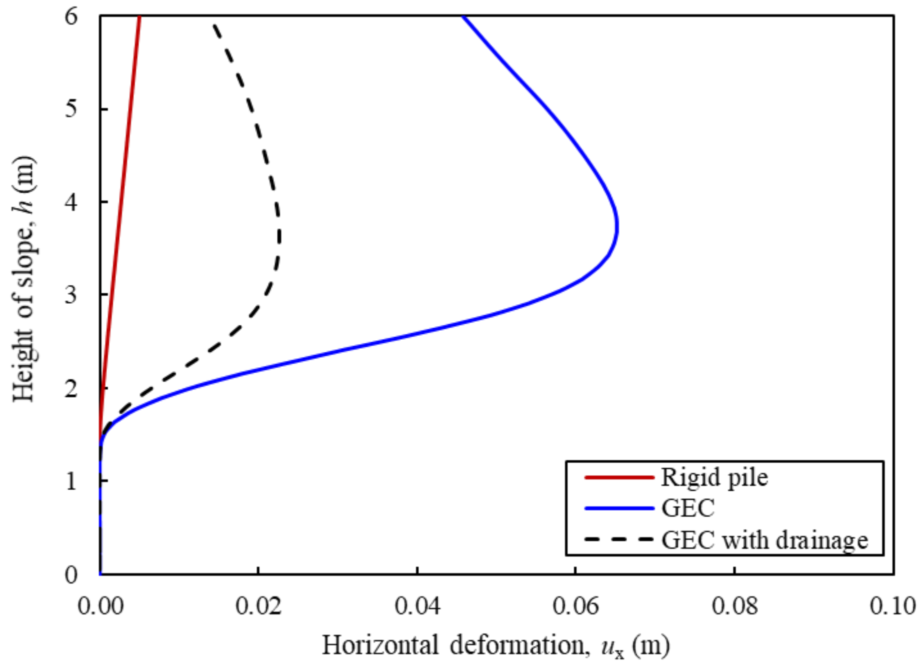

(d)

Figure 5.10: Numerical results of failure of slope systems by: (a) settlement of crest, $|u_z|$; (b) settlement of top, $|u_z|$; (c) dissipation of pore water pressure; and (d) deflection of stabilizing agents

doi:10.6342/NTU202301082

Failure mechanism of various slope failure cases could be summarized by three arguments:

(1) Delay in the development of a fully steady-state seepage condition: This feature is strongly influenced by the GEC's vertical drainage capacity, which enhances the hydraulic and mechanical properties of the slope. This mitigates seepage-induced slope failure by providing a controlled path for water to escape, thereby reducing pore-water pressure and stabilizing the slope.

(2) Failure surface diversion and elongation: In the case of a rigid pile-stabilized slope, the high flexural stiffness of the pile prevents significant deformation at the crest side of the natural slope. This, in turn, leads to a shallow failure condition, often at the interface between the sloped soil and the rigid pile. Contrastingly, GEC-stabilized slopes function harmoniously with the natural slope failure, allowing for the prolongation of the failure surface toward the inner side. In other words, GEC allows for soil displacement, meeting the performance criteria even under failure conditions.

(3) Shear strain mobilization: GEC not only allows for the mobilization of shear strain but also aids in utilizing the residual shear strength of sloped soil, particularly when the proper horizontal drainage conditions are maintained. By doing so, the slope avoids further deformation, and the water level reaches a steady state, allowing for an equilibrium condition. This balance between mechanical strength and hydraulic conditions is crucial for the stability of slopes under seepage conditions.

Overall, research provides valuable insights into the effectiveness of different slope stabilization methods under seepage conditions, with critical implications for geotechnical engineering practices.

doi:10.6342/NTU202301082

5.7 Influence of arching effect

Discussion on soil arching effect provides a detailed understanding of different slope stabilization methods and its influence on the stress distribution in slopes under seepage conditions. The soil arching effect refers to the phenomenon where stress concentrates at areas of higher stiffness, reducing the horizontal stress on the surrounding soil. This phenomenon is significantly influenced by the flexural rigidity of the stabilization structure, with rigid piles causing a pronounced soil arching effect due to their high bending stiffness (Figure 5.11).

The high bending stiffness of rigid piles restricts soil displacement, leading the soil to behave under "at rest" conditions for lateral earth pressure. The stress contours reveal a concave shape, indicating areas of stationary soil particles with high mobilized stress. The stress concentration around the rigid pile is substantial, demonstrating a strong soil arching effect. However, the movement of soil on the existing slope side eventually results in slope failure.

Contrary to rigid piles, GECs, due to their lower bending stiffness, allow soil displacement, leading to "active" conditions for lateral earth pressure. The stress contours reveal a convex shape, indicative of soil particle movement on both sides of the slope. The stress concentration around the GEC is lower compared to rigid piles, indicating a less pronounced soil arching effect.

GEC stabilized slope with drainage case illustrates that the soil arching effect can be further mitigated. The addition of drainage decreases the influence of the soil arching effect significantly, and interestingly, the phreatic surface is positioned behind the stabilization structure. This implies that the drainage allows better management of pore water pressure, preventing saturation of the soil and thereby maintaining slope stability.

doi:10.6342/NTU202301082

In summary, the nature of stress distribution and the impact of soil arching effect on slopes is largely governed by the flexural rigidity and permeability of the slope stabilization structures.

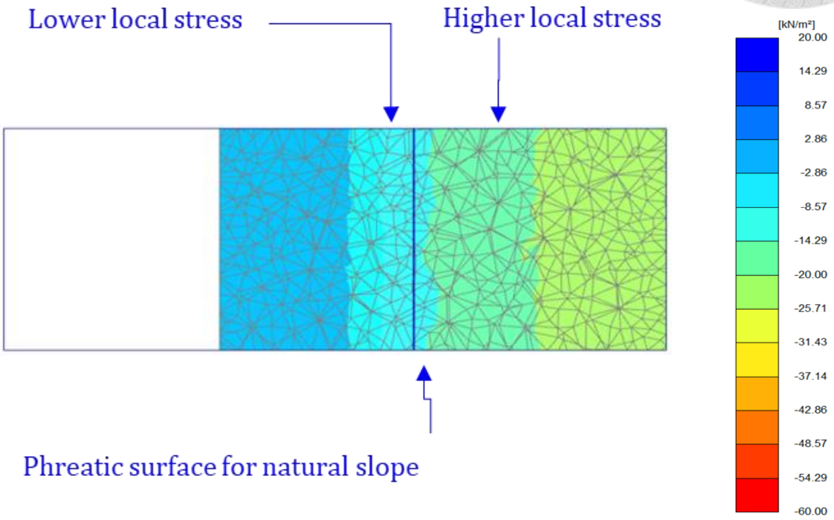

(a)

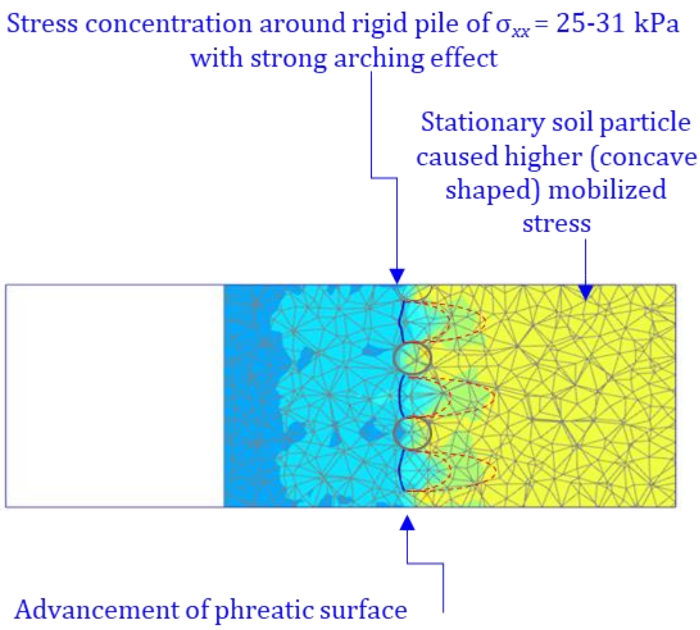

(b)

doi:10.6342/NTU202301082

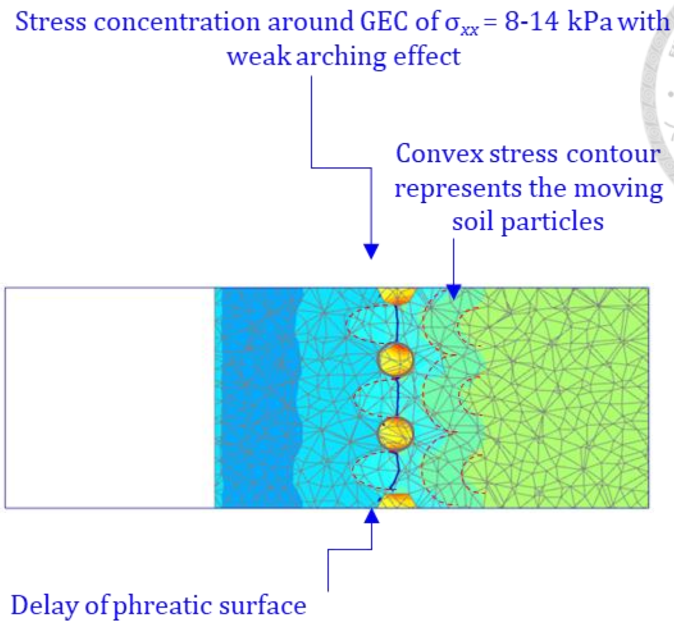

(c)

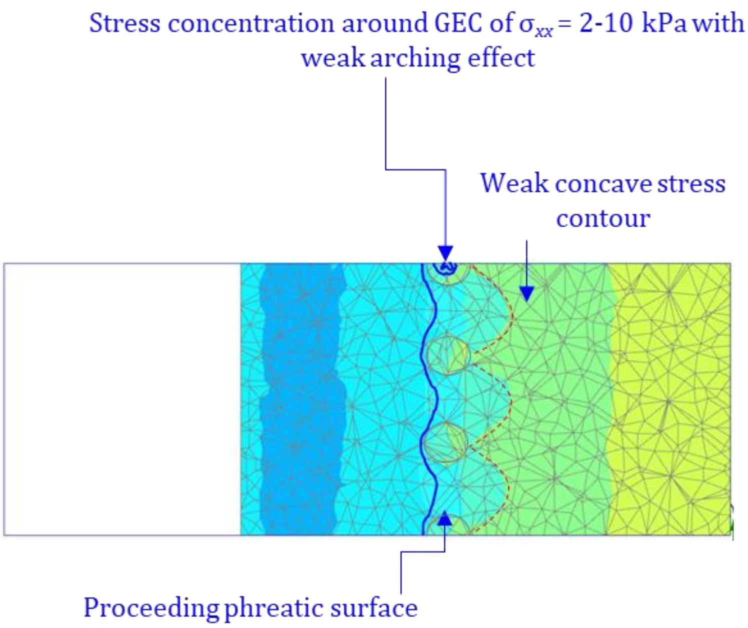

(d)

Figure 5.11: Numerical results of contour of horizontal stress (σ_{xx}) at slope height of 3.0-m: (a) natural slope; (b) rigid pile stabilized slope; (c) GEC stabilized slope; and (d) OSC stabilized slope

doi:10.6342/NTU202301082

Chapter 6 Parametric Study

A comprehensive series of parametric studies were conducted on the full-scale Geosynthetic Encased Column (GEC) stabilized slope subjected to seepage. The objective of these studies was to evaluate the effects of various soil and reinforcement parameters on the performance of the GEC stabilized slope. The results and numerical program of these parametric studies are systematically presented in Tables 6.1 and 6.2. The parameters considered in this study were grouped into four main categories, each representing a distinct aspect of the slope system: encased soil properties, geotextile properties, slope features, and installation workmanship. In detail, the specific variables explored within these categories were: (1) reinforcement stiffness ($J_{50\%}$); (2) stiffness properties of the encased soil (E_{50}^{ref}); (3) shear strength parameters of the encased soil (c' and φ'); (4) relative permeability of encased soil to sloped soil (k_e/k_s); (5) ratio of spacing to diameter (S/D) for GEC placement; (6) diameter (D) of GEC; and (8) location of GEC. Each of these parameters was meticulously adjusted within the numerical model to understand its role and influence on the overall stability and performance of the GEC stabilized slope.

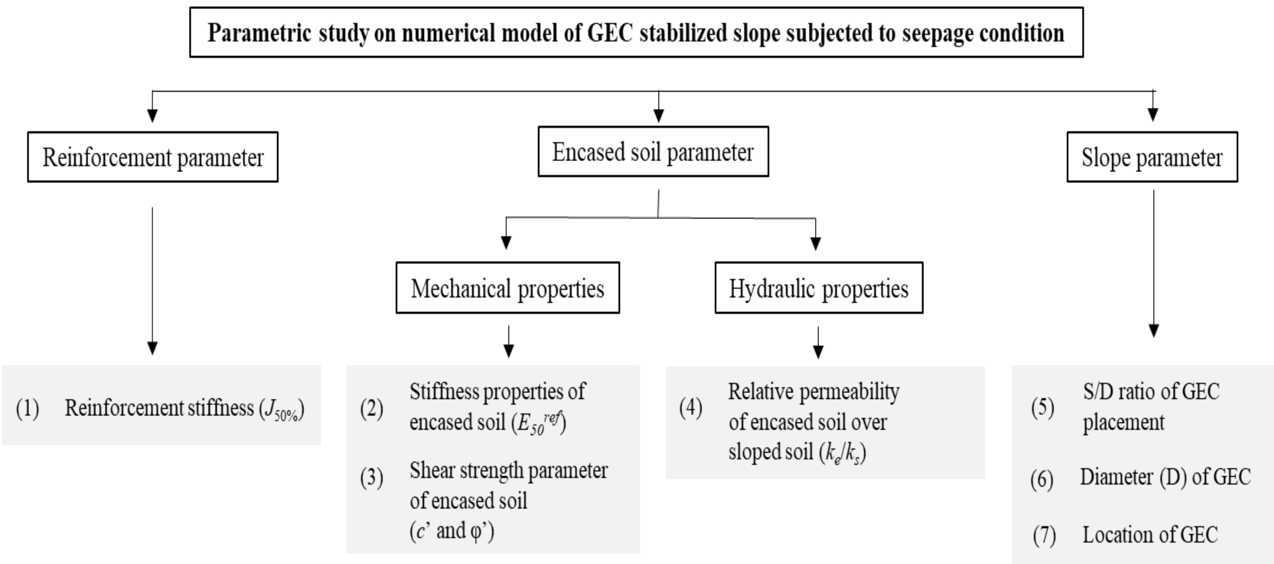

Figure 6.1: Flowchart for parametric study on numerical model

doi:10.6342/NTU202301082

Table 6.1: Numerical program for parametric study

Model	Parameters								
	Notation	S/D ratio	Diameter	Shear strength parameter	Encased Soil	Relative permeability	Reinforcement stiffness	Reinforcement ultimate tensile strength	Interface reduction factor
			d (m)	c' and ϕ'	$E_{50}^{ref} = E_{oed}^{ref} = E_{ur}^{ref}/3$	$(k_{sat\text{-}encased}/k_{sat\text{-}sloped})$	$J_{50\%}$ (kN/m)	T_{ult} (kN/m)	R_{inter} (-)
Natural slope	*N*	-	-	-	-	-	-	-	-
OSC stabilized slope	*O*	2	0.5	1 and 34.7	45000	14.11	-	-	-
GEC stabilized slope	G_m	2	0.5	1 and 34.7	45000	14.11	547	70	0.71
Rigid pile stabilized slope	*R*	2	0.5	-	-	-	-	-	-
GEC stabilized slope with drainage	*GD*	2	0.5	1 and 34.7	45000	14.11	547	70	0.71
Reinforcement stiffness	$G\_J_{50\%}=1000/70$	2	0.5	1 and 34.7	45000	14.11	**1000**	**70**	0.71
	$G\_J_{50\%}=2000/70$						**2000**		
	$G\_J_{50\%}=2000$						**2000**	**300**	0.71
	$G\_J_{50\%}=6000$						**6000**		
	$G\_J_{50\%}=10000$						**10000**		
	$G\_J_{50\%}=14000$						**14000**		
Encased soil stiffness	*G_E=75000*	2	0.5	1 and 34.7	**75000**	14.11	547	70	0.71
	G_E=100000				**100000**				
Shear strength parameter	*G_S=1*	2	0.5	2 and 38					
	G_S=2			4 and 40					
	G_S=3			5 and 42					
Relative permeability	$G\_k_e/k_s=10^0$	2	0.5	1 and 34.7	45000	**1**	547	70	0.71
	$G\_k_e/k_s=10^1$					**10**			
	$G\_k_e/k_s=10^2$					**100**			
	$G\_k_e/k_s=10^3$					**1000**			
S/D ratio	*G_S/D=1*	**1**	0.5	1 and 34.7	45000	14.11	547	70	0.71
	G_S/D=3	**3**							
Diameter	*G_D=0.75*	2	**0.75**	1 and 34.7	45000	14.11	547	70	0.71
	G_D=1		**1**						

doi:10.6342/NTU202301082

Table 6.2: Numerical results for parametric study

Model	Notation	Results					
		Failure timing t_f **(hr)**	**Crest settlement,** u_z **(m)**	**Top settlement,** u_z **(m)**	**PWP at failure, kPa**	**Max. horizontal deformation of GEC,** δ_x **(m)**	**Max. hoop strain of GEC,** $\varepsilon_{h,max}$ **(%)**
Natural slope	*N*	11.75	0.083	0.100	14.163	-	-
OSC stabilized slope	*O*	13.07	0.017	0.069	13.961	-	-
GEC stabilized slope	G_m	13.56	0.072	0.063	14.909	0.065	2.87
Rigid pile stabilized slope	*R*	12.82	0.137	0.001	15.729	0.005	0.00
GEC stabilized slope with drainage	*GD*	50.00	0.020	0.012	10.831	0.023	-
Reinforcement stiffness	$G\_J_{50\%}=1000/70$	14.05	0.089	0.065	15.657	0.064	2.04
	$G\_J_{50\%}=2000/70$	13.78	0.075	0.053	15.716	0.064	1.15
	$G\_J_{50\%}=2000$	13.78	0.069	0.053	15.716	0.064	1.15
	$G\_J_{50\%}=6000$	13.75	0.066	0.047	15.433	0.062	0.98
	$G\_J_{50\%}=10000$	13.63	0.063	0.038	15.200	0.061	0.87
	$G\_J_{50\%}=14000$	13.57	0.058	0.034	14.654	0.596	0.75
Encased soil stiffness	*G_E=75000*	13.36	0.068	0.047	15.189	0.060	2.66
	G_E=100000	13.28	0.054	0.029	14.602	0.051	2.27
Shear strength parameter	*G_S=1*	13.66	0.083	0.074	15.606	0.062	2.85
	G_S=2	13.74	0.076	0.065	15.635	0.056	2.82
	G_S=3	13.86	0.073	0.065	15.781	0.053	2.76
Relative permeability	$G\_k_e/k_s=10^0$	12.66	0.052	0.046	13.534	0.068	2.27
	$G\_k_e/k_s=10^1$	13.22	0.070	0.052	14.653	0.064	2.23
	$G\_k_e/k_s=10^2$	13.13	0.066	0.058	14.739	0.065	2.16
	$G\_k_e/k_s=10^3$	13.27	0.061	0.054	14.638	0.072	2.08
S/D ratio	*G_S/D=1*	13.96	0.042	0.061	14.507	0.063	0.83
	G_S/D=3	12.68	0.093	0.081	15.462	0.079	3.91
Diameter	*G_D=0.75*	13.86	0.065	0.049	15.253	0.014	2.54
	G_D=1	14.84	0.059	0.045	13.875	0.009	2.44

doi:10.6342/NTU202301082

6.1 Reinforcement stiffness ($J_{50\%}$)

Figure 6.2 illustrates the impact of reinforcement stiffness ($J_{50\%}$) on the progression of settlement at the crest of the slope ($|u_z|$), settlement at the top of the slope ($|u_z|$), and dissipation of pore water pressure (*PWP*). It is important to note that the baseline strength properties of the geotextile used in the numerical models are $J_{50\%}$ = 547 kN/m and T_{ult} = 70 kN/m. Three values are considered: $J_{50\%}$ = 547, 1000, and 2000 kN/m, while the ultimate tensile strength (T_{ult}) remains constant at 70 kN/m. The numerical results reveal that an increase in stiffness initially leads to a reduction in horizontal displacement. However, beyond a certain threshold, increasing stiffness does not halt the increase in horizontal displacement. On the other hand, a higher stiffness value results in a reduction of settlement. Interestingly, the dissipation of pore water pressure appears to be largely unaffected by changes in $J_{50\%}$. This is because $J_{50\%}$ does not directly impact the hydraulic properties of the slope system.

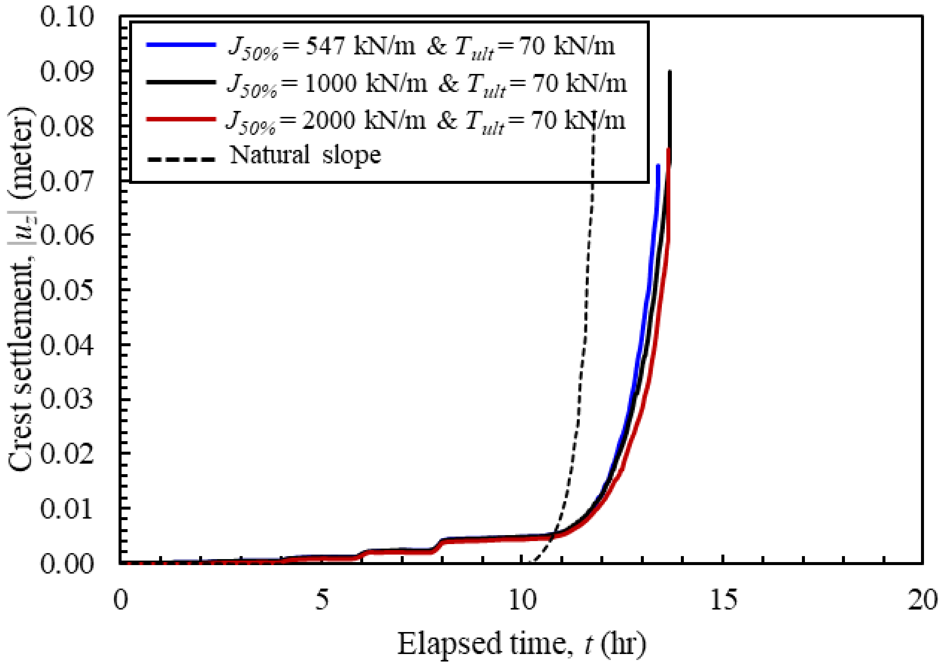

(a)

doi:10.6342/NTU202301082

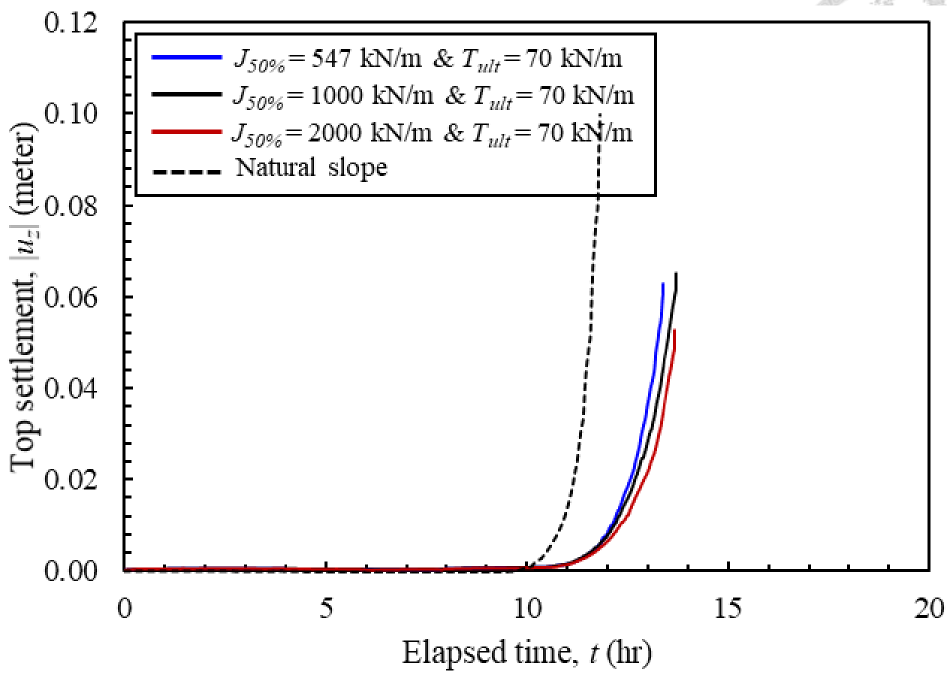

(b)

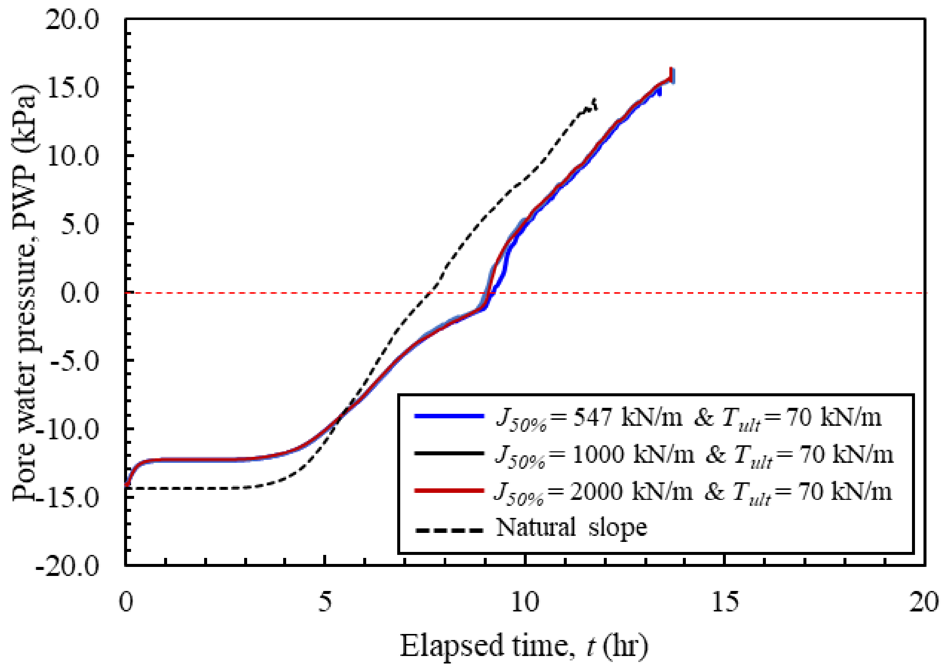

(c)

Figure 6.2: Influence of reinforcement stiffness ($J_{50\%}$) on: (a) progression of settlement of crest ($|u_z|$); (b) progression of settlement of top ($|u_z|$); and (c) dissipation of pore water pressure (PWP)

doi:10.6342/NTU202301082

Increasing the value of $J_{50\%}$ corresponds to an increase in the stiffness of the GEC stabilized slope system. This transition alters the behavior of the GEC from a flexible structure to a rigid one, thereby causing changes in the failure surface. Consequently, with some degree of increased stiffness in reinforcement, there is an increment in the timing of failure. However, further increases in stiffness result in premature slope failure. As depicted in Figure 6.3, the developed failure shear strain is not sufficiently extensive to reach the top of the slope. Consequently, the diversion of the failure surface does not benefit from the mobilization of soil shear strain. Once the failure surface has been diverted, the observed movement in the soil mass no longer comprises a significant portion of the slope system. As a result, slope failure occurs sooner.

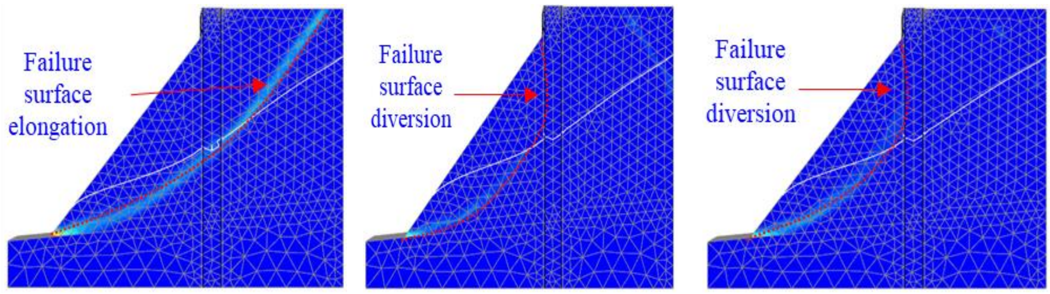

(a) (b) (c)

Figure 6.3: Influence of reinforcement stiffness ($J_{50\%}$) on incremental deviatoric strain ($\Delta\gamma_s$) for: (a) $J_{50\%}$ = 547 kN/m; (b) $J_{50\%}$ = 1000 kN/m; and (c) $J_{50\%}$ = 2000 kN/m

doi:10.6342/NTU202301082

The behavior observed can be interpreted in terms of the soil arching effect. Figure 6.4 illustrates the contour of horizontal stress at mid-height (3.0-m) of the slope, which helps explain the soil arching effect. For ease of comparative study, several key aspects need to be contrasted: (1) confining stress in encased soil, (2) the position of the phreatic surface, and (3) the convexity of the stress distribution contour.

An increase in confining stress indicates that the stiffer GEC system resists the mobilization of strain in the stabilized soil against failure, potentially causing a diversion of the failure surface. The concentration of stress within the GEC increases with an increase in $J_{50\%}$. In such instances, the development of the failure surface towards the upslope side is inhibited. This is further supported by the convexity of the stress distribution contour. The convex shape of the horizontal stress contour indicates uneven stress distribution near the stiffer zone within a slope system. As $J_{50\%}$ increases, the convexity of the GEC stabilized slope decreases, while the stress contour near the GEC begins to adopt a concave shape with a larger stress zone on the stabilized slope side. This indicates a reduction in soil movement on the stabilized slope side as the rigidity of the slope system increases. Lastly, the position of the phreatic surface indicates the development of a steady-state phreatic level. With an increase in $J_{50\%}$, the phreatic surface shifts towards the toe side of the slope prior to failure. This indicates that the slope is rigid enough to sustain higher pore water pressure values prior to failure with significant movement on the stabilized slope side.

doi:10.6342/NTU202301082

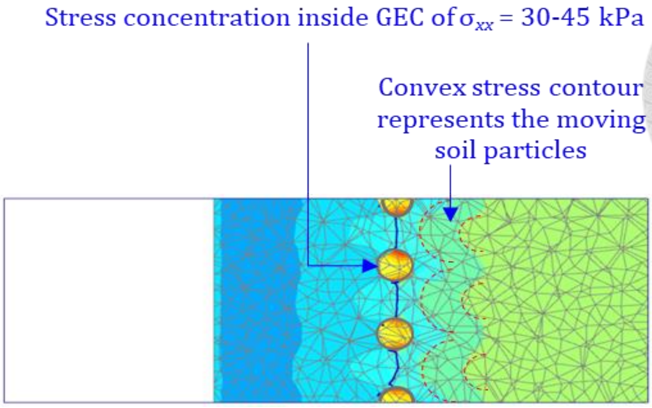

(a)

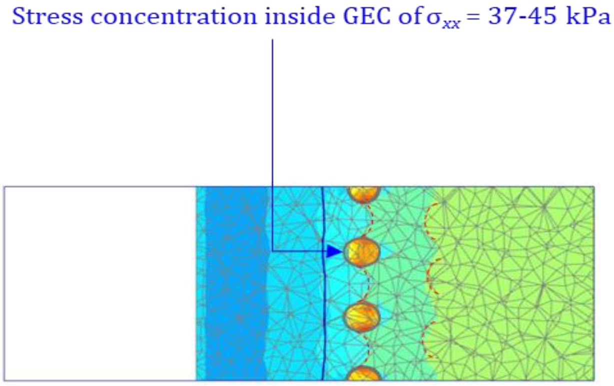

(b)

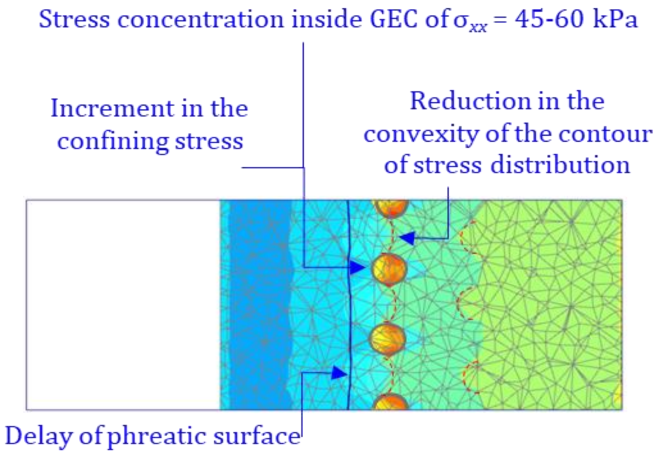

(c)

Figure 6.4: Influence of reinforcement stiffness ($J_{50\%}$) on contour of horizontal stress (σ_{xx}) at slope height of 3.0-m for: (a) $J_{50\%}$ = 547 kN/m; (b) $J_{50\%}$ = 1000 kN/m; and (c) $J_{50\%}$ = 2000 kN/m

doi:10.6342/NTU202301082

Figure 6.5 illustrates the cross-section of the maximum hoop strain that develops in the geotextile of the GEC. The location of this maximum hoop strain can indicate the probable location of GEC failure. The maximum hoop strain in any given cross section of the geotextile reduces with an increase in $J_{50\%}$. A reduction in hoop strain suggests a diversion of the failure surface where the GEC, with insignificant horizontal movement, inhibits the mobilization of soil particles on the stabilized slope side. The maximum reinforcement tensile force (T_{max}) for the reinforcement layer can be computed as:

$$T_{\max} = J_{50\%} \times \varepsilon_{\max} \tag{5.1}$$

where $J_{50\%}$ is the reinforcement secant stiffness, and ε_{max} is the mobilized maximum tensile strain in the reinforcement layer.

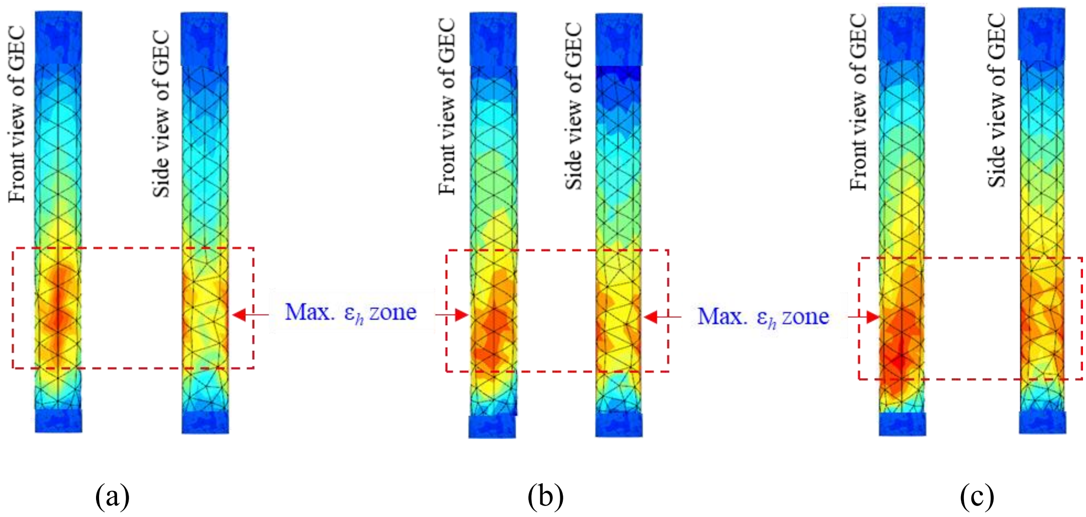

Figure 6.5: Influence of reinforcement stiffness ($J_{50\%}$) on geotextile hoop strain of GEC for: (a) $J_{50\%}$ = 547 kN/m; (b) $J_{50\%}$ = 1000 kN/m; and (c) $J_{50\%}$ = 2000 kN/m

Figure 6.6 depicts the horizontal deformation at the centerline of the retaining column (GEC). It can be observed that the deformation of the column diminishes as the stiffness of the reinforcement increases, and conversely, the deformation augments with a decrease in reinforcement stiffness. This finding demonstrates the inverse relationship

doi:10.6342/NTU202301082

between the stiffness of the reinforcement and the horizontal deformation of the retaining column, reinforcing the crucial role of the reinforcement's stiffness in slope stabilization.

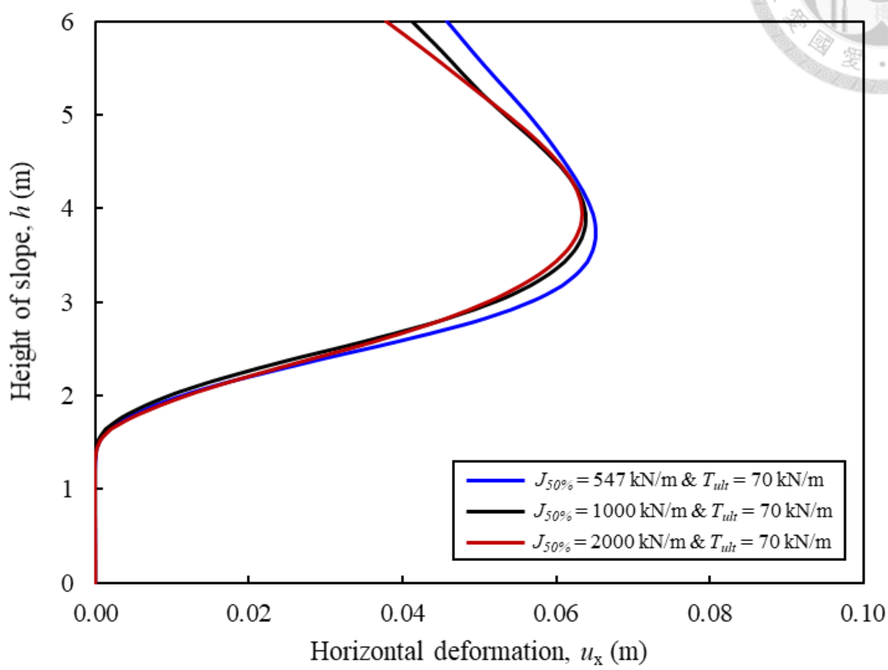

Figure 6.6: Influence of reinforcement stiffness ($J_{50\%}$) on horizontal deformation of GEC

Additional parametric studies are conducted considering a practical ultimate tensile strength (T_{ult}) of 300 kN/m for various stiffness values ($J_{50\%}$) including 2000, 6000, 10000, and 14000 kN/m, as outlined in Table 6.1. The variation in T_{ult} values do not significantly impact the results pertaining to horizontal displacement, settlement, and pore water pressure dissipation. This outcome suggests that slope failure does not typically occur due to rupture failure. Therefore, it is deduced that the influence of ultimate tensile strength (T_{ult}) on the progression of horizontal displacement, settlement, and dissipation of pore water pressure is essentially negligible.

doi:10.6342/NTU202301082

6.2 Stiffness of encased granular soil (E_{50}^{ref})

In this study, the hardening soil model is adopted to represent the encased soil, underscoring the importance of capturing the stiffness of such soil which represents the variety of granular soil types encapsulated. The baseline encased granular soil for this investigation is sand, however, encased soil of greater stiffness could also include stone or gravel. The stiffness values are determined based on the hardening soil model with the values of E_{50}^{ref} set at 45000 kPa, 75000 kPa, and 100000 kPa. The relationships regarding the stiffness of the encased soil are thus considered as follows:

$$E_{50}^{ref} = E_{oed}^{ref} = \frac{E_{ur}^{ref}}{3} \qquad (5.2)$$
$$v_{ur} = 0.2$$

Figure 6.7 presents the effects of the stiffness of encased granular soil on the progression of horizontal displacement, settlement, and pore water pressure, with all other parameters remaining constant. The numerical results suggest that horizontal displacement increases with increasing stiffness, settlement decreases with increasing stiffness, and the influence on pore water pressure dissipation is negligible.

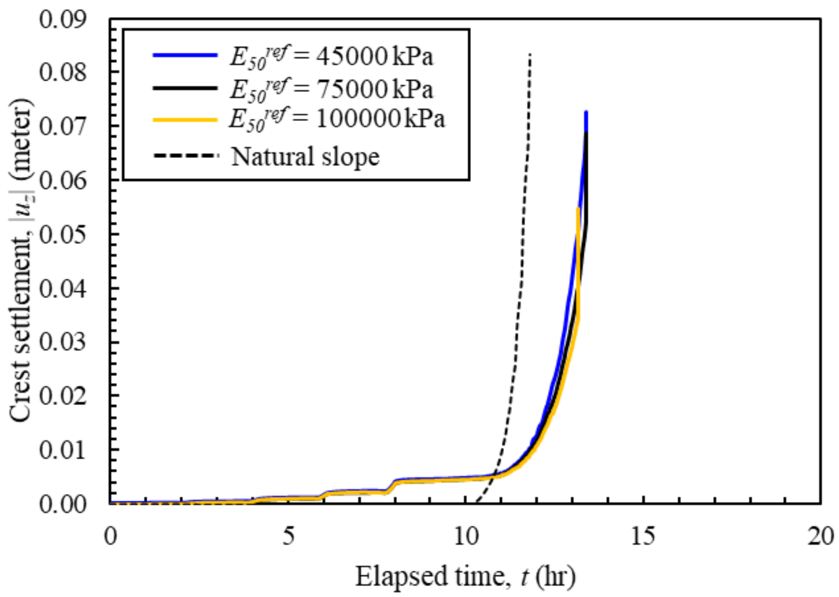

(a)

doi:10.6342/NTU202301082

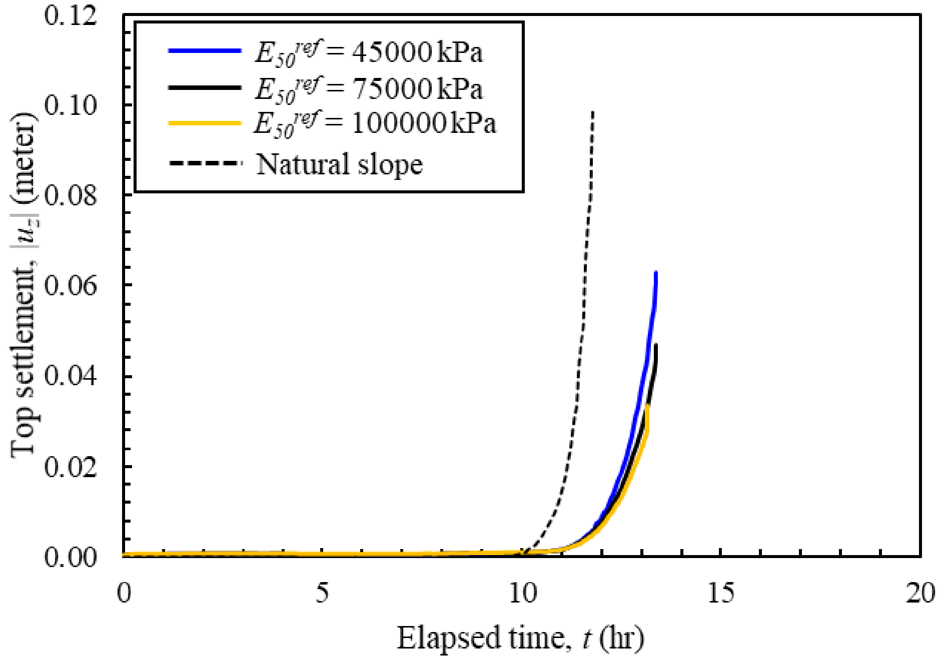

(b)

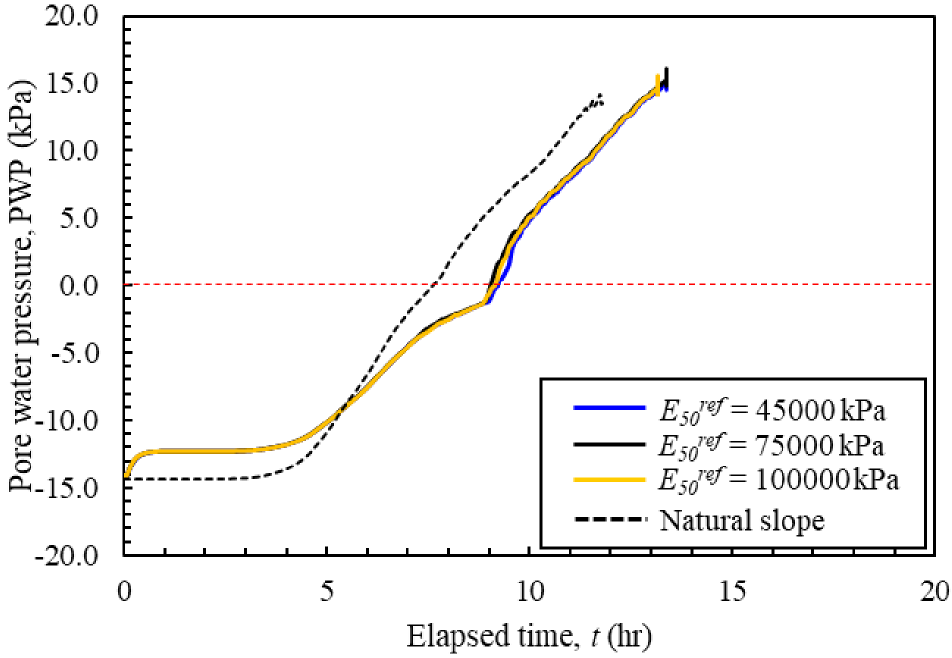

(c)

Figure 6.7: Influence of stiffness of encased granular soil (E_{50}^{ref}) on: (a) progression of settlement of crest ($|u_z|$); (b) progression of settlement of top ($|u_z|$); and (c) dissipation of pore water pressure (PWP)

doi:10.6342/NTU202301082

As illustrated in Figure 6.8, an increase in stiffness correlates with a diversion in the failure surface. This observation is further reinforced by the characteristics of the horizontal stress contour, which presents a diminishing convexity of the contour as shown in Figure 6.9. A decrease in hoop strain, as tabulated in Table 6.2, along with alterations in the deformation of the GEC as represented in Figure 6.10, also lend credence to this assertion. Detailed discussions pertaining to these arguments have been elaborated in the preceding sections.

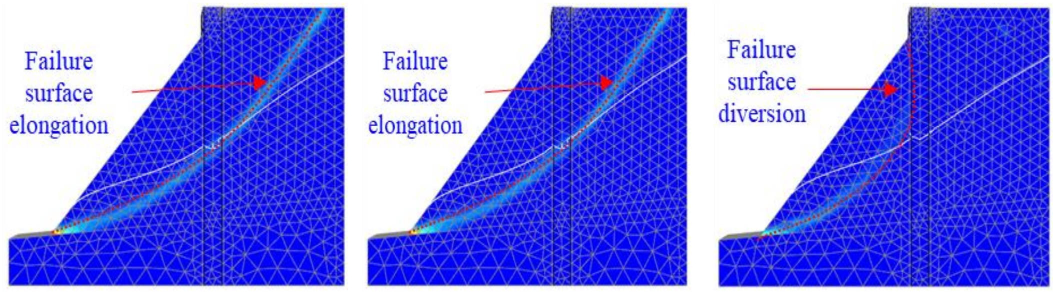

Figure 6.8: Influence of stiffness of encased granular soil (E_{50}^{ref}) on incremental deviatoric strain ($\Delta\gamma_s$) for: (a) E_{50}^{ref} = 45000 kPa; (b) E_{50}^{ref} = 75000 kPa; and (c) E_{50}^{ref} = 100000 kPa

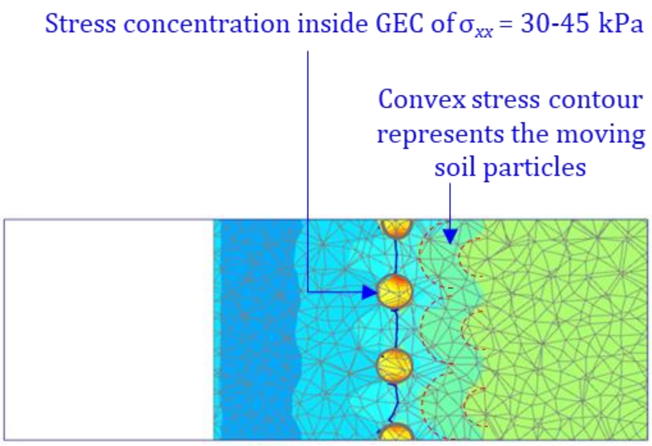

(a)

doi:10.6342/NTU202301082

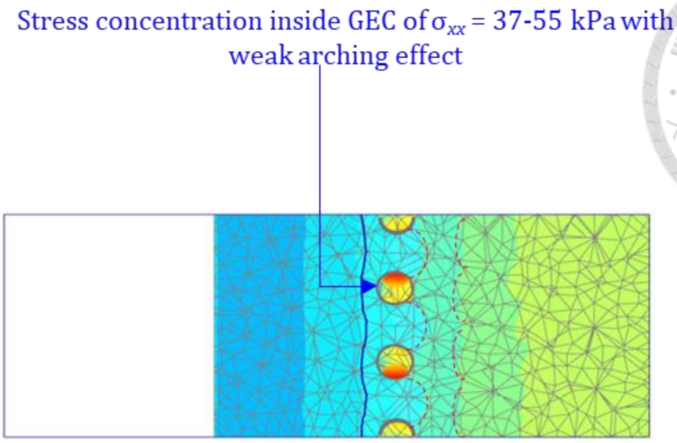

(b)

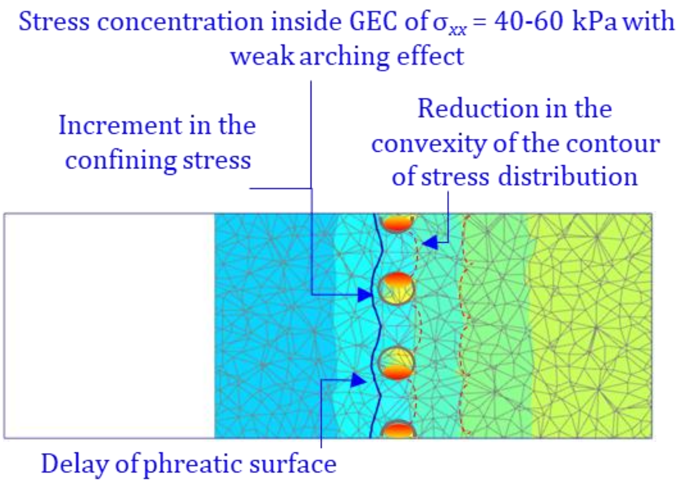

(c)

Figure 6.9: Influence of stiffness of encased granular soil (E_{50}^{ref}) on contour of horizontal stress (σ_{xx}) at slope height of 3.0-m for: (a) E_{50}^{ref} = 45000 kPa; (b) E_{50}^{ref} = 75000 kPa; and (c) E_{50}^{ref} = 100000 kPa

doi:10.6342/NTU202301082

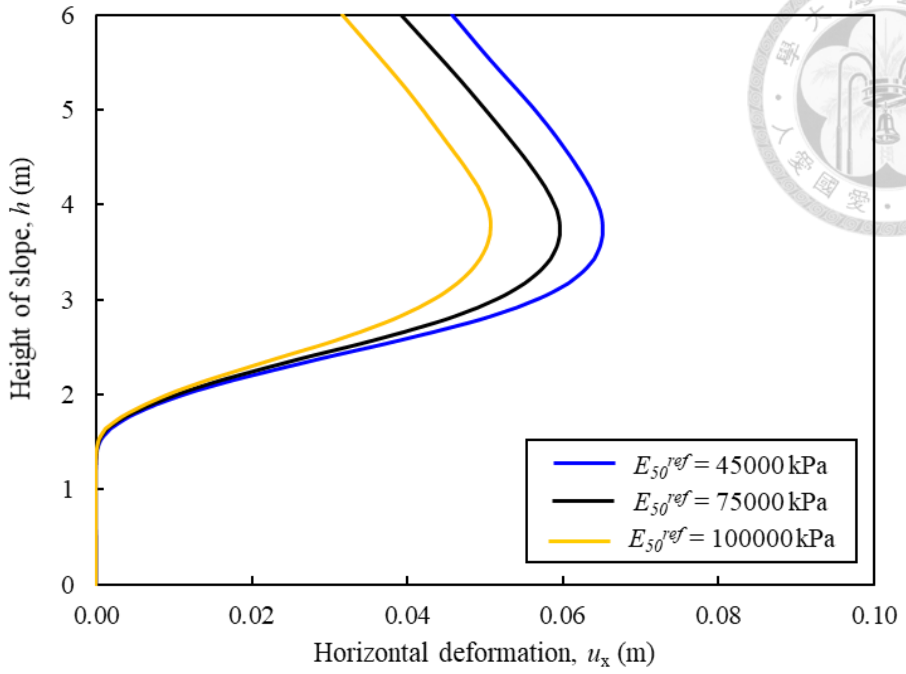

Figure 6.10: Influence of stiffness of encased granular soil (E_{50}^{ref}) on horizontal deformation of GEC

6.3 Shear strength parameter of encased soil

Figure 6.11 illustrates the impact of the shear strength parameter of the encased granular soil on the progression of settlement at the crest ($|u_z|$), settlement at the top ($|u_z|$), and the dissipation of pore water pressure (*PWP*). This analysis is conducted while keeping all other parameters constant. The shear strength parameters are represented through a set of values, reflecting the cohesion and frictional angle of the encased soil while maintaining the stiffness parameters as a constant. Four different combinations of shear strength properties are considered: the first set consisted of c' = 1 kPa and ϕ' = 34.7°, the second set of c' = 2 kPa and ϕ' = 38°, the third of c' = 4 kPa and ϕ' = 40°, and the fourth set of c' = 5 kPa and ϕ' = 42°. The results indicate that horizontal deformation, settlement, and failure time tended to increase with an escalation in the shear strength parameters. However, variations in the dissipation of pore water pressure remained

doi:10.6342/NTU202301082

insignificant.

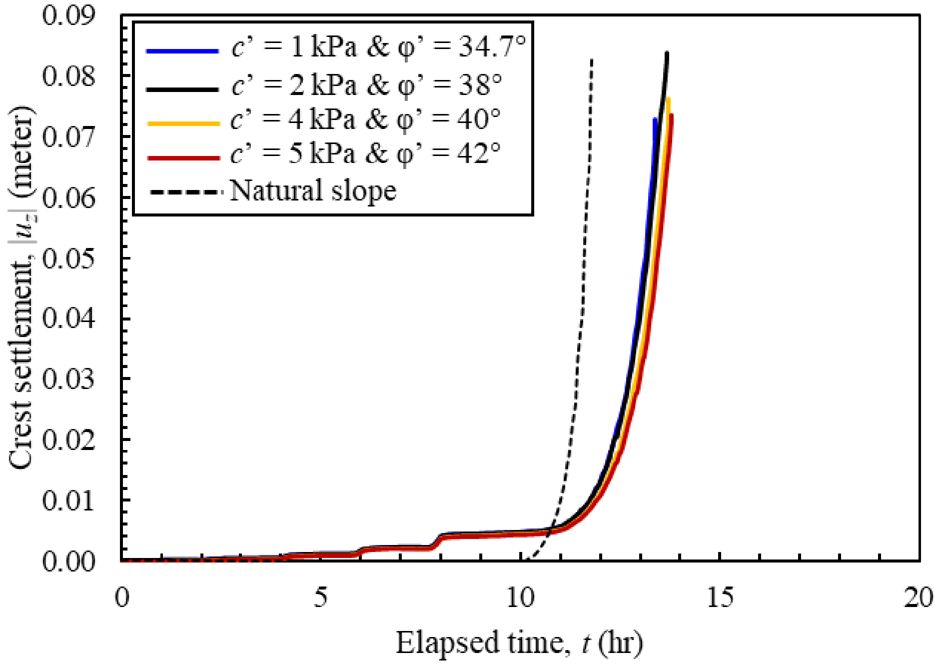

(a)

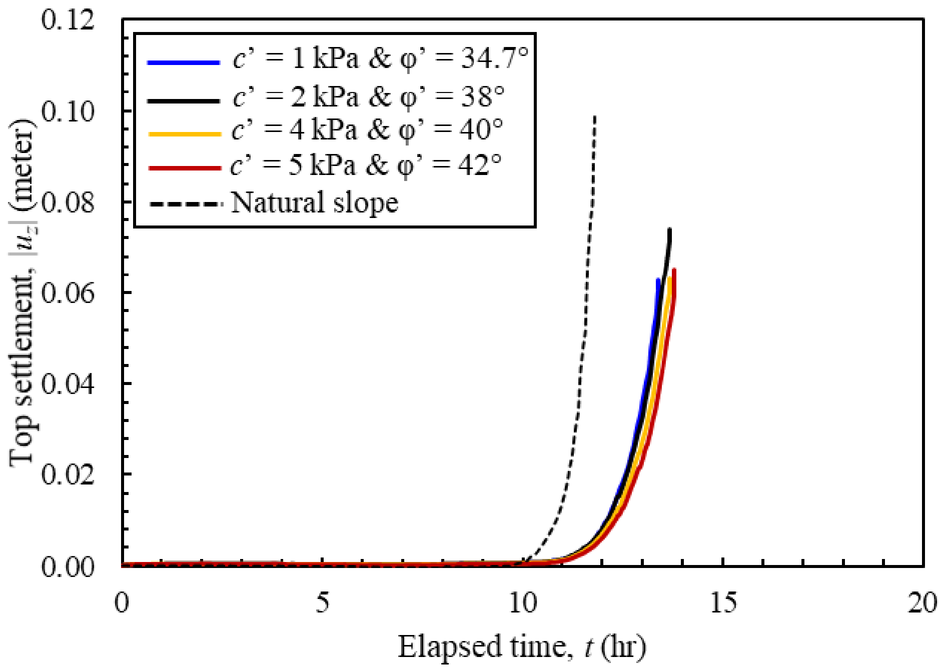

(b)

doi:10.6342/NTU202301082

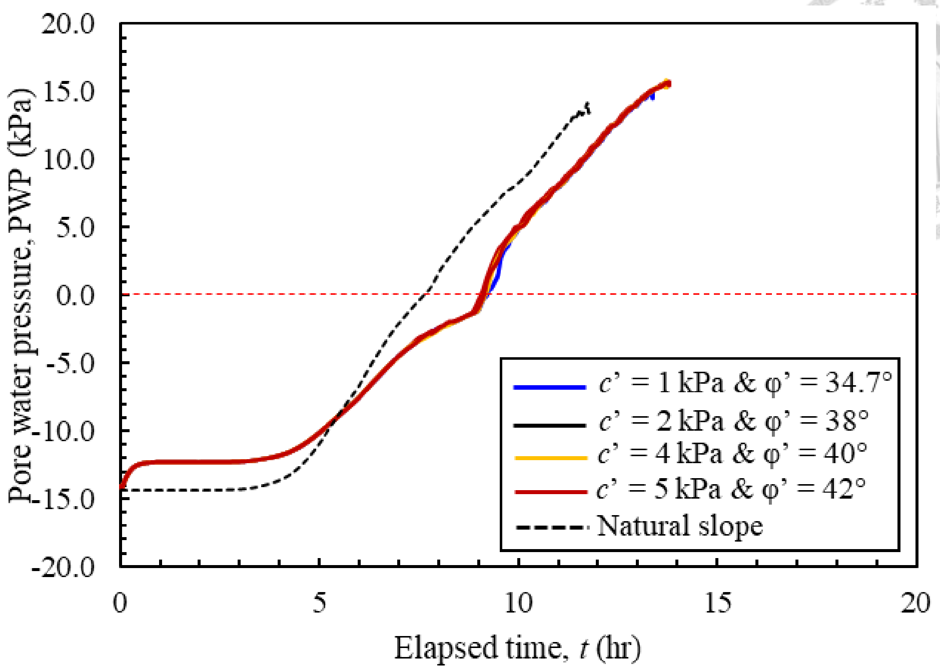

(c)

Figure 6.11: Influence of shear strength parameter of encased granular soil (c' and φ') on: (a) progression of settlement of crest ($|u_z|$); (b) progression of settlement of top ($|u_z|$); and (c) dissipation of pore water pressure (*PWP*)

Figure 6.12 elucidates the progression of the failure surface in relation to an increase in the shear strength parameters. As the shear strength of the encased soil augmented, it was observed that the failure surface initiating from the toe was unable to penetrate the GEC structure. This occurred despite the stabilized slope side possessing adequate weakness to precipitate failure. This particular circumstance led to the isolation of the failure surface, resulting in the formation of two distinct failure surfaces. The first was identified as the active failure wedge, situated on the stabilized slope side. The second was classified as the passive failure wedge, located on the existing slope side. A further increment in the shear strength parameters significantly emphasized the delineation between these failure wedges.

doi:10.6342/NTU202301082

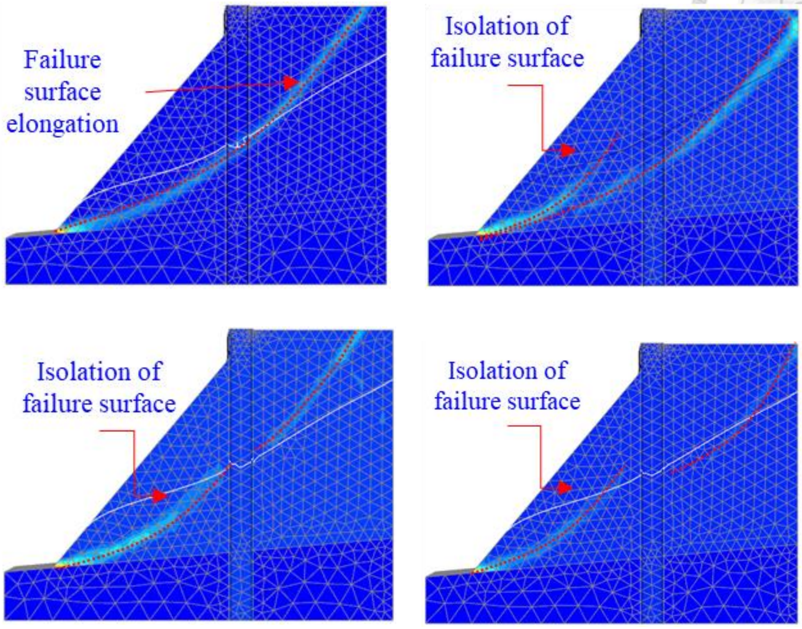

Figure 6.12: Influence of shear strength parameter of encased granular soil (c' and φ') on incremental deviatoric strain ($\Delta\gamma_s$) for: (a) c' = 1 kPa and φ' = 34.7°; (b) c' = 2 kPa and φ' = 38°; (c) c' = 4 kPa and φ' = 40°; and (d) c' = 5 kPa and φ' = 42°

Figure 6.13 illustrates that an increase in the shear strength parameters induced a decline in confining stress, conforming to the observed failure wedge phenomenon. This subsequently led to a decrease in the convexity of the contour of stress distribution. Further to this, the lag in the emergence of the phreatic surface indicated that slope failure was postponed until prior to the point of failure. Table 6.2 highlights a significant influence exerted by the rise in shear strength parameters on the reduction of hoop strain. Consequently, the collective effect of reduced confining stress and hoop strain substantiated the isolation of the failure surface.

doi:10.6342/NTU202301082

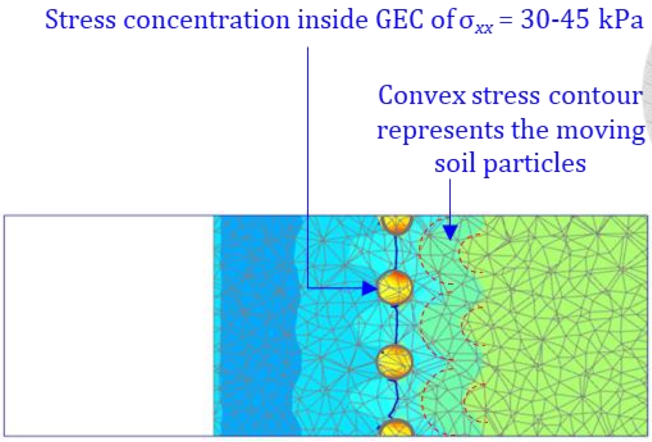

(a)

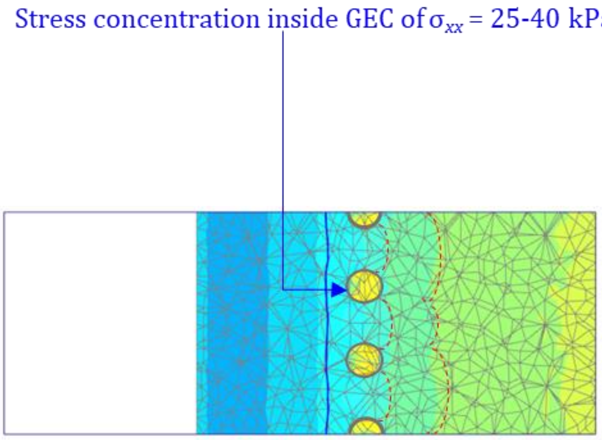

(b)

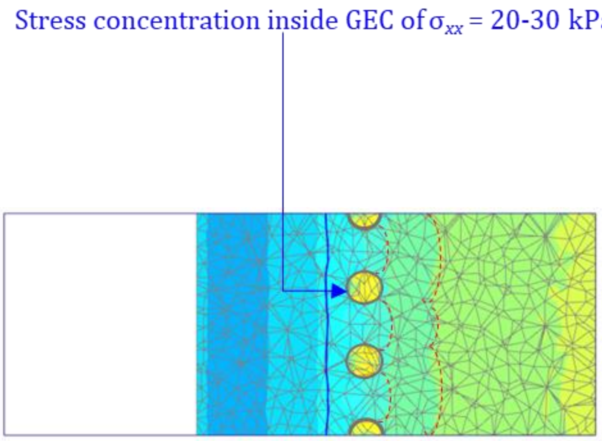

(c)

doi:10.6342/NTU202301082

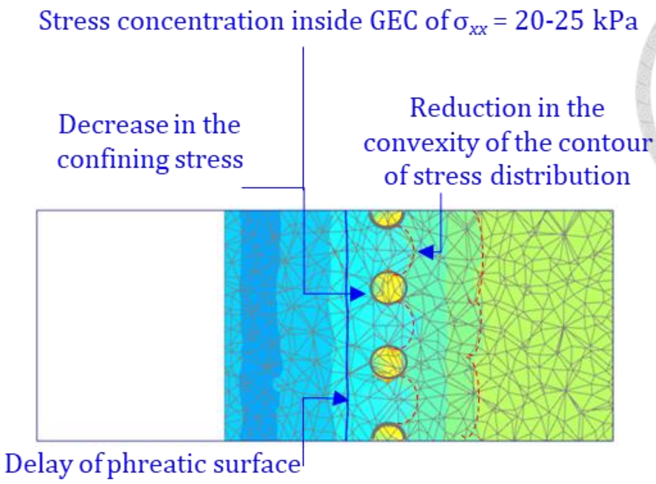

(d)

Figure 6.13: Influence of shear strength parameter of encased granular soil (*c*' and φ') on contour of horizontal stress (σ_{xx}) at slope height of 3.0-m for: (a) c' = 1 kPa and φ' = 34.7°; (b) c' = 2 kPa and φ' = 38°; (c) c' = 4 kPa and φ' = 40°; and (d) c' = 5 kPa and φ' = 42°

Figure 6.14 demonstrates that an increment in shear strength properties led to a reduction in the horizontal deformation of the GEC centerline.

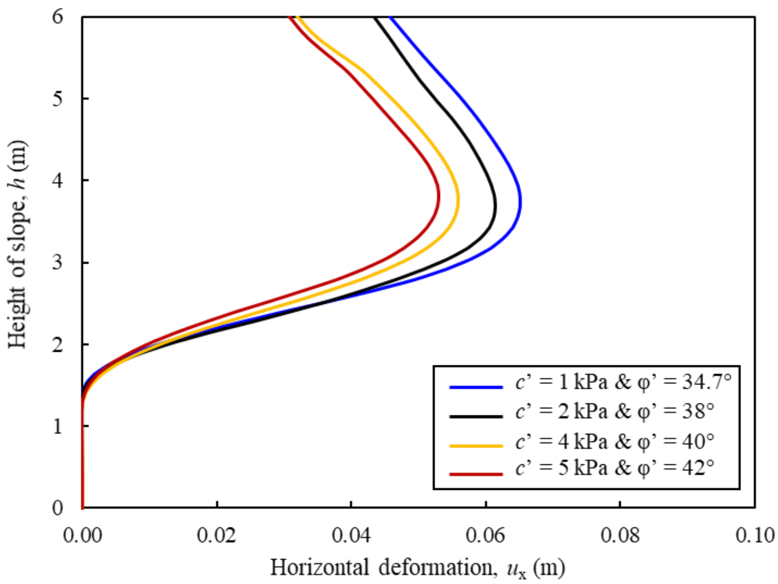

Figure 6.14: Influence of shear strength parameter of encased granular soil (*c*' and φ') on horizontal deformation of GEC

doi:10.6342/NTU202301082

6.4 Relative permeability of sloped soil ($k_{sat\text{-}encased}/k_{sat\text{-}sloped}$)

The concept of relative permeability is introduced in this study as a means to elucidate the conditions under which encased soil can effectively dissipate pore water pressure in comparison to sloped soil. It is defined as the ratio of the saturated hydraulic conductivity of encased soil to that of sloped soil.

Relative permeability of sloped soil, $k_e / k_s = \dfrac{k_{sat-encased}}{k_{sat-sloped}}$ (5.3)

Where, $k_{sat\text{-}encased}$ and $k_{sat\text{-}sloped}$ are the saturated permeability of encased soil and sloped soil respectively.

Figure 6.15 delineates the impact of relative permeability on the progression of horizontal displacement, settlement, and pore water pressure, while holding all other parameters constant. The factor of relative permeability is observed to vary between k_e/k_s = 10^0, 10^1, 10^2, and 10^3, with k_e/k_s = 14 for the standard case. Additionally, Figure 5.16 displays the resulting alterations in the failure surface pattern. Interestingly, complete saturation does not occur with lower relative permeability values, hence hindering the optimal utilization of the drainage property. It's noteworthy that, specifically for the case of saturated encased soil, no discernible change in the failure surface pattern is detected. The failure surface generally develops towards the top of the slope, indicative of failure surface elongation. It is critical to understand that relative permeability pertains to the hydraulic properties of the slope system, rather than its mechanical properties. As such, no significant changes in the failure surface are to be expected based on variations in relative permeability alone.

doi:10.6342/NTU202301082

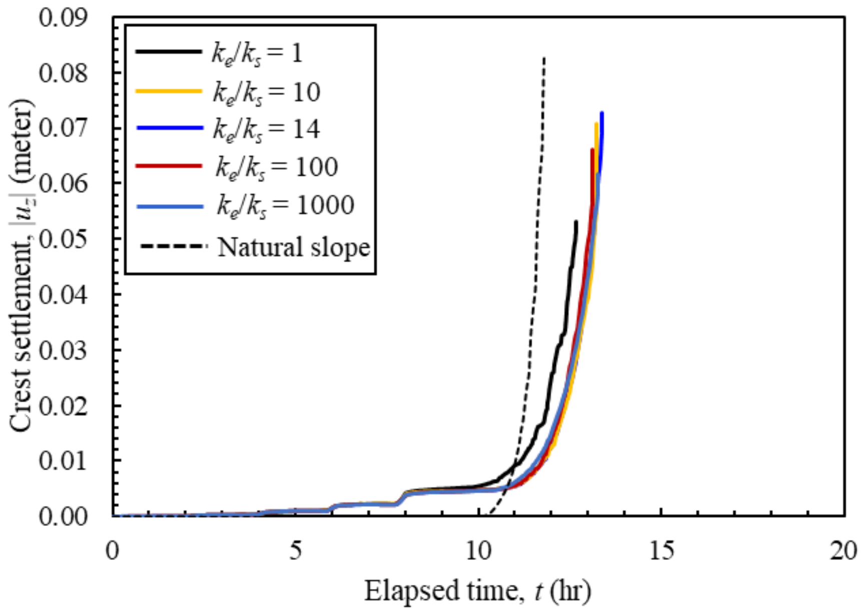

(a)

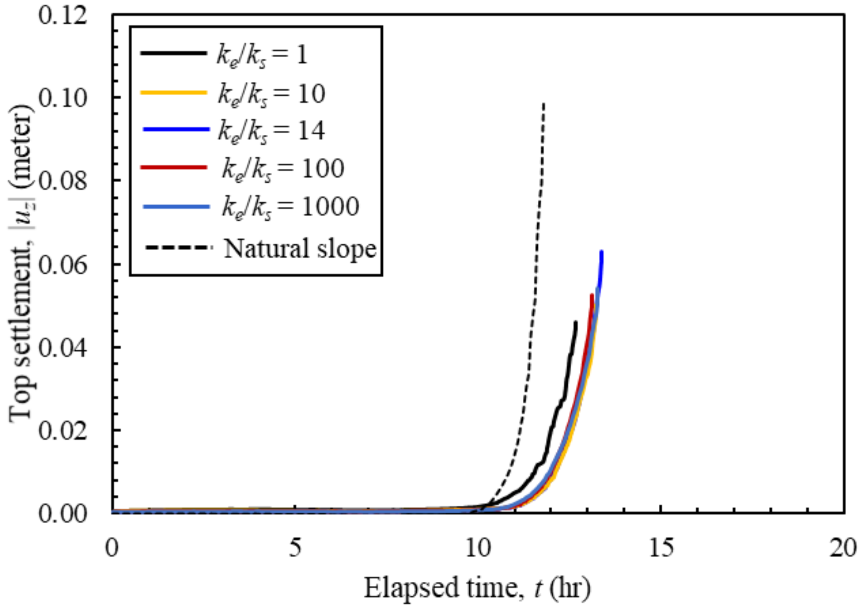

(b)

doi:10.6342/NTU202301082

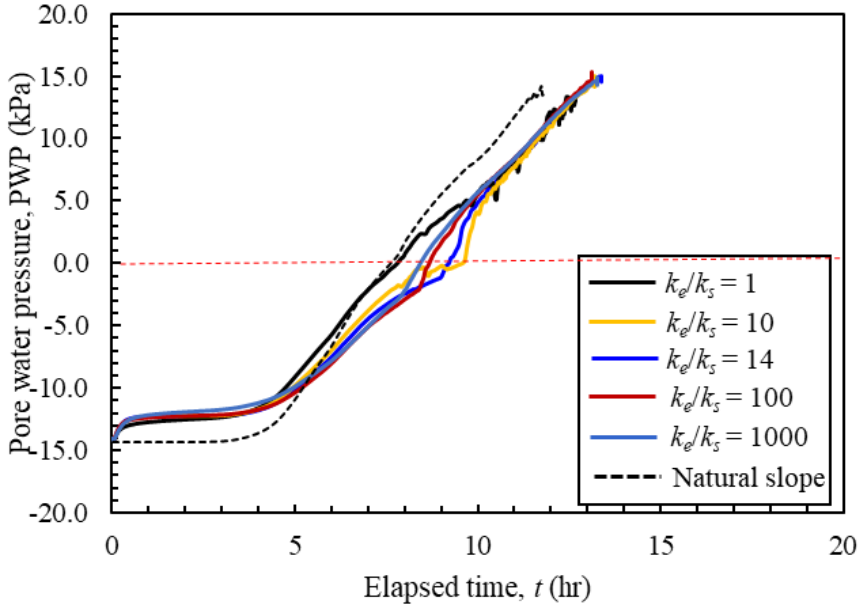

(c)

Figure 6.15: Influence of relative permeability of sloped soil ($k_{sat\text{-}encased}/k_{sat\text{-}sloped}$) on: (a) progression of settlement of crest ($|u_z|$); (b) progression of settlement of top ($|u_z|$); and (c) dissipation of pore water pressure (PWP)

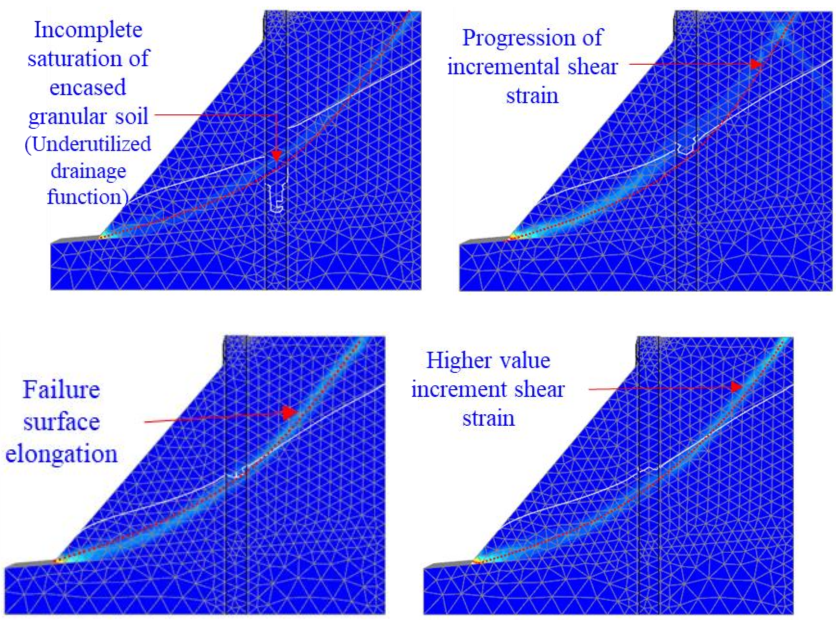

doi:10.6342/NTU202301082

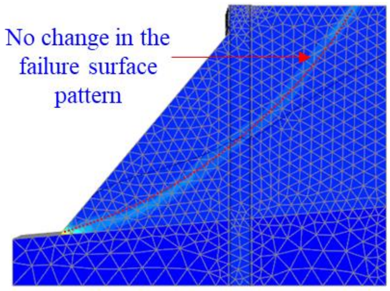

Figure 6.16: Influence of relative permeability of sloped soil ($k_{sat\text{-}encased}/k_{sat\text{-}sloped}$) on incremental deviatoric strain ($\Delta\gamma_s$) for: (a) $k_e/k_s = 10^0$; (b) $k_e/k_s = 10^1$; (c) $k_e/k_s = 14$; (d) $k_e/k_s = 10^2$; and (e) $k_e/k_s = 10^3$

Figures 6.17 and 6.18 illustrate that the influence of relative permeability on the stability of a Geosynthetic Encased Column (GEC) stabilized slope system can be categorized into three distinct mechanisms: (1) the stage of undersaturation, (2) the transition from under- to over-saturation, and (3) the stage of oversaturation. These stages can be inferred from the shape of the phreatic surface. In circumstances where relative permeability is exceedingly low, sloped soil tends to achieve saturation before encased soil does. In such cases, seepage predominantly occurs through the sloped soil, resulting in the outward bulging of the phreatic surface towards the toe of the slope. Conversely, when relative permeability is exceptionally high, the encased soil reaches saturation before the sloped soil. Under these conditions, seepage through the sloped soil is exacerbated by the highly permeable encased soil, causing the phreatic surface to bulge inwards towards the toe of the slope. Between these two stages of under- and oversaturation, there exists a transition stage. This stage is characterized by an optimal level of relative permeability that facilitates sufficient seepage and thereby stabilizes the slope system. During this phase, the phreatic surface is more likely to be linear, indicating a simultaneous saturation of the slope system in both the encased and sloped soil.

doi:10.6342/NTU202301082

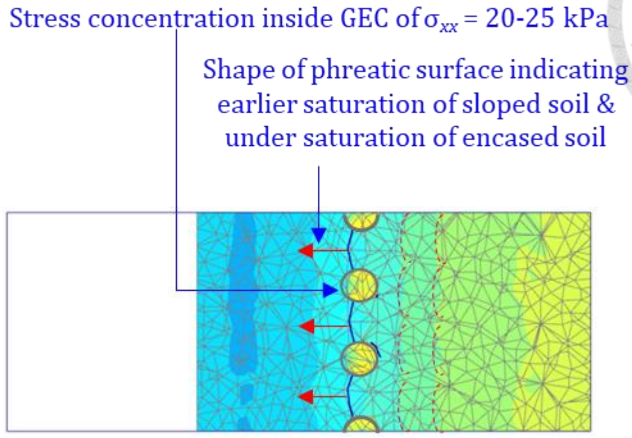

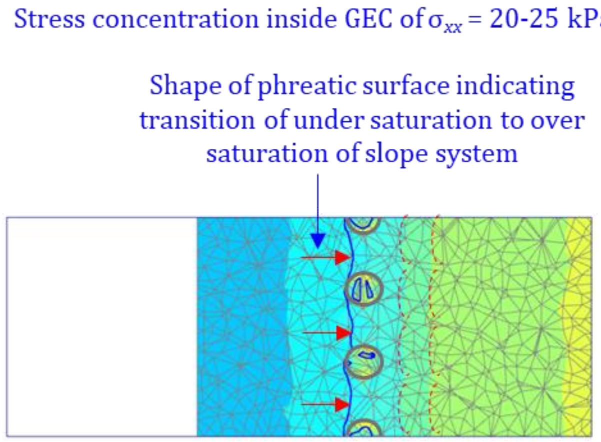

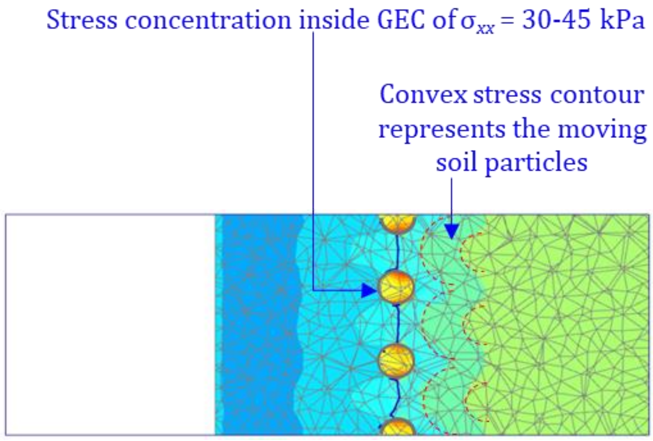

doi:10.6342/NTU202301082

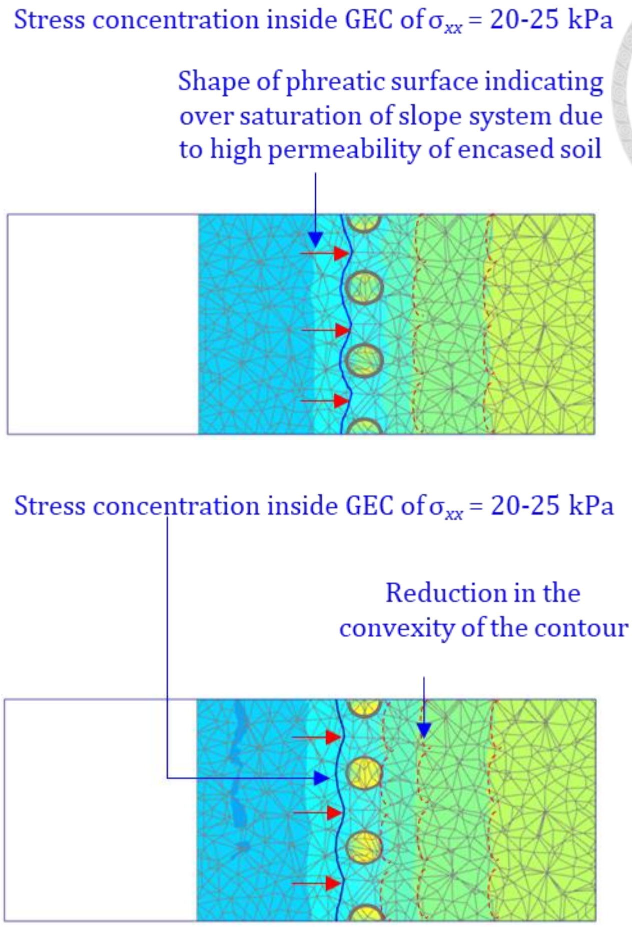

Figure 6.17: Influence of relative permeability of sloped soil ($k_{sat\text{-}encased}/k_{sat\text{-}sloped}$) on contour of horizontal stress (σ_{xx}) at slope height of 3.0-m for: (a) $k_e/k_s = 10^0$; (b) $k_e/k_s = 10^1$; (c) $k_e/k_s = 14$; (d) $k_e/k_s = 10^2$; and (e) $k_e/k_s = 10^3$

doi:10.6342/NTU202301082

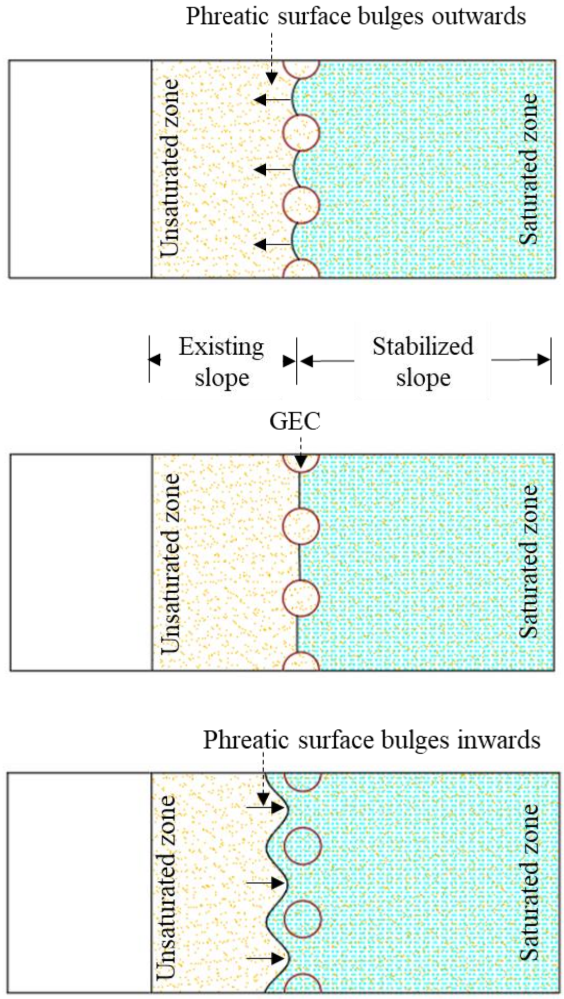

Figure 6.18: Mechanism of influence of relative permeability of sloped soil ($k_{sat-encased}/k_{sat-sloped}$) on slope stability: (a) stage of undersaturation; (b) transition stage; and (c) stage of oversaturation

Figure 6.19 illustrates that satisfactory drainage properties can be leveraged when the relative permeability is at an optimal level to dissipate pore water pressure effectively. As previously discussed, lower horizontal deflection is observed when the drainage properties of the Geosynthetic Encased Column (GEC) are adequate to facilitate water seepage through the GEC, while concurrently preventing excessive water flow that could potentially lead to slope failure. However, it is important to note that this study does not

doi:10.6342/NTU202301082

include an analytical estimation of the influence of the GEC's relative permeability on slope stability when subject to seepage. This aspect remains a potential avenue for further research.

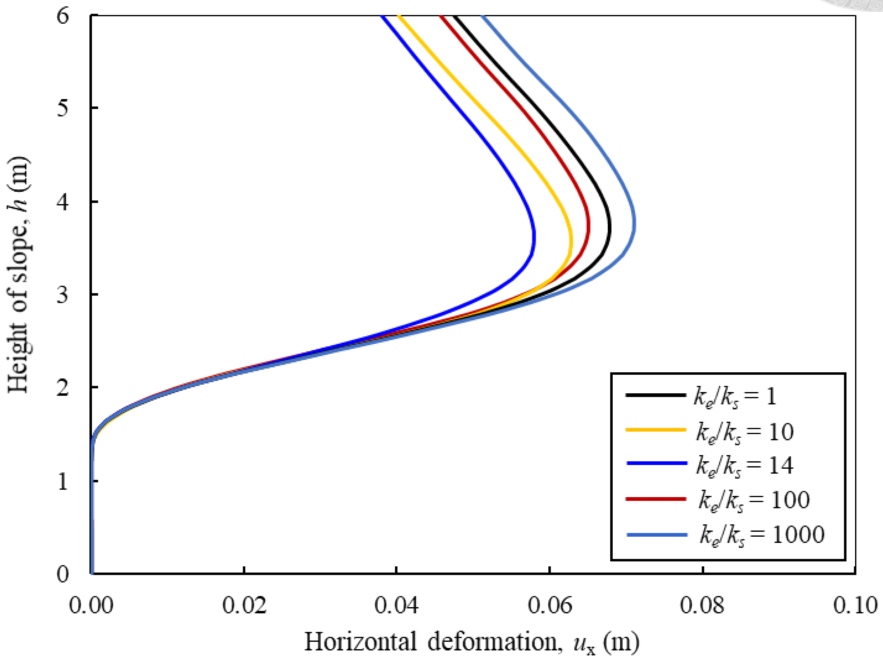

Figure 6.19: Influence of relative permeability of sloped soil ($k_{sat\text{-}encased}/k_{sat\text{-}sloped}$) on horizontal deformation of GEC

6.5 Spacing to diameter (S/D) ratio

Figure 6.20 demonstrates the impact of the *S/D* ratio on the progression of horizontal displacement, settlement, and pore water pressure, while maintaining all other parameters constant. The *S/D* ratio varies between *S/D* = 1.0, 2.0, and 3.0. A lower *S/D* ratio implies a higher concentration of Geosynthetic Encased Columns (GECs) installed in the natural slope, which could potentially improve both the mechanical and hydraulic performance, thereby enhancing slope stability. The numerical results show that an increase in the *S/D* ratio correlates with a decrease in horizontal displacement, while it prompts an increase in settlement. An elevated *S/D* ratio hastens the failure of GEC-stabilized slopes under

doi:10.6342/NTU202301082

seepage conditions, and inhibits the effective dissipation of pore water pressure. It is important to note that no noticeable transition in the failure surface is detected, further reinforcing the significance of the *S/D* ratio in slope stabilization studies.

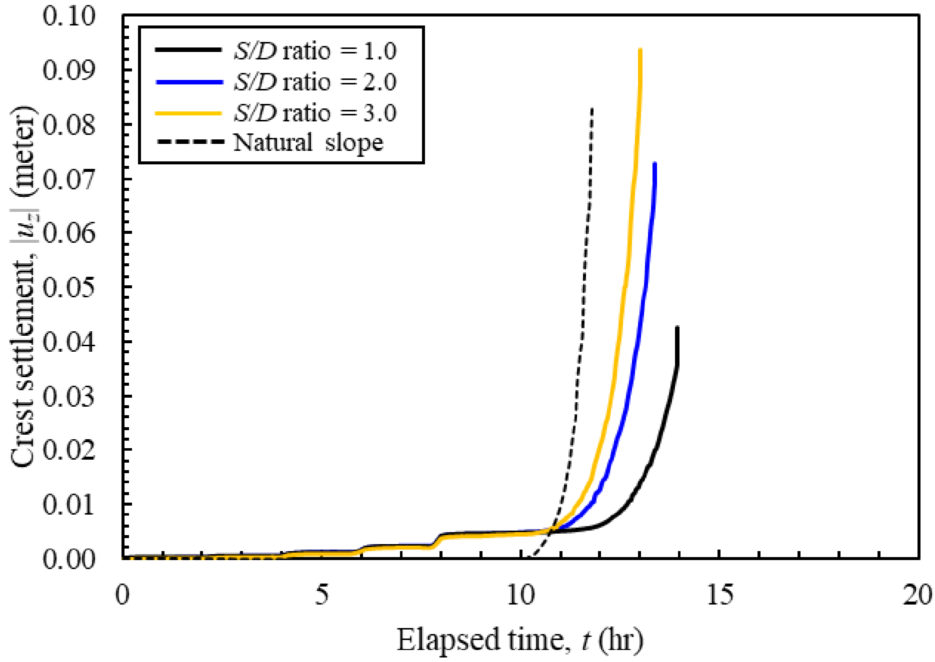

(a)

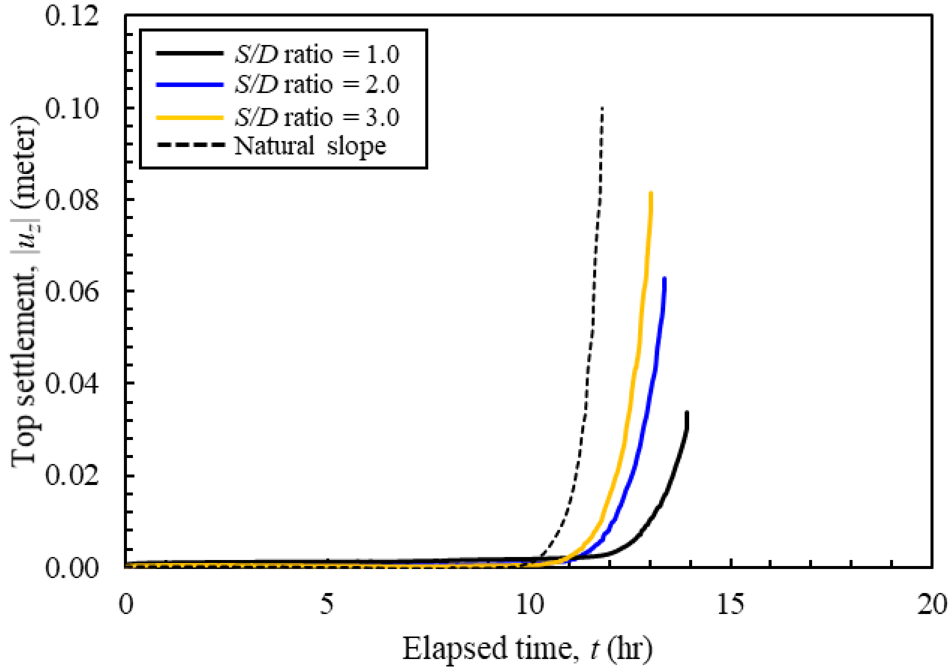

(b)

doi:10.6342/NTU202301082

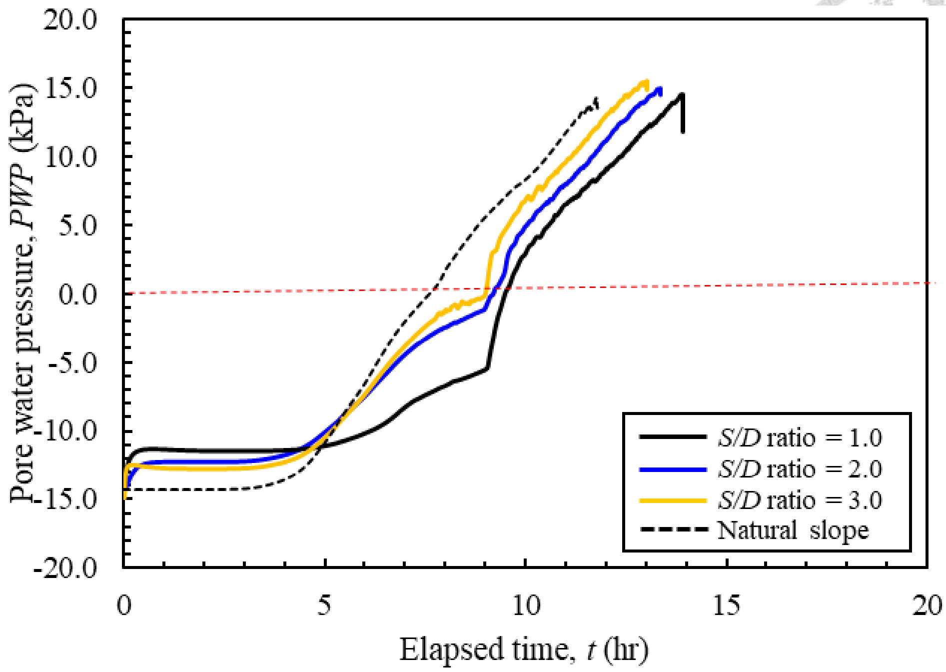

(c)

Figure 6.20: Influence of spacing to diameter (S/D) ratio on: (a) progression of settlement of crest ($|u_z|$); (b) progression of settlement of top ($|u_z|$); and (c) dissipation of pore water pressure (*PWP*)

Figure 6.21 presents the geometry of a Geosynthetic Encased Column (GEC) stabilized slope as it undergoes a parametric study of the *S/D* ratio. The depicted slope cases all experienced failure with elongation of the failure surface. Interestingly, the data show that with a higher *S/D* ratio, the slope failed at lower incremental shear strain values, and conversely, lower *S/D* ratios were associated with higher shear strain values at failure. This relationship further underscores the critical role of the *S/D* ratio in the analysis of slope stability.

doi:10.6342/NTU202301082

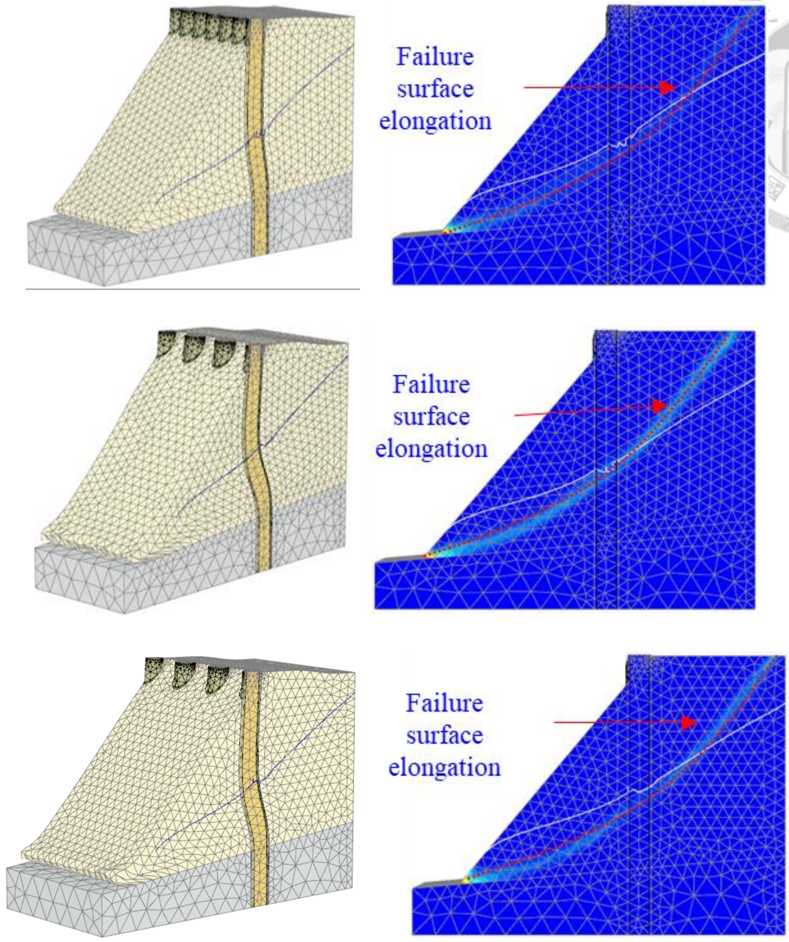

Figure 6.21: Influence of spacing to diameter (S/D) ratio on incremental deviatoric strain ($\Delta\gamma_s$) for: (a) *S/D* = 1.0; (b) *S/D* = 2.0; and (c) *S/D* = 3.0

Figure 6.22 presents the horizontal stress contour at the mid-height of the slope, as determined by numerical analyses. With the increase in the *S/D* ratio, the convexity in the shape of the stress distribution contour diminishes. As such, the resulting stress contour is quite similar to that of a natural slope. This observation underscores the fact that when fewer Geosynthetic Encased Columns (GECs) are installed in a natural slope, the slope is more likely to behave as a natural slope, thereby exhibiting a stress contour similar to that of a natural slope. These findings demonstrate the profound influence of the *S/D* ratio on the stress contour and the behavior of GEC-stabilized slopes.

doi:10.6342/NTU202301082

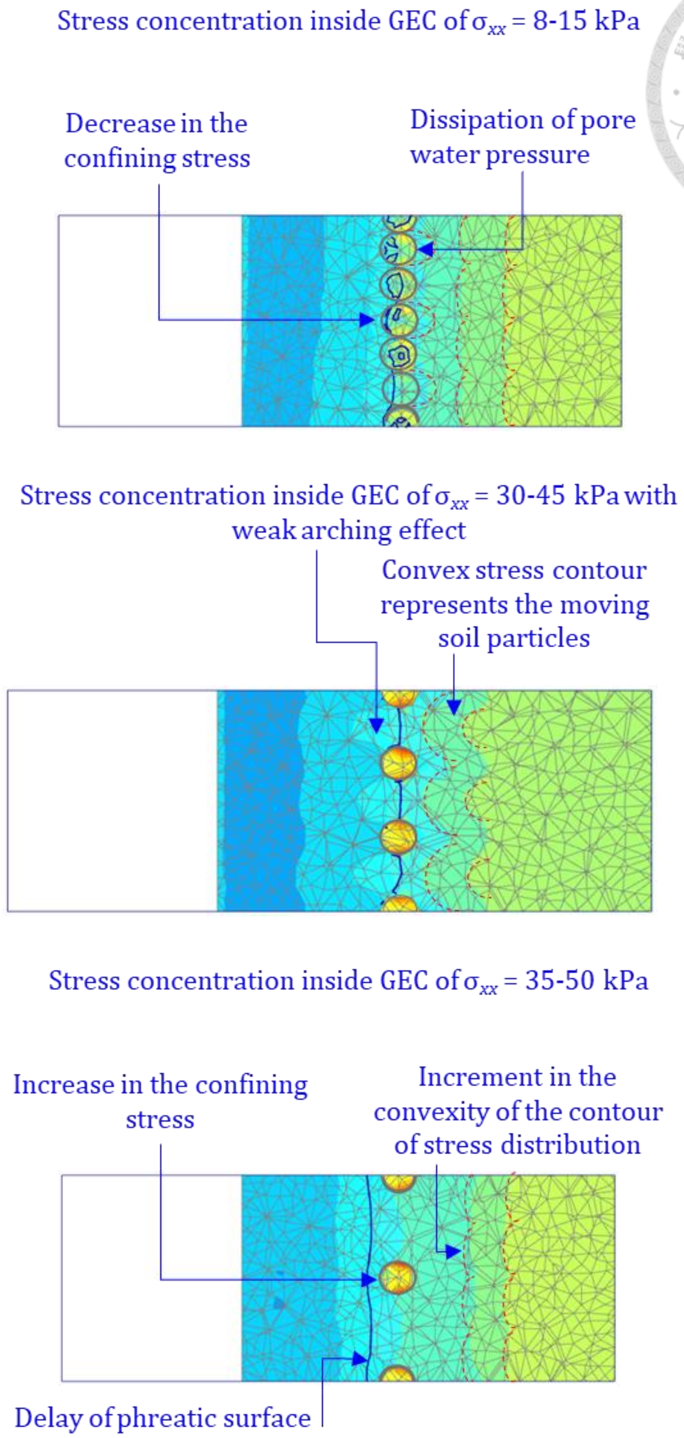

Figure 6.22: Influence of spacing to diameter (S/D) ratio on contour of horizontal stress (σ_{xx}) at slope height of 3.0-m for: (a) *S/D* = 1.0; (b) *S/D* = 2.0; and (c) *S/D* = 3.0

An increase in the hoop strain is observed with the rise in the *S/D* ratio. A higher *S/D* ratio indicates that a greater volume of mobilized soil is being supported by fewer

doi:10.6342/NTU202301082

Geosynthetic Encased Columns (GECs). Consequently, the hoop strain escalates in an effort to prevent slope failure. This observation is further substantiated by the horizontal deflection evident in the GEC, as depicted in Figure 6.23. These findings underline the critical role of the *S/D* ratio in the structural behavior of GEC-stabilized slopes, as it impacts the distribution of stress and strain within the system.

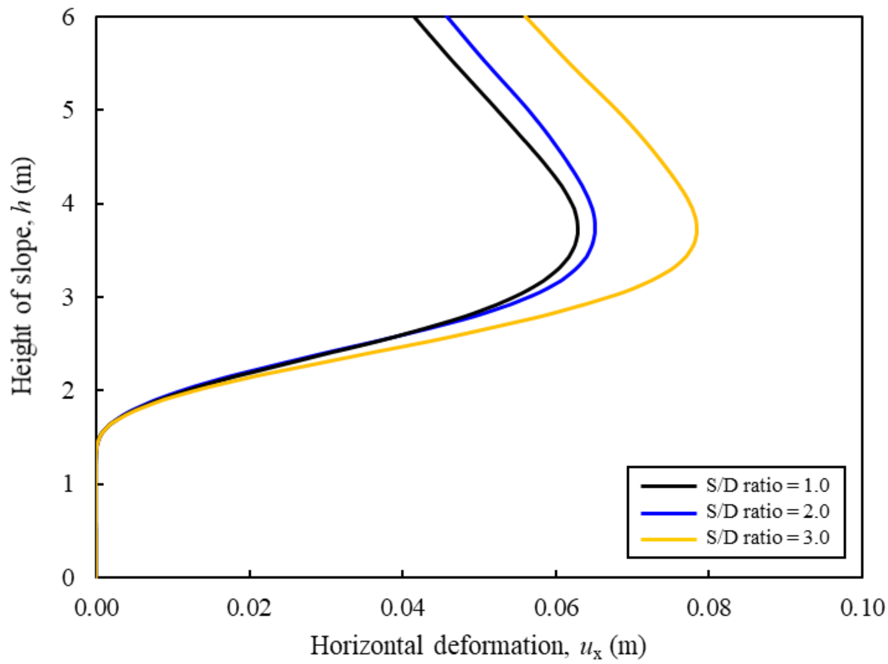

Figure 6.23: Influence of spacing to diameter (S/D) ratio on horizontal deformation of GEC

6.6 Diameter of GEC

In practical applications, the diameter of a Geosynthetic Encased Column (GEC) can range between 0.5 meters and 1.0 meter. A larger diameter can enhance both the mechanical and hydraulic performance, contributing to improved slope stability. However, at the same time, a larger diameter could potentially diminish stability by disrupting a larger portion of the natural slope. This study examines the failure behavior in GEC-stabilized slopes for diameters of 0.5 meters, 0.75 meters, and 1.0 meter, with a constant

doi:10.6342/NTU202301082

S/D ratio of 2.0. Figure 6.24 provides a graphical representation of the slope geometry for this parametric study, highlighting the impact of varying GEC diameters on the behavior and stability of the slope.

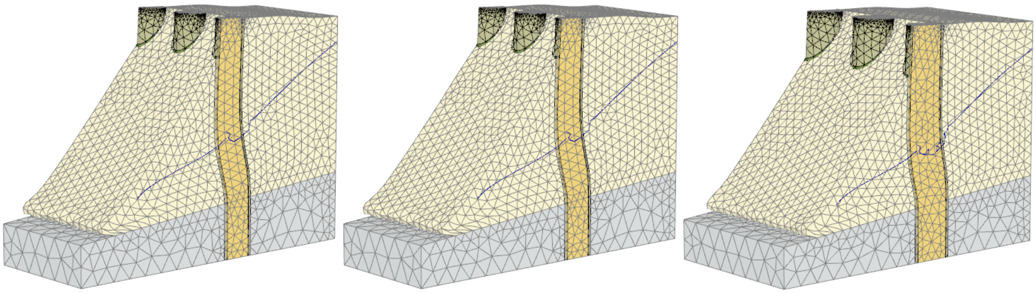

Figure 6.24: Slope geometry for study of the influence of diameter (*D*) of GEC with: (a) *D* = 0.5-m; (b) *D* = 0.75-m; and (c) *D* = 1.0-m

Figure 6.26 delineates the influence of varying diameters on the progression of horizontal displacement, settlement at the top, and the dissipation of pore water pressure in Geosynthetic Encased Column (GEC) stabilized slopes. The enhanced hydraulic and mechanical performance afforded by a larger diameter serves to delay the failure of the GEC stabilized slope under seepage conditions, which implies a quicker dissipation of pore water pressure. Importantly, an increase in diameter is observed to result in an increase in horizontal displacement and a decrease in settlement at the top. This suggests a transition of the failure surface from the elongation stage to the diversion stage. This shift is further corroborated by the corresponding decrease in the convexity of the horizontal stress contour, a reduction in hoop strain, and changes in the deformation of the GEC, all of which confirm the significant role that GEC diameter plays in slope stability.

doi:10.6342/NTU202301082

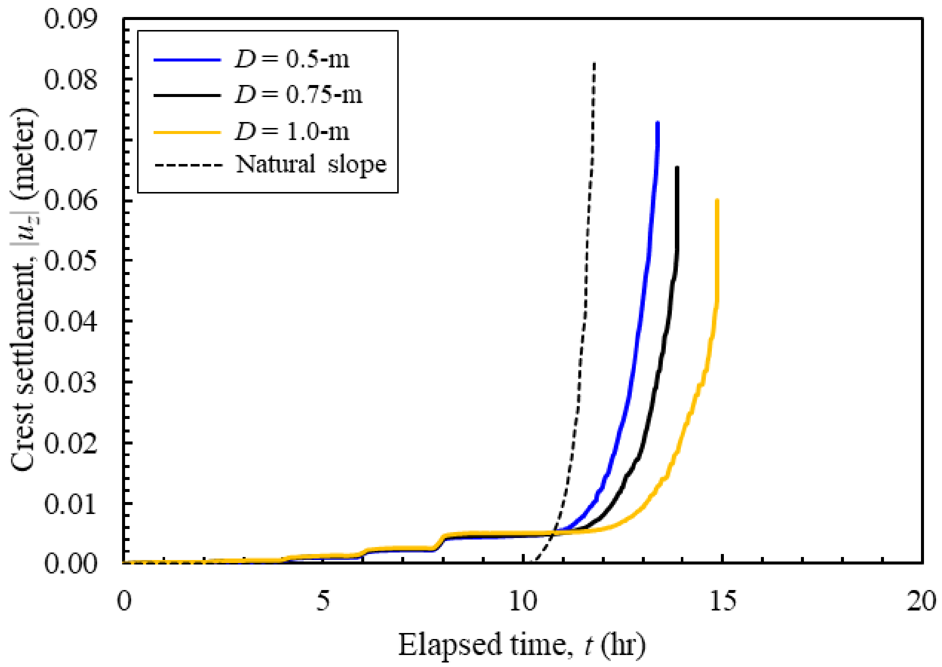

(a)

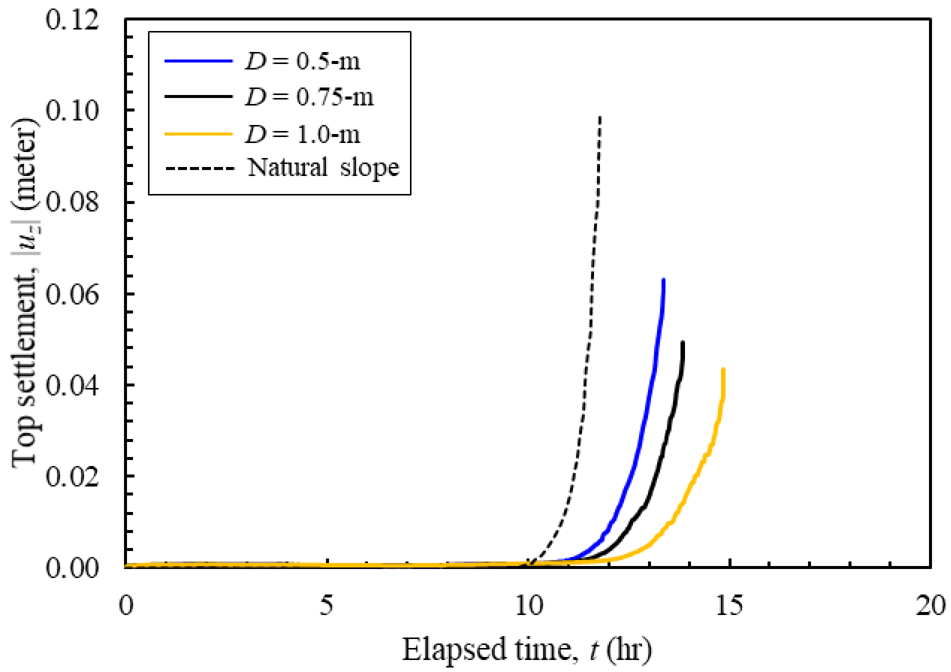

(b)

doi:10.6342/NTU202301082

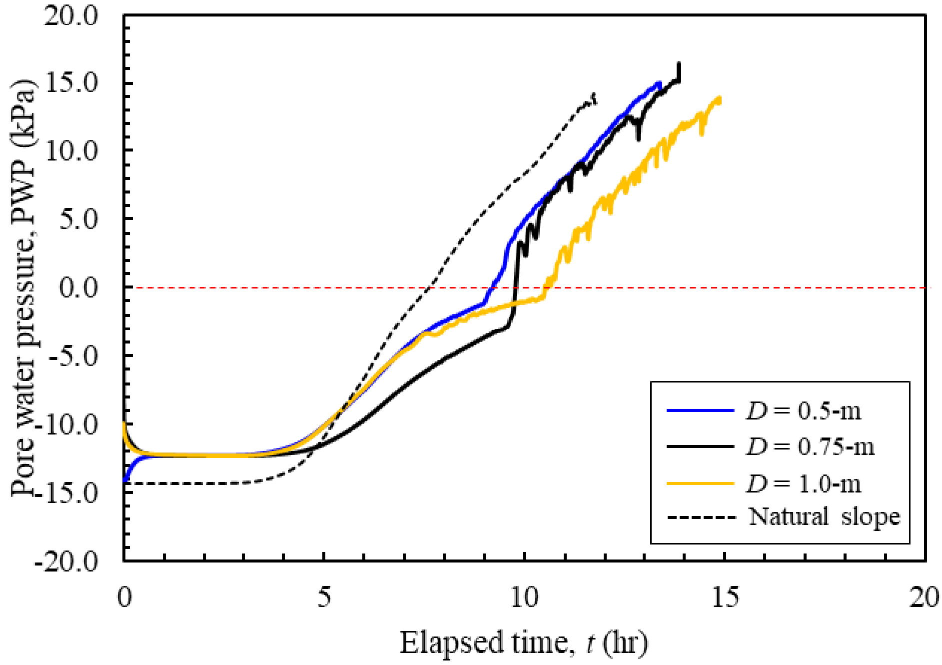

(c)

Figure 6.25 Influence of diameter (D) of GEC on: (a) progression of settlement of crest ($|u_z|$); (b) progression of settlement of top ($|u_z|$); and (c) dissipation of pore water pressure (PWP)

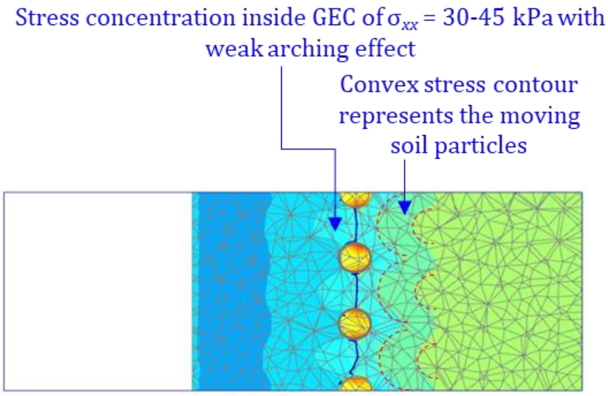

doi:10.6342/NTU202301082

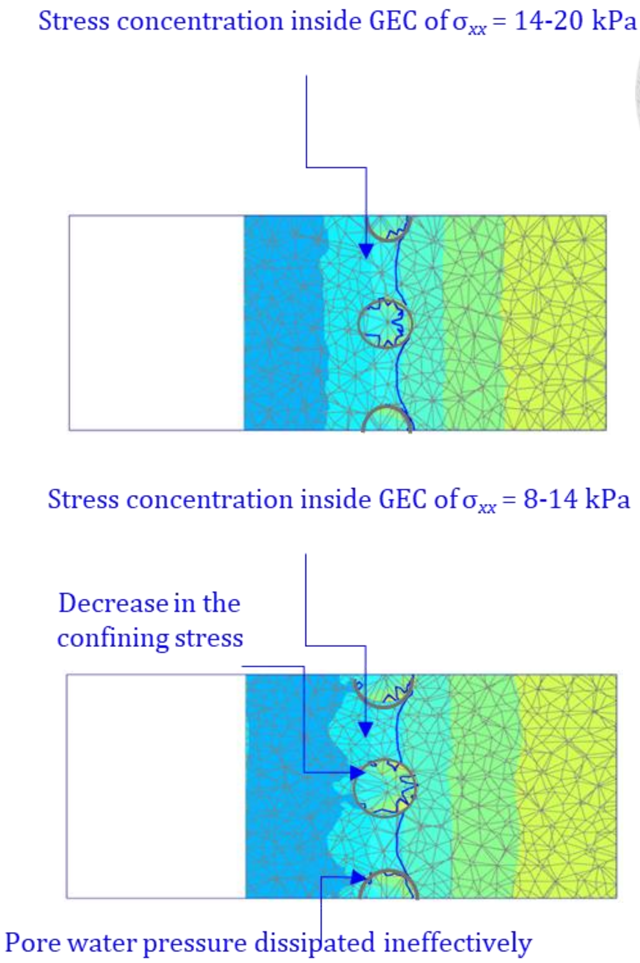

Figure 6.26: Influence of diameter (D) of GEC on contour of horizontal stress (σ_{xx}) at slope height of 3.0-m for: (a) D = 0.5-m; (b) D = 0.75-m; and (c) D = 1.0-m

doi:10.6342/NTU202301082

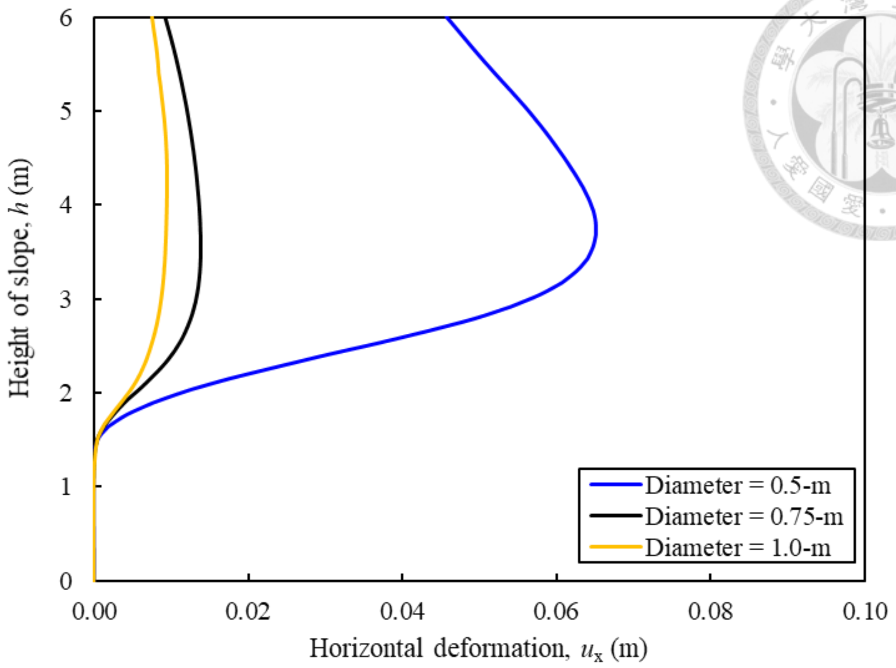

Figure 6.27: Influence of diameter (D) on horizontal deformation of GEC

6.7 Location of GEC

To better comprehend the influence of the Geosynthetic Encased Column (GEC) position on horizontal displacement, top settlement, and the dissipation of pore water pressure, GECs are installed at the top, middle, and bottom of the slope. Given that the maximum column height can be achieved when the GEC is positioned at the top, better mechanical and hydraulic performance is typically realized in such configurations. In these cases, the dissipation of pore water pressure and the mobilization of soil shear strain are optimally utilized. Moreover, a constant, steady-state phreatic surface and a fully developed failure surface can be achieved when the GEC is placed at the top. Consequently, for design practices, it is generally not advisable to position the GEC at the middle or bottom of the slope, given the comparative advantages of a top placement. This insight emphasizes the significant role of the GEC's position in enhancing the stability of slopes.

doi:10.6342/NTU202301082

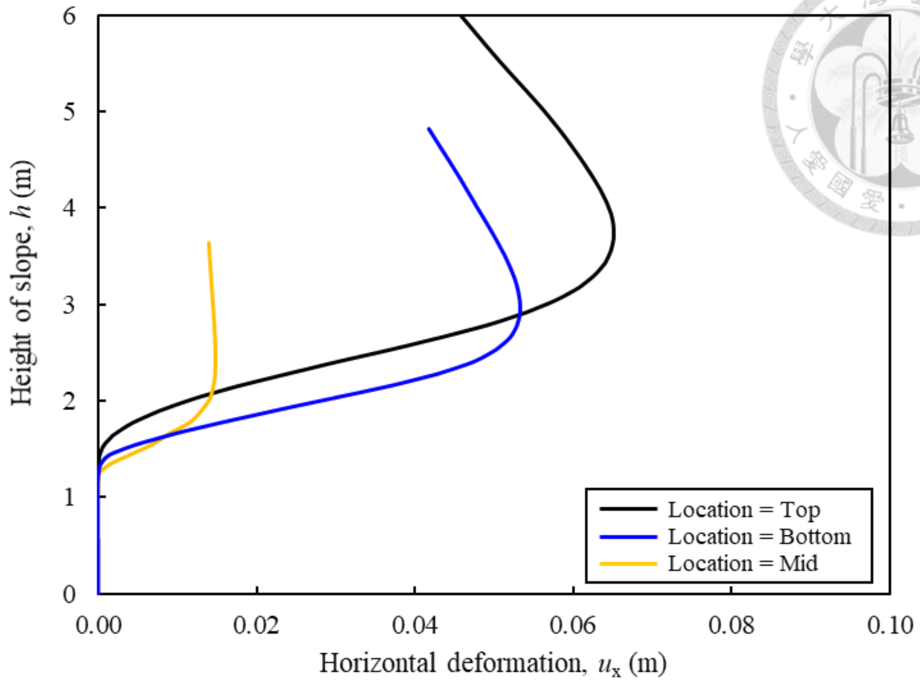

Figure 6.28: Influence of location of GEC on horizontal deformation of GEC

6.8 Sensitivity analysis

Figure 6.29 and 6.30 presents the sensitivity assessment results. The effect of each parameters on $|u_z|$ and t_f values is quantitatively compared using a sensitivity assessment. The x-axis represents the percentage change of input parameters, and the y-axis represents the percentage change in output values. The percentage changes in input or output values are calculated in reference to the baseline case, which is located at the center of the figure. The slope of each line represents the degree of influence of the input parameters on $|u_z|$ and t_f values; the line with a steep slope has a large influence on $|u_z|$ and t_f values.

Figure 6.29 shows the influence of all soil and reinforcement parameters on $|u_z|$. Increment in $J_{50\%}$ assisted to reduce the $|u_z|$ at certain extent, further increment in the input parameters (up to 1300%) caused the failure surface diversion and therefore it got increased (up to 7%). The similar trend is noticed for the relative permeability. Parameters such as stiffness of encased soil, shear strength properties, and diameter

doi:10.6342/NTU202301082

showed the positive correlation. *S/D* ratio is the most influential parameters where reduction in *S/D* ratio by 50% caused the increment in horizontal deformation before failure by 92% which provided sufficiently larger time before failure and failure is steady and slow.

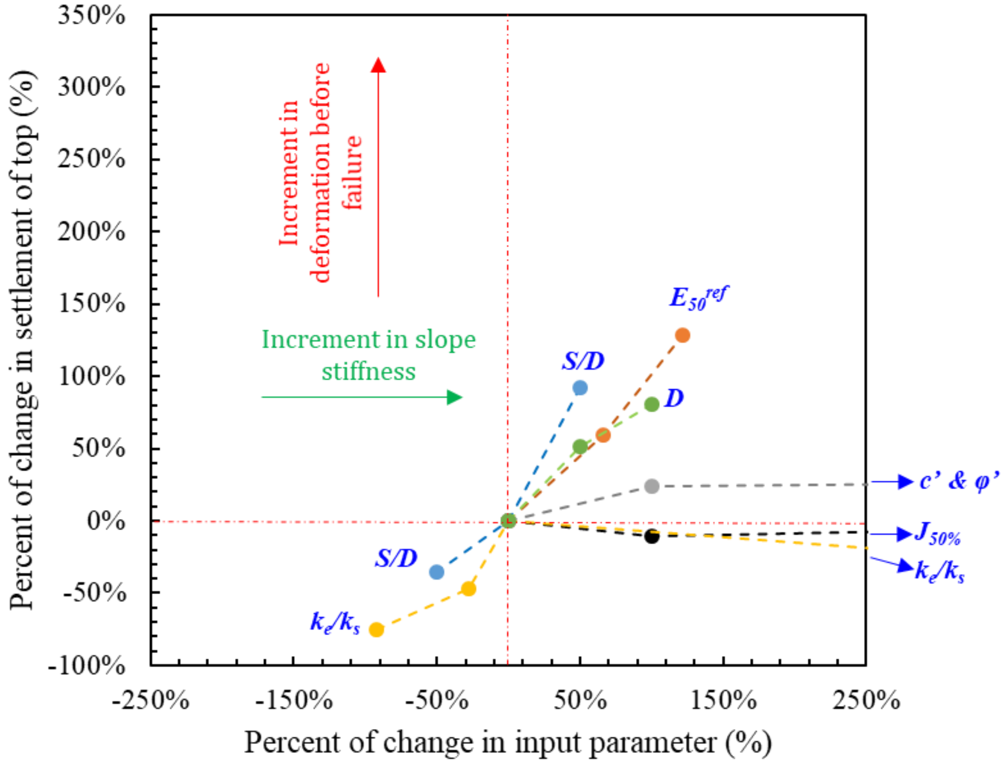

Figure 6.1: Results of sensitivity assessment on settlement of top

doi:10.6342/NTU202301082

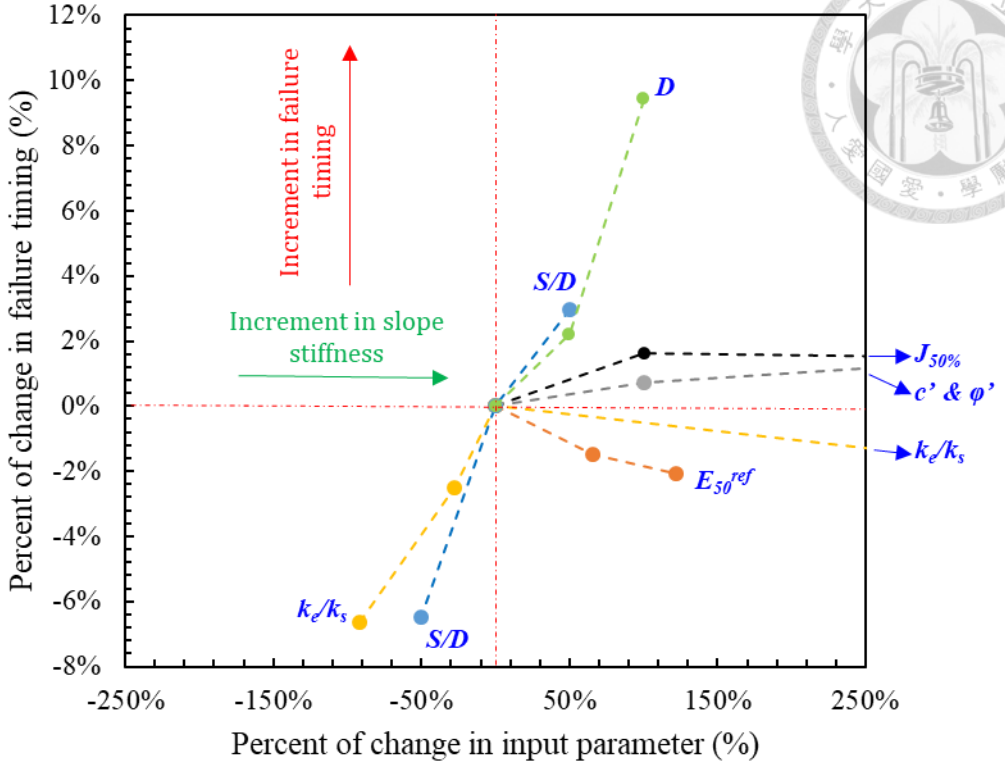

Figure 6.30: Results of sensitivity assessment on failure timing

doi:10.6342/NTU202301082

Chapter 7 Conclusion and Recommendation

7.1 Conclusions

This dissertation presents a series of experimental and numerical studies to evaluate the performance of GEC stabilized slope case as a mitigation measure for excess seepage conditions. The effectiveness of GEC stabilized slope in reducing failure over rigid pile stabilized slope was discussed. The reinforcing mechanisms and the influence of design parameters on the performance of GEC stabilized slope were also investigated. The findings and discussion presented in this research provide valuable information for engineering to optimize the design of GEC stabilized slope for the mitigation of excess seepage conditions. The conclusions of this research are as follows:

1. GEC, being a flexible slope system, allowed for a larger displacement before failure. Performance of GEC stabilized slope improved by combined effect of soil shear strain mobilization of encased soil and vertical drainage property.
2. The rigid pile-stabilized slope, a rigid slope system, failed allowing for a smaller displacement. Rigid pile stabilized slope improved the slope stability by its high bending stiffness.
3. Natural slope failed earlier, while the Geosynthetic Encased Column (GEC) with drainage condition achieved a constant horizontal displacement.
4. Failure mechanism of various slope failure cases could be summarized by three arguments: (1) delay in the development of a fully steady-state seepage condition; (2) failure surface diversion and elongation; and (3) shear strain mobilization.
5. The soil arching effect offers an in-depth understanding of diverse slope stabilization methods and their influence on stress distribution in slopes, particularly under seepage conditions. Rigid piles typically display a concave

doi:10.6342/NTU202301082

shape stress contours, denoting areas of static soil particles subject to high mobilized stress. Conversely, Geosynthetic Encased Columns (GECs) exhibit a convex shape, signifying soil particle mobility on both sides of the slope.

6. Increasing the stiffness of slope system of the GEC stabilized slope system alters the behavior of the GEC from a flexible structure to a rigid one, thereby causing changes in the failure surface. Once the failure surface has been diverted, slope failure occurs sooner.
7. Encasement provided by geotextile improved the performance of OSC as it provided additional confining stress by increment in hoop stress. Therefore, increasing the soil shear strain of the encased soil delayed the failure timing.

7.2 Limitation and recommendation of study

While FEM-based simulation has limitations compared to other commercially available software based on FDM, DEM, or MPM, each method has its own constraints. PLAXIS-3D is considered the best tool for simulating geosynthetic applications. However, several limitations were identified during this study:

1) FEM based simulations did not allow larger displacement. This limitation could not explain the post-failure behaviour of GEC stabilized slope cases.
2) This study does not include the study of the behavior of GEC in rows or the effect of group GEC.
3) For the future study, GEC stabilized slope could be studied under various rainfall conditions.

doi:10.6342/NTU202301082

References

Alexiew, D., Raithel, M., Küster, V., Bau-Aktiengesellschaft, J. M., and Detert, O. (2012). 15 years of experience with geotextile encased granular columns as foundation system.

Ali, K., Shahu, J. T., and Sharma, K. G. (2012). Model tests on geosynthetic-reinforced stone columns: a comparative study. *Geosynthetics International*, 19(4), 292-305.

Araujo, G. L. S., Palmeira, E. M., and Cunha, R. P. (2009). Behaviour of geosynthetic-encased granular columns in porous collapsible soil. *Geosynthetics International*, 16(6), 433-451.

ASTM D6836. (2008). Standard test methods for determination of the soil water characteristic curve for desorption using a hanging column, pressure extractor, chilled mirror hygrometer, and/or centrifuge: *ASTM International*, West Conshohocken, PA, USA.

Ausilio, E., Conte, E., and Dente, G. (2001). Stability analysis of slopes reinforced with piles. *Computers and Geotechnics*, 28(8), 591-611.

Berg, R., Christopher, B. R., and Samtani, N. (2009a). Design of mechanically stabilized earth walls and reinforced soil slopes vol I. Report No. FHwA-NHI-10-024, *Federal Highway Administration*.

Berg, R., Christopher, B. R., and Samtani, N. (2009b). Design of mechanically stabilized earth walls and reinforced soil slopes vol II. Report No. FHwA-NHI-10-025, *Federal Highway Administration*.

Bolton, M. D. (1986). The strength and dilatancy of sands. *Geotechnique*, 36(1), 65-78.

Brinkgreve, R. B. J., Kumarswamy, S., Swolfs, W. M., Zampich, L., and Ragi Manoj, N. (2019). PLAXIS 3D Manual, Plaxis bv, *Bentley Systems*, Inc., Netherlands.

Bryson, L. S., and Zapata-Medina, D. G. (2012). Method for Estimating System Stiffness for Excavation Support Walls. *Journal of Geotechnical and Geoenvironmental Engineering*, 138(9), 1104-1115.

Buckingham, E. (1914). On physically similar systems; Illustrations of the use of dimensional equations. *Physical review*, 4(4), 345-376.

doi:10.6342/NTU202301082

Castro, J., and Sagaseta, C. (2013). Influence of elastic strains during plastic deformation of encased stone columns. *Geotextiles and Geomembranes*, 37, 45-53.

Cengiz, C., Kilic, I. E., and Guler, E. (2019). On the shear failure mode of granular column embedded unit cells subjected to static and cyclic shear loads. *Geotextiles and Geomembranes*, 47(2), 193-202.

Chong, S. Y., Kassim, K. A., Lee, M. L., and Lau, S. H. (2018). Geotextile Encapsulation as Protection to Lime Column under Shear Load. *E3S Web Conf.*, 65, 06005.

Clough, W., and O'Rourke, T. (1990). Construction induced movements of in situ wall. *Geotechnical Special Publication*, 439-470.

Dao, T. P. T. (2011). Validation of PLAXIS embedded piles for lateral loading. *Masters of Science Thesis, TU Delft*, Netherland.

Elias, V., Christopher, B. R., and Berg, R. R. (2001). Mechanically stabilized earth walls and reinforced soil slopes design and construction guidelines. Report No. FHwA-NHI-00-043, *Federal Highway Administration*.

FEMA. 2016b. Dam Maintenance: Technical Advisory for Dams in South Carolina. (*Series of advisories prepared by FEMA under DR-4241-SC; these are unpublished, but available from FEMA*).

Franke, E., and Muth, G. M. (1985). Scale effect in 1g-model tests on horizontally loaded piles. *Proceedings of the 11th international conference on soil mechanics and foundation engineering*, San Francisco, 12-16 Aug 1985.

Galli, A., Maiorano, R., Prisco, C., and Aversa, S. (2017). Design of slope-stabilizing piles: From Ultimate Limit State approaches to displacement based methods. *Rivista Italiana di Geotecnica*, 51, 77-93.

Garcia, F. E., and Bray, J. D. (2019a). Discrete element analysis of earthquake fault rupture-soil-foundation interaction. *Journal of Geotechnical and Geoenvironmental Engineering*, ASCE, 145(9), 04019046.

Gniel, J., and Bouazza, A. (2009). Improvement of soft soils using geogrid encased stone columns. *Geotextiles and Geomembranes*, 27(3), 167-175.

Gui, M.-W., and Alebachew, A. A. (2022). Responses of Laterally Loaded Single Piles Subjected to Various Loading Rates in a Poroelastic Soil. *Applied Sciences*, 12(2), 617.

doi:10.6342/NTU202301082

Haeri, S. M., Kavand, A., Rahmani, I., and Torabi, H. (2012). Response of a group of piles to liquefaction-induced lateral spreading by large scale shake table testing. *Soil Dynamics and Earthquake Engineering*, 38, 25-45.

Hajiazizi, M., Mazaheri, A., and Orense, R. P. (2018). Analytical approach to evaluate stability of pile-stabilized slope. *Scientia Iranica*, 25(5), 2525-2536.

Hajiazizi, M., Nemati, E., Nasiri, M., Bavali, M., and Sharifipur, M. (2020). Optimal location of stone column for stabilization of sand slope: An experimental and 3D numerical investigation. *Scientia Iranica*, 27(1), 105-116.

Hassiotis, S., Chameau, J. L., and Gunaratne, M. (1997). Design Method for Stabilization of Slopes with Piles. *Journal of Geotechnical and Geoenvironmental Engineering*, 123(4), 314-323.

Heibaum, M. (2014). Geosynthetics for waterways and flood protection structures – Controlling the interaction of water and soil. *Geotextiles and Geomembranes*, 42(4), 374-393.

Heidari, M., and El Naggar, M. (2017). Analytical method for the design of stabilizing rigid pile in frictional soil. *GeoOttawa 2017*.

Hong, Y.-S., Wu, C.-S., and Yu, Y.-S. (2016). Model tests on geotextile-encased granular columns under 1-g and undrained conditions. *Geotextiles and Geomembranes*, 44(1), 13-27.

Hosseinpour, I., Riccio, M., and Almeida, M. S. S. (2014). Numerical evaluation of a granular column reinforced by geosynthetics using encasement and laminated disks. *Geotextiles and Geomembranes*, 42(4), 363-373.

Huesker (2021). *Ringtrac product brochure*. https://www.huesker.us/fileadmin/media/Brochures/GB/PB_Ringtrac_GB.pdf

Indraratna, B., Basack, S., and Rujikiatkamjorn, C. (2013). Numerical solution of stone column improved soft soil considering arching, clogging, and smear effects. *Journal of Geotechnical and Geoenvironmental Engineering*, 139(3), 377-394.

Ito, T., Matsui, T., and Hong, W. P. (1981). Design Method for Stabilizing Piles Against Landslide—One Row of Piles. *Soils and Foundations*, 21(1), 21-37.

Jeng, C.-J. and Sue, D.-Z. (2016). Characteristics of ground motion and threshold values for colluvium slope displacement induced by heavy rainfall: a case study in northern Taiwan, *Nat. Hazards Earth Syst. Sci.*, 16, 1309–1321.

doi:10.6342/NTU202301082

Kahyaoğlu, M. R., İmançlı, G., Özden, G., and Kayalar, A. Ş. (2017). Numerical simulations of landslide-stabilizing piles: a remediation project in Söke, Turkey. Environmental Earth Sciences, 76(19), 656.

Khan, S. S., and Ali, M. (2022). Short-Term and Long-Term Needs for Sustainable Concrete: An Overview. *Engineering Proceedings*, 22(1), 14.

Lai, S., Tobita, T., and Nakahara, T. (2005). Generalised scaling relations for dynamic centrifuge tests. *Geotechnique*, 55, 355-362.

Langhaar, H.L. (1951). Dimensional analysis and theory of models. *Krieger*.

Lee, C. Y., Hull, T. S., and Poulos, H. G. (1995). Simplified pile-slope stability analysis. *Computers and Geotechnics*, 17(1), 1-16.

Li, A. J., Wang, W. C., and Lin, H. D. (2022). Investigation of slope reinforcement with drilled shafts in colluvium soils. *Geomechanics and Engineering*, 31(1), 71-86.

Liang, R., and Zeng, S. (2002). Numerical Study of Soil Arching Mechanism in Drilled Shafts for Slope Stabilization. *Soils and Foundations*, 42(2), 83-92.

Lin, H.-D., Wang, W.-C., and Li, A.-J. (2020). Investigation of dilatancy angle effects on slope stability using the 3D finite element method strength reduction technique. *Computers and Geotechnics*, 118, 103295.

Manzari, M. T., and Nour, M. A. (2000). Significance of Soil Dilatancy in Slope Stability Analysis. *Journal of Geotechnical and Geoenvironmental Engineering*, 126(1), 75-80.

Meyer, B., and Reese, L. (1979). Analysis of single piles under lateral loading. Report No. FHwA/TX-79/38+244-1, *Federal Highway Administration*.

Mohapatra, S. R., Rajagopal, K., and Sharma, J. (2016). Direct shear tests on geosynthetic-encased granular columns. *Geotextiles and Geomembranes*, 44(3), 396-405.

Mualem, Y. (1976). A new model for predicting the hydraulic conductivity of unsaturated porous media. *Water Resource Research*, 12, No. 3, 593–622.

Murugesan, S., and Rajagopal, K. (2006). Geosynthetic-encased stone columns: Numerical evaluation. *Geotextiles and Geomembranes*, 24(6), 349-358.

Naderi, E., Asakereh, A., and Dehghani, M. (2020). Numerical and Physical Modeling of Soft Soil Slope Stabilized with Stone Columns. *Journal of Rehabilitation in Civil Engineering*, 8(4), 118-136.

doi:10.6342/NTU202301082

Nagula, S. S., Nguyen, D. M., and Grabe, J. (2018). Numerical modelling and validation of geosynthetic encased columns in soft soils with installation effect. *Geotextiles and Geomembranes*, 46(6), 790-800.

Nasiri, M., and Hajiazizi, M. (2019). An experimental and numerical investigation of reinforced slope using geotextile encased stone column. *International Journal of Geotechnical Engineering*, 15, 543 - 552.

NYSDOT *Geotechnical design manual* (2013). Chapter 14: Ground improvement technology. https://www.dot.ny.gov/divisions/engineering/technical-services/geotechnical-engineering-bureau/geotech-eng-repository/GDM_Ch-14_Ground%20Improvement.pdf

Özçelik, C., Aydoğdu, O., and Kılıç, H. (2012). Behavior of Laterally Loaded Piles on Slopes. *10th International congress on advances in civil engineering*.

Poulos, H. G. (1995). Design of reinforcing piles to increase slope stability. *Canadian Geotechnical Journal*, 32(5), 808-818.

Pradel, D., Garner, J., and Kwok, A. O. L. (2010). Design of Drilled Shafts to Enhance Slope Stability. *In Earth Retention Conference 3* (pp. 920-927).

Pulko, B., Majes, B., and Logar, J. (2011). Geosynthetic-encased stone columns: Analytical calculation model. *Geotextiles and Geomembranes*, 29(1), 29-39.

Ramu, M., Raja, P., and Thyla, P. R. (2010). Development of Structural Similitude and Scaling Laws for Elastic Models.

Reddy, K. M., and Ayothiraman, R. (2015). Experimental Studies on Behavior of Single Pile under Combined Uplift and Lateral Loading. *Journal of Geotechnical and Geoenvironmental Engineering*, 141(7), 04015030.

Rowe, R. K., and Poulos H. G. (1979). A method for predicting the effect of piles on slope behaviour. *Research report in School of Civil Engineering*, Sydney, Australia.

Schanz, T., Vermeer, P. A., and Bonnier, P. G. (1999). The hardening soil model-formulation and verification. Beyond 2000 in Computational Geotechnics – 10 Years of PLAXIS, Balkema, Rotterdam.

Song, H., and Cui, W. (2016). A large-scale colluvial landslide caused by multiple factors: mechanism analysis and phased stabilization. *Landslides*, 13(2), 321-335.

Soralump, S., Shrestha, A., Thowiwat, W., Sukjaroen, R., Chaithong, T., Yangsanphu,

doi:10.6342/NTU202301082

S., Koirala, A., and Jotisankasa, A. (2021). Assessment of landslide behaviour in colluvium deposit at Doi Chang, Thailand. *Scientific Reports*, 11(1), 22960.

Van Genuchten, M. T. (1980). A closed form equation for predicting the hydraulic conductivity of unsaturated soils. *Soil Science Society of America Journal*, 44, No. 5, 892–898.

Vekli, M., Aytekin, M., Banu İkizler, S., and Çalik, Ü. (2012). Experimental and numerical investigation of slope stabilization by stone columns. *Natural Hazards*, 64(1), 797-820.

Viswanadham, B. V. S., and König, D. (2004). Studies on scaling and instrumentation of a geogrid. *Geotextiles and Geomembranes*, 22(5), 307-328.

Vogt, S., Hampel, T., and Braeu, G. (2014). Buckling Resistance of Geotextile-encased Columns. *10th International Conference on Geosynthetics*, Berlin, Germany.

Wong, Y. K. (2013). Comparison of Drainage Line Elements in PLAXIS 2D and 3D applied in Consolidating Marine Clay Deposits.

Wu, C.-S., and Hong, Y.-S. (2009). Laboratory tests on geosynthetic-encapsulated sand columns. *Geotextiles and Geomembranes*, 27(2), 107-120.

Wu, C.-S., Hong, Y.-S., and Lin, H.-C. (2009). Axial stress–strain relation of encapsulated granular column. *Computers and Geotechnics*, 36(1), 226-240.

Zhang, G., and Wang, L. (2017). Simplified evaluation on the stability level of pile-reinforced slopes. *Soils and Foundations*, 57(4), 575-586.

doi:10.6342/NTU202301082